DYNAMIC SILICON NANOPHOTONIC DEVICES FOR ON-CHIP OPTICAL INTERCONNECTS

A Dissertation

Presented to the Faculty of the Graduate School

of Cornell University

in Partial Fulfillment of the Requirements for the Degree of

Doctor of Philosophy

by

Hugo Leonardo Rocha de Lira

January 2012

DYNAMIC SILICON NANOPHOTONIC DEVICES FOR ON-CHIP OPTICAL INTERCONNECTS

Hugo Leonardo Rocha de Lira, Ph.D.

Cornell University 2012

Silicon nanophotonics is one of the most promising candidates to keep the steady increase of computational power we have been used to for the last decades. Its most appealing feature is the amount of data it can deliver, an important factor as complex networks on chip are developed: while Microelectronics suffers from attenuation of the signal traveling through metallic wires as bandwidth is increased, in Photonics losses and bandwidth are not related.

Joining our efforts with many of the interesting insights provided by researchers in this very active field of Silicon Nanophotonics, we present a few more dynamic components which are key for the development and maturing of this technology. The first device we study is a hitless switch, which is formed by two coupled microring resonators which transfer function can be changed from a bandpass filter to a allpass filter. The second object of our study is a thermo-optical coupled resonator filter which can be tuned across many nanometers while keeping its transfer function unchanged. Third we present a coupled cavity filter which has its Free Spectral Range doubled by using Mach-Zehnder Interferometer couplers, and we also demonstrate non-blocking tuning of such a filter. The last device we present is an electrically-driven optical-isolator, which provides an optical isolator without using magnetic materials, being therefore CMOS-compatible. All devices are studied theoretically, designed, fabricated and tested, with results corroborating the theory presented.

BIOGRAPHICAL SKETCH

I was born in São Bernardo do Campo, São Paulo State, Brazil. Son of Sebastião and Maria, brother of Bruno and Cynthia, I was raised in a lovely family. As a child I used to pretend that I worked in a miniature imaginary place of my father's workplace, I used to say that I would build my house aside my family's house, and I used to fight, hate and love my brother. Until we suddenly stop fighting, and then I started to admire him and follow some of his footsteps, including one of our favorites 'sports': to harass our little sister together. A few things can unite more two brothers than a common 5-year-younger-very-talkative sister trying to get some attention. And she knew how to be loud, very, very loud. My brother was accepted at a trainee's school (SENAI) to work at Toyota, and one year later I was accepted as well. He was accepted to a technician school (ETE), and one year later I got there as well. He was accepted in a Engineering College, and, at this point I decided to try another college (ITA) and join the Brazilian Air Force. I almost didn't make it into the College, the admittance exam was quite hard for me. Luckily I was accepted in the last few spots that showed up after some people gave up. I moved to the College campus, which was only 2 hours away from home. I could spend almost all weekends with my family and church, which was a really good, maybe perfect, arrangement. Five years passed, I graduated Summa cum Laude, and a place for me was reserved in the best Optics Research lab in Brazilian Air Force. I got to know some wonderful co-workers and bosses, obtained my Master's degree (ITA) and suddenly I was blessed with the opportunity to come to Cornell to pursuit my PhD. Here I am now, saying goodbye to this memorable place, going back home to share what I learned and help other fellow researchers in this very promising field of Silicon Photonics.

This dissertation is dedicated to my mom and my dad, my brother and his wife, my sister and her fiancée, my beloved spouse-to-be and our future children (may them be many!).

ACKNOWLEDGEMENTS

Some of the people I'd like to acknowledge are hors concours: I'll always be thankful to all my family, all the time, no matter what.

To avoid any sort of injustice, I'll mention names kind of chronologically, as events happened in my life or pop up in my mind.

First, all the people in the Brazilian Air Force who joined their efforts so that I could pursuit my PhD in the US. I don't know the names of all of them, so I'll thank just those who I know and are closer to me: Vilson, who convinced Michal that it would be worth accepting me and, together with Josiel, my previous advisor, encouraged me and supported my decision to accept this mission. Thank you both.

First as well, since it is impossible to put her as second even in a chronological list, my advisor, Michal Lipson. Always friendly and supportive, always demanding and believing in me, it is hard to find the right words to thank her enough. Through her I'd like to thank all of Cornell's Professors and staff members.

Then, the group. Such a wonderful place and environment! Special thanks to Carl, always helpful, always supportive, always there when needed, I cannot imagine the group without him.

The time came when I had to face the cleanroom and Po Dong, who was the first one that I had more interaction with, taught me a bit about the lab, the clean room, and silicon photonics. Thanks, Po! I also was responsible for his remarkable phrase "Nobody doubts it¡' after, well, I decide to question some calculations about group index. Of course I was wrong.

My thanks, as well, to Amy Turner, who really taught me a lot about the cleanroom, and with whom it was always a pleasure to talk. She was one of

the few people with whom I could share my faith, political views and related matters without worries. A good friend.

Then I started learning more and more about the cleanroom with Jaime. Hard working guy, very knowledgeble about almost all the processes, and, well a dear friend. One can always count on him. Thank you.

Talking about fabrication, it is impossible to forget the good-old VB6 days with Sasi. That was fun! Always thinking and running, he taught me a lot about the testing of active devices and many silicon-photonic related things. Thanks, Sasi.

Before going to the lab, I have to thank my desk-neighbor throughout all this four years. Yep, Nick was able to survive for all this time at my side. Very smart, he knows how to listen, and has a big heart. Thank you for your time, help, rides, and anything else I might be missing.

Going back to the lab, I remember annoying Long when he was about to graduate and I wanted to share his setup to get some results for CLEO. Long was patient, knowledgeable about everything photonics related, and always willing to help. Thanks, Long!

Talking about being helpful, I could not even consider writing any paper without abusing the good will of Jacob Levy, the zeroth-author of my papers. Reviewing my soup of ideas written down in some language that hardly resembles English wasn't easy, I know. Jake, thank you very much!

Special thanks to Kyle as well! A hockey game would never be as interesting without his help to teach me what was going on. Go Big Red!

Thanks to Art, another very dear friend. His discipline, humor, competitiveness were always inspiring. Sometimes he even managed to get to the office before me, always making sure to leave a "you-are-late!" note.

I also have to thank a real gentlemen, Mohammed Soltani. As polite as one can be, always with meaningful suggestions and well spirited.

My other desk-neighbors also deserve a grateful thank you. Debo, the true physicist, who even having no more space on his desk still managed not to invade mine, I'm sure that that required lots of effort. And Lian, auntieee!!! Very patient, lover of a good soccer game, I'm sure I need to apologize for being too annoying sometimes. Thank you both!

Last, but not least, all my fellow Brazilians. I was really glad once I got to know that Lucas would join the group. A very good friend, extremely competent, smart, and funny. It was a pleasure to share one more group with him. Also a pleasure to get to know Gustavo, one of the most brilliant guys I ever met. Fellow bike rider, unfortunately his knee didn't like it very much. Thank you!

For all of you, my most sincere thank you. You changed my life, and I'll always be grateful for your support during this journey. Thanks be to God.

TABLE OF CONTENTS

LIST OF TABLES

LIST OF FIGURES

CHAPTER 1

INTRODUCTION

1.1 Silicon and nanophotonics

The astonishing growth in computational power in the last decades, following a trend proposed by Gordon E. Moore and soon baptized as Moore's law [1], is a remarkable achievement for the field of electronics. Materials have been chosen and perfected; processes have been developed and mastered; entrepreneurs have envisioned and made possible all sorts of gadgets to help everyday life. We are habituated to technology and to expect and drive always more of it.

Through the years, many different obstacles attempted to finally stop the trend proposed by Moore's law, each of them succumbing thanks to the dedication and eagerness of many diligent researchers. An illustrative example is the recent history of the clock rate in microprocessors: up to late the 90's we were used to see the clock rate of microprocessors increasing every year, in a very predictable trend, until an also predictable saturation happened around 3 GHz [2]. However, parallel processing and multicore approaches came into help and kept the trend of the improvement in computational power alive and well.

Miniaturization of microelectronics transistor is also to reach a fundamental limit, which is clear considering that the gate of the transistors is already just a few atoms thick [3]. It means that at some point it will not be possible to bring microprocessors closer to each other to reduce intrinsic losses of high frequency electrical signals propagating through metallic wires [4]. Increasing the signal

strength to compensate for losses is an alternative, but there is only so much thermal power a block of silicon can dissipate, and such approach can also lead to prohibitive levels of power consumption [5].

A very promising alternative to increase computational power without requiring reduction of real-state comes from Photonics. In the same way that fiber optics made it possible to reach an unprecedented amount of data communication between personal computers spread all around the globe [6], bringing Optics into multicore multiprocessor chips is a promising way to increase the amount of data communication in a Network on Chip, which is closer to become true through nanotecnologically fabricated optical devices [7].

1.2 Dynamic components on silicon nanophotonics

This dissertation deals with dynamic and reconfigurable optical devices. The platform we use for the devices we fabricate and discuss here is silicon on insulator, which is composed of a crystalline silicon wafer with a 3-µm thick silicon dioxide and with 250 nm of cristalline silicon on top of it. We process it through many different fabrication steps in order to obtain waveguides, resonators, filters, and all sort of CMOS-compatible optical devices.

In order to achieve dynamic behavior, we change the index of refraction of the waveguide. There are two mechanisms that we use, depending on the application that the component is designed to address.

The first mechanism we use for changing the index of refraction relies on the free-carrier plasma dispersion on silicon [8]. We inject or extract free-carriers by

applying a voltage on pn or p-i-n junctions fabricated across the silicon waveguide. The index of refraction can be changed by reverse biasing the junction, which changes the size of the depletion region, or by forward biasing the diode, which suppresses the depletion region and causes a flow of electrons and holes across the waveguide. This mechanism has a response time that can have been already shown to achieve frequencies as high as 30 GHz [9], which makes it suitable for applications as modulators [10, 11] and switches [12, 13, 14]. It can achieve refractive index change on the order of -10^{-3} [13], being necessary to account for the losses caused by free-carrier absorption in the design [8].

The second mechanism we use relies on the thermo-optical coefficient of silicon [15]. As the temperature increases, the bandgap decreases [16, 17], changing the refractive index of the waveguide. Thermal tuning is usually achieved by having a resistor (heater) closeby the waveguide, with a response time depending on the distance between waveguide and heaters. A typical value for response time is about 10 µs [18], not fast enough for high speed modulators, but good enough for reconfigurable filters and for fine tuning to compensate both temperature fluctuation and variation in the fabrication process. It can achieve refractive index change on the order of +10^{-2}, with negligible loss added to the device [19].

1.3 Focus and organization of this dissertation

In this introductory chapter we present the theoretical background common to most of the devices we discuss in this dissertation. Starting from Maxwell's Equations, we explore very simple and important tools for the design of optical

devices: Effective Index Method, Supermode Theory, and Coupling between Curved Waveguides. We briefly present the coefficients for Sellmeier Equations of the materials used in this work and head into an exposition of a few passive optical devices which are building blocks for the dynamic devices we discuss.

In chapter two we explore a hitless switch, which consists on a device with two coupled microring resonators that can have its transfer function changed from a band-pass filter to an all-pass filter. We derive all the equations necessary for the synthesis of the filter, fabricate it and confirm the theoretically predicted behavior of the transfer function. We discuss the limitations caused by the thermo-optical effect counteracting the index change provided by free-carrier plasma dispersion, as well as other operation limits and synthesis charts relating insertion loss and extinction ratio for the through and drop ports of the filter to the synthesis parameters.

In chapter three we demonstrate that it is possible to thermally tune a second-order microring resonator filter across half of the C-Band while keeping its bandwidth and extinction ratio the same as in the original wavelength. We start by analyzing the effects of a large thermal tunning on the transfer function of coupled microring resonators. We obtain a model which predicts the effect that different configurations of thermal distribution causes on the coupling between waveguides. We test some configurations of thermal distribution and observe that, after tuning across a large spectral range, negligible variation of the transfer function for two of them. We also observe, both in simulation and in devices we fabricate, the enhancement of the heat diffusion from heaters to waveguides by the use of a thin silicon slab connecting them. We finally compare metallic heaters with doped-silicon heaters, in order to provide a guideline

to increase the tunability range of such devices.

In chapter four we study a modified coupled microring filter, which doubles the original Free Spectral Range and is capable of non-blocking reconfiguration. We observe that by changing the typical one-point coupling between a bus waveguide and a ring to a two-point coupling, a wavelength dependent coupling is obtained. This feature is used to double the Free Spectral Range of the filter. We provide synthesis equations and compare a few possibilities of transmission functions related to choices in the design. We finally show that such a device can also work as a hitless switch, and we also perform non-blocking tuning of the device to a new resonance wavelength.

In chapter five we present an electrically-driven optical-isolator. Its principle of operation is based on mode conversion provided by a traveling-wave modulation pattern. The traveling wave only matches the difference between two guided modes when the optical signal travels in one direction, converting the original symmetric mode to an anti-symmetric mode, which then is filtered. We present the theoretical background required to design it, as well as the intricate electrical design required to provide the proper permittivity modulation of the waveguide. Finally we present the parameters chosen, describe the fabrication, show the results obtained and discuss ways to improve its performance in the future.

1.4 Theoretical Background

In this section we briefly present Maxwell's Equations and the Transverse Electrical (TE) and the Transverse Magnetic (TM) solutions for slab waveguides. We

present the Effective Index Method, which is used to obtain a slab waveguide model for channel and ridge waveguides. We also show the transcendental equations for a three-layer symmetric waveguide and for a five-layer symmetric waveguide. We derive the equations regarding coupling for curved waveguides, an important tool for the proper design of the coupling between a microring resonator and a bus waveguide. Finally we show the coefficients for the Sellmeier Equation used to model the material dispersion of silicon and silicon dioxide.

1.4.1 Maxwell's Equations

The foundations of electromagnetism are summarized in a compact set of equations, known as Maxwell's equations. Their differential form is given by:

$$\nabla \times \vec{E} = -\frac{\partial \vec{B}}{\partial t} \tag{1.1a}$$

$$\nabla \times \vec{H} = \vec{J} + \frac{\partial \vec{D}}{\partial t} \tag{1.1b}$$

$$\nabla \cdot \vec{D} = \rho \tag{1.1c}$$

$$\nabla \cdot \vec{B} = 0 \tag{1.1d}$$

with constitutive relations

$$\vec{B} = \mu \vec{H} \tag{1.2a}$$

$$\vec{D} = \varepsilon \vec{E} \tag{1.2b}$$

Description and units of the variables used above are listed in Table 1.1.

In this work we deal mostly with linear, isotropic, source-free medium. The

Table 1.1: Maxwell's equations variables and constants.

Symbol	Description	SI Unit
$\vec{E}$	Electric field	V/m
$\vec{H}$	Magnetic field	A/m
$\vec{D}$	Electric displacement field	C/m^2
$\vec{B}$	Magnetic induction	Wb/m^2
$\vec{J}$	Current density	A/m^2
ρ	Charge density	C/m^3
ε	Permittivity	F/m
μ	Permeability	H/m

general form of the macroscopic Maxwell's equation for such a medium is [20]:

$$\nabla \times \vec{E} = -\frac{\partial \vec{B}}{\partial t} \tag{1.3a}$$

$$\nabla \times \vec{H} = \frac{\partial \vec{D}}{\partial t} \tag{1.3b}$$

$$\nabla \cdot \vec{D} = 0 \tag{1.3c}$$

$$\nabla \cdot \vec{B} = 0 \tag{1.3d}$$

An important case which provides insight for more detailed calculation is the analysis of two-dimensional (2D) medium. In this particular case, the equations for an isotropic, lossless medium, are simplified to:

$$\nabla \times \vec{E} = -\mu_0 \frac{\partial \vec{H}}{\partial t} \tag{1.4}$$

$$\nabla \times \vec{H} = \varepsilon_0 n^2 \frac{\partial \vec{E}}{\partial t} \tag{1.5}$$

Where μ_0 is the permeability in free space, ε_0 is the permittivity in free space, and n is the refractive index of the medium.

Maxwell's equation for two-dimensional waveguides can be divided in two sets, one for Transverse Electric field (TE) and another for transverse magnetic field (TM). For propagation in the z direction of an orthogonal coordinate system (x, y, z), the harmonic behavior of the electromagnetic fields can be set apart from the cross-section profile of the fields:

$$\vec{E}(x, y, z, t) = \vec{E}(x, y) \cdot e^{i(\omega t - \beta z)} \tag{1.6a}$$

$$\vec{H}(x, y, z, t) = \vec{H}(x, y) \cdot e^{i(\omega t - \beta z)} \tag{1.6b}$$

Where β is the propagation wavenumber in m^{-1} and ω is the oscillation frequency of the electromagnetic wave in rad/s. Further simplification comes from the 2D nature of the waveguide, which requires $\partial/\partial y = 0$; and from the solution for harmonic fields, yielding $\partial/\partial t = i\omega$ and $\partial/\partial z = -i\beta$. The final set of equations for TE waves is:

$$\begin{aligned} \frac{\partial^2 E_y}{\partial x^2} + (k_0^2 n^2 - \beta^2) E_y &= 0 \\ H_x &= -\frac{\beta}{\omega \mu_0} E_y \\ H_z &= -\frac{1}{i\omega\mu_0} \frac{\partial E_y}{\partial x} \end{aligned} \tag{1.7}$$

The final set of equations for TM waves is:

$$\begin{aligned} \frac{\partial^2 H_y}{\partial x^2} + (k_0^2 n^2 - \beta^2) H_y &= 0 \\ E_x &= \frac{\beta}{\omega \varepsilon n^2} H_y \\ E_z &= \frac{1}{i\omega\varepsilon n^2} \frac{\partial H_y}{\partial x} \end{aligned} \tag{1.8}$$

where

$$k_0 = \frac{2\pi}{\lambda} \tag{1.9}$$

The equations above can be used for any refractive index distribution. In the particular case of channel and ridge waveguides, where there is an abrupt

transition between materials, we need to use the boundary conditions [21, 20]:

$$\begin{aligned} \hat{s} \times (\vec{E}_2 - \vec{E}_1) &= 0 \\ \hat{s} \times (\vec{H}_2 - \vec{H}_1) &= 0 \\ \hat{s} \cdot (\vec{B}_2 - \vec{B}_1) &= 0 \\ \hat{s} \cdot (\vec{D}_2 - \vec{D}_1) &= 0 \end{aligned} \tag{1.10}$$

where $\hat{s}$ is the vector normal to the interface, and the indices 1 and 2 represent each side of an interface. The equations above state the continuity of the tangential component of the electric ($\vec{E}$) and magnetic fields ($\vec{H}$) and of the normal components of the electric displacement ($\vec{D}$) and magnetic induction ($\vec{B}$).

1.4.2 Effective Index Method

Mathematically, electromagnetic wave propagation is usually represented by a set of orthogonal modes. There is certainly no lack of precise numerical methods for mode calculations. However, simple approaches for first guess are essential to save time before heading into computational-expensive time-demanding simulations. A particularly useful approach comes from Effective Index Method, where a three dimensional structure is approximated by two dimensional slab waveguides. Its most obvious feature comes from its simplicity: the effective index can be obtained by solving sequentially two simple transcendental equations for slab modes.

Solution for a quasi-TE mode requires first a TE slab calculation, which provides an intermediate index of refraction n_{int}, followed by a TM slab calculation using n_{int}. Solution for a quasi-TM mode requires first a TM slab calculation, which provides an intermediate index of refraction n_{int}, followed by a TE slab

calculation using n_{int}. An schematic of this approach is shown in Fig. 1.1.

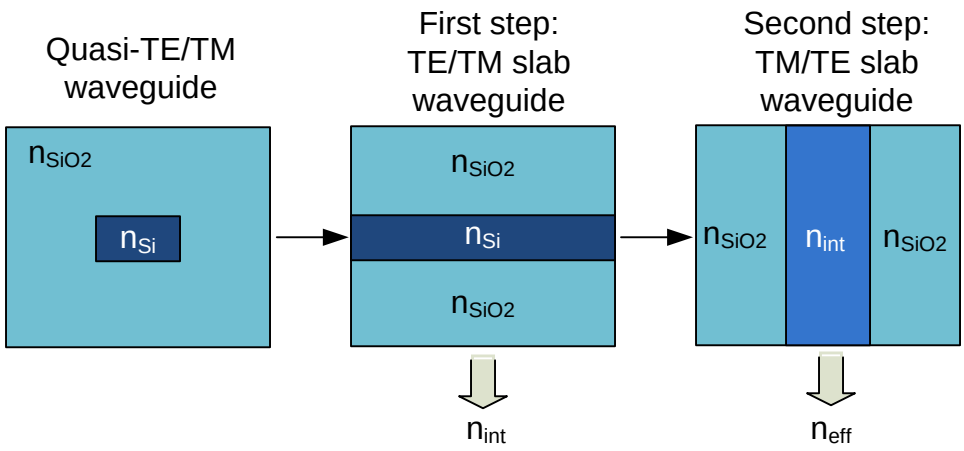

Figure 1.1: Effective index schematics. The original structure is converted first into a horizontal set of slabs. An intermediate index of refraction n_{int} is obtained, which is used as the central index in the vertical set of slabs. The effective index of the structure n_{eff} is then obtained.

Eq. 1.7 for TE modes and Eq. 1.8 for TM modes, together with the boundary conditions presented at Eq. 1.10, lead to the following transcendental equations for even modes and for odd modes, respectively:

$$\kappa h \sin(\kappa h) = \cos(\kappa h) \left(\frac{n_{in}}{n_{out}}\right)^{2\sigma} \sqrt{\left(k_0 \frac{h}{2}\right)^2 (n_{in}^2 - n_{out}^2) - (\kappa h)^2} \tag{1.11}$$

$$\kappa h \cos(\kappa h) \left(\frac{n_{in}}{n_{out}}\right)^{2\sigma} = -\sin(\kappa h) \sqrt{\left(k_0 \frac{h}{2}\right)^2 (n_{in}^2 - n_{out}^2) - (\kappa h)^2} \tag{1.12}$$

Where κ is the transverse wave constant, h is the width of the slab, n_{in} is the index of refraction of the inner slab (n_{Si} in the first step and n_{int} in the second step), n_{out} is the index of refraction of the outter slabs (n_{SiO2} in both steps), and σ is zero for TM modes and one for TE modes.

From the solution of the transcendental equations we can calculate all the

parameters related to the wave propagation:

$$\beta = \sqrt{(k_0 n_{in})^2 - \kappa^2} \tag{1.13}$$

$$\gamma = \sqrt{k_0^2(n_{in}^2 - n_{out}^2) - \kappa^2} \tag{1.14}$$

$$n_{eff} = \frac{\beta}{k_0} \tag{1.15}$$

Where γ is the evanescent field decay constant, and n_{eff} is the effective index of refraction of the mode calculated. The electric field distribution across the waveguide is given by:

$$E(x) = \frac{1}{n_{SiO_2}^{2\sigma}} \begin{cases} e^{-\gamma\left(x-\frac{w}{2}\right)} & \text{if } \frac{w}{2} < x \\ \frac{n_{SiO_2}^{2\sigma}}{n_{int}^{2\sigma}} \frac{\cos(\kappa x)}{\cos\left(\kappa\frac{w}{2}\right)} & \text{if } -\frac{w}{2} \leq x \leq \frac{w}{2} \\ e^{\gamma\left(x+\frac{w}{2}\right)} & \text{if } x < -\frac{w}{2} \end{cases} \tag{1.16}$$

Where w is the width of the waveguide. The 2D field distribution, seeing as a simplification of the 3D real distribution, is depicted in Fig. 1.2.

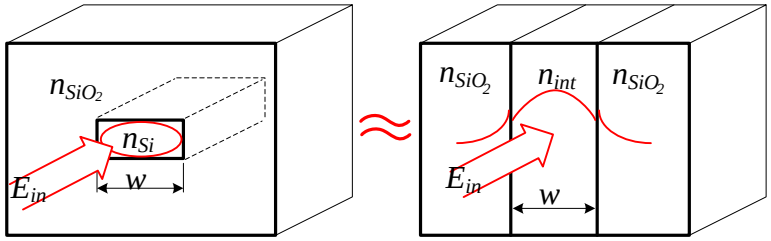

Figure 1.2: Representation of the field distribution in a 2D structure.

The normalization factor, required for proper calculations of inner product between modes, has an analytical expression for slab waveguides:

$$C = \sqrt{\eta_0/(n_{eff} \cdot I)} \tag{1.17}$$

with

$$I = \frac{1}{n_{int}^{4\sigma}} \left[\frac{w}{4\cos^2\left(\kappa\frac{w}{2}\right)} + \frac{\sin\left(\kappa w\right)}{4\kappa\cos^2\left(\kappa\frac{w}{2}\right)} \right] + \frac{1}{n_{SiO_2}^{4\sigma}} \frac{1}{2\gamma} \tag{1.18}$$

where η_0 is the impedance of free space.

1.4.3 Supermode Theory

Another important type of waveguide used in this work is made of two parallel high-index material beams surrounded by low-index material. They can be approximated by a 5-layer slab waveguide, as shon in Fig. refsuper(left). In this case, the original modes of the each waveguide are split into a symmetric and an anti-symmetric supermodes, as shown in Fig. 1.3(right).

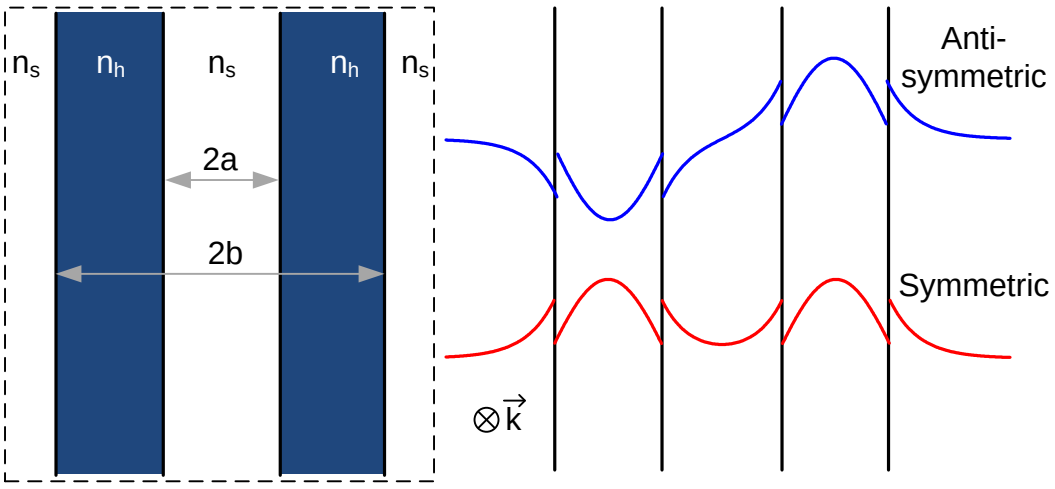

Figure 1.3: In the left, we show the geometry with two separated slabs with higher index of refraction n_h surrounded by slabs with lower index of refraction n_s. In the right, we show symmetric and anti-symmetric TE modes suported by the structure.

Solution for the boundary conditions of such structures leads to the follow-

ing transcendental equations for the symmetric (or even) mode:

$$-\sinh(\gamma_s a)\cos[\kappa_h(b-a)] + \left(\frac{n_s}{n_h}\right)^{2\sigma}\frac{\kappa_h}{\gamma_s}\cosh(\gamma_s a)\sin[\kappa_h(b-a)] - \cosh(\gamma_s a)\cos[\kappa_h(b-a)] - \left(\frac{n_h}{n_s}\right)^{2\sigma}\frac{\gamma_s}{\kappa_h}\sinh(\gamma_s a)\sin[\kappa_h(b-a)] = 0 \quad (1.19)$$

And for the anti-symmetric (or odd) mode:

$$-\cosh(\gamma_s a)\cos[\kappa_h(b-a)] - \left(\frac{n_s}{n_h}\right)^{2\sigma}\frac{\kappa_h}{\gamma_s}\sinh(\gamma_s a)\sin[\kappa_h(b-a)] + \sinh(\gamma_s a)\cos[\kappa_h(b-a)] + \left(\frac{n_h}{n_s}\right)^{2\sigma}\frac{\gamma_s}{\kappa_h}\cosh(\gamma_s a)\sin[\kappa_h(b-a)] = 0 \quad (1.20)$$

With

$$\gamma_s = \sqrt{\beta^2 - k_0^2 n_s^2} \quad (1.21)$$

$$\beta = \sqrt{k_0^2 n_h^2 - \kappa_h^2} \quad (1.22)$$

Where n_h is the index of refraction of the high-index material, n_s is the refractive index of the surrounding low-index material, a is the distance from the center to the inner part of the high-index material, and b is the distance from the center to the outer part of the high-index material.

The expression for the electric field for the even mode is:

$$E_{even} = \begin{cases} \frac{1}{n_s^{2\sigma}} e^{-\gamma_h(x-b)} & \text{if } b \leqslant x \\ \frac{1}{n_h^{2\sigma}} \frac{\cos\left[\kappa_h\left(x-\frac{b+a}{2}\right)\right]}{\cos\left[\kappa_h\left(\frac{b-a}{2}\right)\right]} & \text{if } a \leqslant x < b \\ \frac{1}{n_s^{2\sigma}} \frac{\cosh(\gamma_h x}{\cosh(\gamma_h a)} & \text{if } -a \leqslant x < a \\ \frac{1}{n_h^{2\sigma}} \frac{\cos\left[\kappa_h\left(x+\frac{b+a}{2}\right)\right]}{\cos\left[\kappa_h\left(\frac{b-a}{2}\right)\right]} & \text{if } -b \leqslant x < -a \\ \frac{1}{n_s^{2\sigma}} e^{\gamma_h(x+b)} & \text{if } x \leqslant -b \end{cases} \quad (1.23)$$

The expression for the electric field for the odd mode is:

$$E_{odd} = \begin{cases} \frac{1}{n_s^{2\sigma}} e^{-\gamma_h (x-b)} & \text{if } b \leqslant x \\ \frac{1}{n_h^{2\sigma}} \frac{\cos\left[\kappa_h \left(x - \frac{b+a}{2}\right)\right]}{\cos\left[\kappa_h \left(\frac{b-a}{2}\right)\right]} & \text{if } a \leqslant x < b \\ \frac{1}{n_s^{2\sigma}} \frac{\sinh(\gamma_h x}{\sinh(\gamma_h a)} & \text{if } -a \leqslant x < a \\ \frac{1}{n_h^{2\sigma}} \frac{-\cos\left[\kappa_h \left(x + \frac{b+a}{2}\right)\right]}{\cos\left[\kappa_h \left(\frac{b-a}{2}\right)\right]} & \text{if } -b \leqslant x < -a \\ \frac{1}{n_s^{2\sigma}} e^{\gamma_h (x+b)} & \text{if } x \leqslant -b \end{cases} \tag{1.24}$$

1.4.4 Coupling between Curved Waveguides

Directional couplers are basic building blocks for microring resonators and Mach-Zenhder Interferometers. The solution for parallel waveguides starting with electrical field at only one of the inputs of a directional coupler (as shown schematically in the left side of Fig. 1.4) leads to an oscillatory behavior of the field, going from one waveguide to the other with periodicity given by the coupling constant K_c [22]:

$$a_1(z) = \cos(K_c z) \tag{1.25a}$$

$$a_2(z) = -\imath \sin(K_c z) \tag{1.25b}$$

Where a_1 is the normalized field amplitude of mode in the input waveguide, and a_2 is the normalized field amplitude of the mode in the coupled waveguide. Therefore, the total coupling is obtained considering the total phase $\theta_c = K_c z$ accumulated by the field propagating in the coupling region.

Given that the field decays exponentially outside of the core of the waveguide, the coupling constant also changes as [23]

$$K_c(d) = K_{c0} e^{-\gamma(d-d_0)} \tag{1.26}$$

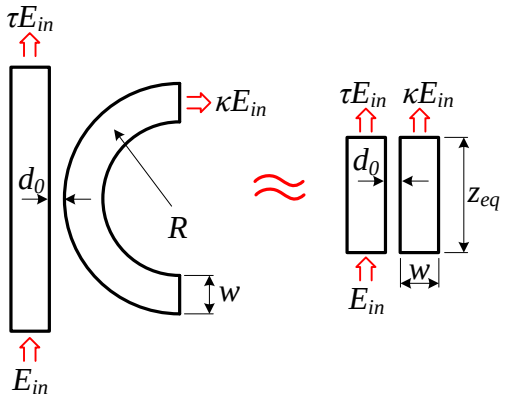

Figure 1.4: Equivalent parallel-waveguide model for coupling in a curved waveguide.

where K_{c0} is the coupling when the waveguides are at a distance d_0, and γ is the decay constant of the evanescent field. Therefore, for the case of a straight waveguide coupling to a curved waveguide, where the distance between waveguides changes as

$$d(z) = d_0 + R - \sqrt{R^2 - z^2} \tag{1.27}$$

we need to perform an integral to obtain the total phase:

$$\theta_c = K_{c0} \int_{-R}^{R} e^{-\gamma(R-\sqrt{R^2-z^2})} dz \tag{1.28}$$

For the first time, to our knowledge, we obtain a solution in Bessel series for this integral. We start with the change of variables

$$z = R\sin(\theta) \tag{1.29}$$

which leads to

$$\int_{-R}^{R} e^{\gamma\sqrt{R^2-z^2}} dz = \int_{-\pi/2}^{\pi/2} e^{\gamma R\cos(\theta)} R\cos(\theta) d\theta \tag{1.30}$$

For $\gamma = \imath B$, we have

$$\begin{aligned}
&\int_{-\pi/2}^{\pi/2} e^{\imath BR\cos(\theta)} \cos R(\theta) d\theta = \\
&\int_{-\pi/2}^{\pi/2} \cos(BR\cos(\theta)) \cos R(\theta) d\theta + \imath \int_{-\pi/2}^{\pi/2} \sin(BR\cos(\theta)) \cos R(\theta) d\theta = \\
&\int_{-\pi/2}^{\pi/2} \cos(BR\cos(\theta)) \cos R(\theta) d\theta + \imath\pi J_1(BR)
\end{aligned} \tag{1.31}$$

To solve the remaining integral, we have from properties of Bessel functions that

$$\cos[x\cos(\phi)] = J_0(x) + 2\sum_{k=1}^{\infty}(-1)^k J_{2k}(x)\cos(2k\phi) \tag{1.32}$$

Therefore

$$\begin{aligned}
&\int_{-\pi/2}^{\pi/2} \cos[BR\cos(\theta)] d\theta = \\
&\int_{-\pi/2}^{\pi/2} J_0(BR) cos(\theta) d\theta + 2\sum_{k=1}^{\infty}(-1)^k J_{2k}(BR) \int_{-\pi/2}^{\pi/2} \cos(2k\theta)\cos(\theta) d\theta
\end{aligned} \tag{1.33}$$

After performing the integral of the cosine terms, we obtain

$$\int_{pi/2}^{\pi/2} e^{\imath BR\cos(\theta)} \cos R(\theta) d\theta = R\left[2J_0(BR) - 4\sum_{k=1}^{\infty} \frac{J_{2k}(BR)}{(2k)^2 - 1} + \imath\pi J_1(BR)\right] \tag{1.34}$$

From the relations

$$\begin{aligned}
\imath J_1(-\imath\gamma R) &= I_1(\gamma R) \\
J_0(-\imath\gamma R) &= I_0(\gamma R) \\
J_2(-\imath\gamma R) &= -I_2(\gamma R) \\
J_4(-\imath\gamma R) &= I_4(\gamma R) \\
&\vdots
\end{aligned} \tag{1.35}$$

we finally obtain the total coupling phase

$$\theta_c = K_{c0} R\left[2I_0(\gamma R) - 4\sum_{k=1}^{\infty} \frac{(-1)^k I_{2k}(\gamma R)}{(2k)^2 - 1} + \pi I_1(\gamma R)\right] \tag{1.36}$$

The value of γ can be obtained from the symmetric and anti-symmetric refractive indices for two distinct distances d_1 and d_2 as

$$\gamma = \frac{1}{d_2 - d_1} \ln \left(\frac{n_{effsym}(d_1) - n_{effasym}(d_1)}{n_{effsym}(d_2) - n_{effasym}(d_2)} \right) \tag{1.37}$$

where n_{effsym} is the effective index of the symmetric mode in the coupling region, and where $n_{effasym}$ is the effective index of the anti-symmetric mode in the coupling region. Since the coupling follows a exponential decay with constant A, it is straight forward to obtain the desired distance between waveguides for a given desired coupling value.

Another way to obtain the coupling value is by approximating 1.27 as

$$d(z) \approx d_0 + \frac{z^2}{2R} \tag{1.38}$$

The coupling phase calculation is now a Gaussian integral, which can be performed from $-\infty$ to ∞. The final result is [24]

$$\theta_c \approx K_{c0} \sqrt{\frac{2\pi R}{\gamma}} \tag{1.39}$$

For two curved waveguides in the coupling region, the only change is a factor of two appears multiplying γ.

1.4.5 Sellmeier Equation Coefficients

From considerations of the resonance frequency for each material, it is possible to derive the material dispersion of dielectrics from first principles [20], which can be checked experimentally using an Ellipsometer. Any application where a large span of wavelengths is required needs to take into account the material dispersion.

A typical way to model the dispersion of materials is by the use of Sellmeier's equation, which is given by:

$$n^2 = A + \sum_k \frac{G_k \lambda^2}{\lambda^2 - \lambda_k^2} \tag{1.40}$$

Tabulated values for most materials can be found in the literature. Table 1.2 presents the coefficients for silicon (Si) and silicon dioxide (SiO_2), which are the materials used throughout this work. Figure 1.5 shows the index of refraction

Table 1.2: Sellmeier's equation coefficients for Si and SiO_2.

	Si	SiO_2	$SiO_2(\mathrm{GSI-PECVD})$
A	1	1	1
G_1	10.66842933	0.6961663	0.69617
$\lambda_1(\mu m)$	0.003015116485	0.0684043	0.0684
G_2	0.003043475	0.4079426	0.40794
$\lambda_2(\mu m)$	0.0113475115	0.1162414	0.1162
G_3	1.54133408	0.8974794	0.89748
$\lambda_3(\mu m)$	11.04	9.896161	9.8962

using the coefficients presented in Table 1.2. It is worth to notice the difference between tabulated values for silicon dioxide and the value typically obtained in our fabrication processes.

1.5 Passive devices

In this section we describe important characteristics of three passive devices used throughout this dissertation: the microring resonator, the Mach-Zehnder

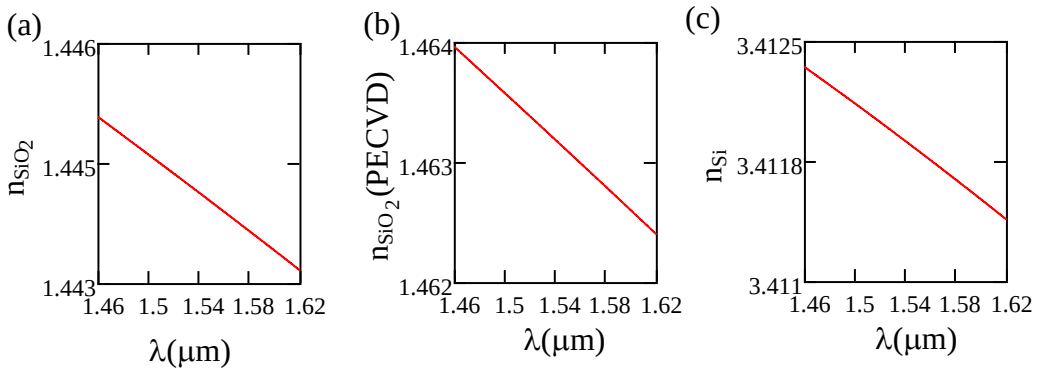

Figure 1.5: (a) Refractive index of bulk SiO_2. (b) Typical refractive index of undoped GSI-PECVD deposited SiO_2 obtained at Cornell Nanofabrication Facility.

(c) Refractive index of bulk Si.

Interferometer and the Multi-Mode Interference device.

1.5.1 Microring Resonator

Microring resonators are frequency-dependent optical components which, through an interference mechanism, can enhance the electric field intensity inside its structure to levels higher than the input intensity. They have a passband filter response which depends on losses (scattering, material absorption, tap waveguides), and a Free Spectral Range which depends on its size and effective index of refraction.

There are two interesting ways to solve the equations for a simple ring resonator: a steady-state approach, which neglects the dynamics of the field build-up mechanism, and a time-domain approach, where the temporal response is obtained and steady-state behavior can be verified by simply making $t \to \infty$.

In time domain, the time constant which determines the ring resonator char-

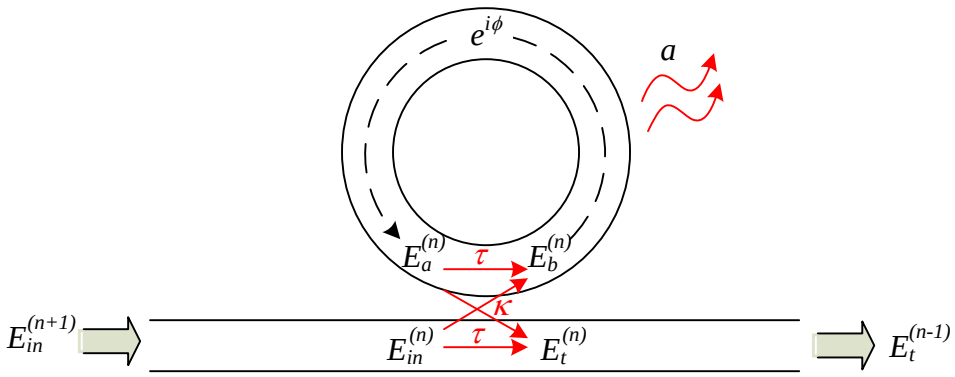

Figure 1.6: Microring resonator.

acteristics is the roundtrip, which is tied to the length of the propagation delay of the resonator by the relation:

$$t_{rt} = \frac{L_r n_{eff}}{c_0} \tag{1.41}$$

Where t_{rt} is the roundtrip time constant, L_r is the length of the resonator, n_{eff} is the effective index of refraction of the waveguide, and c_0 is the speed of light in free space.

The equations necessary to obtain the transmitted field and build-up field after n roundtrips, considering the convention displayed in Fig. 1.6, are:

$$E_t^{(n)} = \tau E_{in}^{(n)} - \imath\kappa E_b^{(n)} \tag{1.42a}$$

$$E_a^{(n)} = \tau E_b^{(n)} - \imath\kappa E_{in}^{(n)} \tag{1.42b}$$

$$E_b^{(n)} = E_a^{(n-1)} a e^{\imath\phi} \tag{1.42c}$$

Where κ is the coupling constant, τ is the transmission constant. For a lossless coupling κ and τ are such that

$$\tau^2 + \kappa^2 = 1, \tag{1.43}$$

E_t is the electrical field at the output (usually known as through port), E_{in} is the electrical field at the input, E_a is the electrical field inside the resonator right af-

ter the coupling region, E_b is the electrical field inside the resonator right before the coupling region, the indices (n), $(n-1)$ is the number of complete roundtrip times t_{rt} computed, ϕ is the total optical phase accumulated by a field propagating inside the resonator, given by

$$\phi = \frac{2\pi}{\lambda} n_{eff} L_r \tag{1.44}$$

a is the loss term, which can be expressed as

$$a = e^{\frac{\alpha}{2} L_r}, \tag{1.45}$$

where α is the field propagation loss in m^{-1}.

The recursive equations above can be expanded as

$$E_t^{(n)} = \tau E_{in}^{(n)} - i\kappa a e^{i\phi}(-i\kappa E_{in}^{(n-1)} + \tau a e^{i\phi}(-i\kappa E_{in}^{(n-2)} + \cdots + \tau a e^{i\phi}(-i\kappa E_{in}^{(0)}) \dots)) \tag{1.46a}$$

$$E_a^{(n)} = -i\kappa E_{in}^{(n)} + \tau a e^{i\phi}(-i\kappa E_{in}^{(n-1)} + \tau a e^{i\phi}(-i\kappa E_{in}^{(n-2)} + \cdots + \tau a e^{i\phi}(-i\kappa E_{in}^{(0)}) \dots)) \tag{1.46b}$$

For the particular case when $E_{in}^{(n)} = 1$ for all n, it simplifies to:

$$E_t^{(n)} = \tau - i\kappa a e^{i\phi}(-i\kappa)(1 + \tau a e^{i\phi} + (\tau a e^{i\phi})^2 + \cdots + (\tau a e^{i\phi})^{n-1}) \tag{1.47a}$$

$$E_a^{(n)} = -i\kappa a e^{i\phi}(-i\kappa)(1 + \tau a e^{i\phi} + (\tau a e^{i\phi})^2 + \cdots + (\tau a e^{i\phi})^{n-1}) \tag{1.47b}$$

These series have a closed form, which is given by:

$$E_t^{(n)} = \frac{\tau - a e^{i\phi} + \kappa^2 a e^{i\phi}(\tau a e^{i\phi})^n}{1 - \tau a e^{i\phi}} \tag{1.48a}$$

$$E_a^{(n)} = -i\kappa \frac{1 - (\tau a e^{i\phi})^{n+1}}{1 - \tau a e^{i\phi}} \tag{1.48b}$$

Figure 1.7 shows the stepwise response in time domain for the through port field and for the build-up field inside the ring, as well as the frequency response

at different moments during the transient. As any Infinite Response Filter, the spectrum changes as time progresses, until a steady-state condition is achieved.

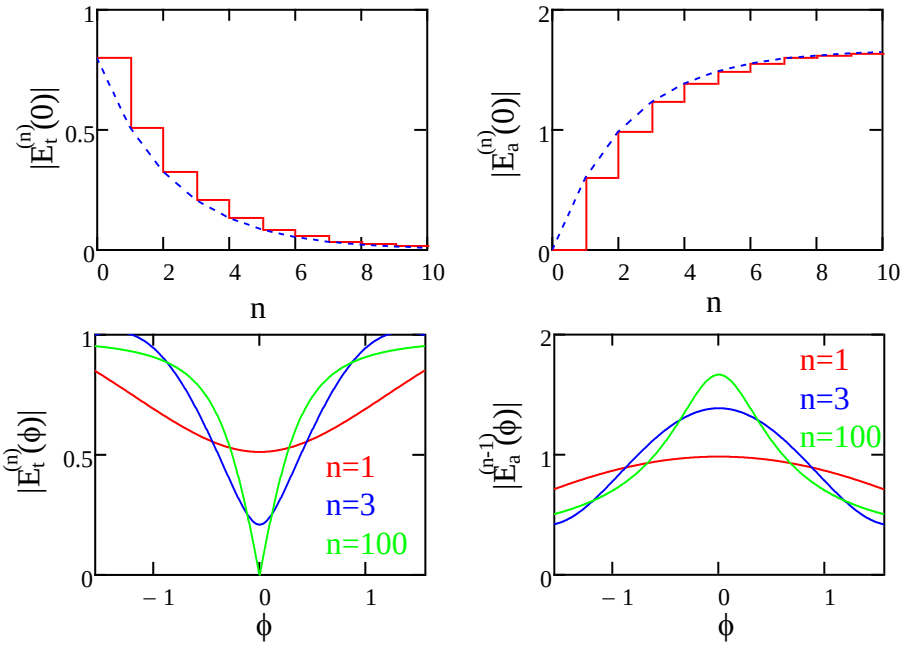

Figure 1.7: Time and frequency domain response of a ring resonator. Top left shows the discrete response of the through port (red), as well the exponential fit (blue). Top right shows the discrete build-up field inside the ring (red), as well the exponential fit (blue). Bottom left shows the field intensity of the through port as a function of phase at three distinct moments: after the first roundtrip (red), after the third (blue) and after the hundredth (green). Bottom right shows the field build-up intensity as a function of phase at three distinct moments: after the first roundtrip (red), after the third (blue) and after the hundredth (green).

For $n \to \infty$ we obtain the steady-state solution:

$$E_t^{(\infty)} = \frac{\tau - ae^{i\phi}}{1 - \tau a e^{i\phi}} \tag{1.49a}$$

$$E_a^{(\infty)} = \frac{-i\kappa}{1 - \tau a e^{i\phi}} \tag{1.49b}$$

In resonance, the time dependence of the build-up field inside the microring is given by:

$$E_a^{(n)} = -i\kappa \frac{1-(\tau a)^{n+1}}{1-\tau a} \tag{1.50}$$

From the equations above it is possible to extract the photon lifetime and the Quality Factor of the resonator. Given that the number of roundtrip for which the field inside the microring reaches $1-e^{-1}$ of its maximum is

$$(n+1) = \frac{-1}{\ln(\tau a)}, \tag{1.51}$$

we use the roundrip time constant t_{rt} and obtain the photon lifetime:

$$t_{lt} = -\frac{L_r n_{eff}}{c_0 ln(\tau a)} \tag{1.52}$$

Quality factor (Q) of a microring resonator is obtained from

$$\frac{|E_a^{(\infty)}(\Delta\phi/2)|^2}{|E_a^{(\infty)}(0)|^2} = \frac{1}{2} \tag{1.53}$$

The final result, after some algebraic manipulation, is:

$$\cos(\Delta\phi/2) = \frac{1-4\tau a+(\tau a)^2}{-2\tau a} \tag{1.54}$$

After expanding it up to the second term in Taylor's Series, we obtain

$$\Delta\phi = 2\frac{1-\tau a}{\sqrt{\tau a}} \tag{1.55}$$

and the expression for the Q is

$$Q = \frac{\phi}{\Delta\phi} = \frac{\sqrt{\tau a}}{1-\tau a}\pi n_{eff} L_r \tag{1.56}$$

For critical coupling it simplifies to

$$\Delta\phi = 2\alpha L_r \tag{1.57}$$

The Quality factor for critical coupling Q_{cr} is therefore given by

$$Q_{cr} = \frac{\pi n_{eff}}{\lambda\alpha} \tag{1.58}$$

The Free-Spectral-Range (FSR) of a microring resonator is obtained considering the distance between two consecutive resonances:

$$FSR = \lambda_m - \lambda_{m+1} \tag{1.59}$$

Where λ_m and λ_{m+1} are the m$^{\text{th}}$ and (m+1)$^{\text{th}}$ resonances, extracted from:

$$L_r n_{eff}(\lambda_m) = \lambda_m m \tag{1.60a}$$

$$L_r n_{eff}(\lambda_{m+1}) = \lambda_{m+1}(m+1) \tag{1.60b}$$

From the definition of group index [20]

$$n_g = n_{eff} - \lambda_m \frac{dn_{eff}}{d\lambda_m}, \tag{1.61}$$

and after some algebraic manipulation, we finally obtain

$$FSR = \frac{\lambda^2}{n_g L_r} \tag{1.62}$$

1.5.2 Mach-Zehnder Interferometer

A Mach-Zehnder Interferometer (MZI) is a device which translates material difference between two optical paths into the amplitude of the output signal. The optical paths may differ in length or in the value of the effective index of refraction. The MZI can be divided in three parts: one directional coupler at the input, one directional coupler at the output, and two arms (delay lines) connecting them to each other (Fig. 1.8). Each part is constituted by two inputs and two outputs. Since all elements are passive, relation between input and outputs can be written in a matricial form.

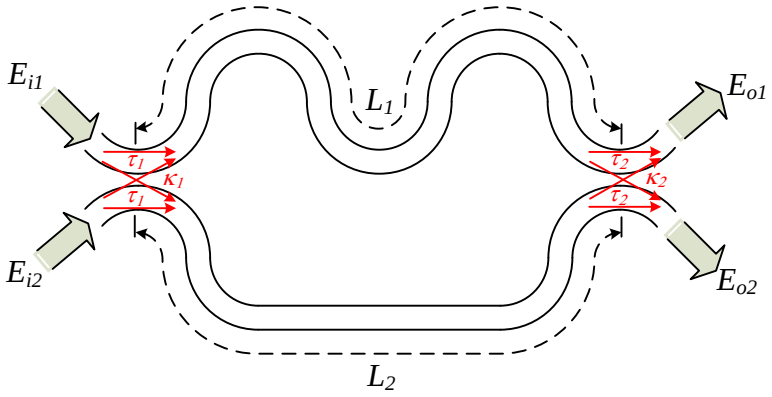

Figure 1.8: Mach-Zehnder Interferometer.

The relations between input and output of each part are given by:

$$\text{First coupler: } \begin{pmatrix} E_{a1} \\ E_{a2} \end{pmatrix} = \begin{pmatrix} \tau_1 & i \cdot \kappa_1 \\ i \cdot \kappa_1 & \tau_1 \end{pmatrix} \begin{pmatrix} E_{i1} \\ E_{i2} \end{pmatrix} \tag{1.63}$$

$$\text{Delay lines: } \begin{pmatrix} E_{b1} \\ E_{b2} \end{pmatrix} = \begin{pmatrix} e^{i\cdot\varphi_1} & 0 \\ 0 & e^{i\cdot\varphi_2} \end{pmatrix} \begin{pmatrix} E_{a1} \\ E_{a2} \end{pmatrix} \tag{1.64}$$

$$\text{Second coupler: } \begin{pmatrix} E_{o1} \\ E_{o2} \end{pmatrix} = \begin{pmatrix} \tau_2 & i \cdot \kappa_2 \\ i \cdot \kappa_2 & \tau_2 \end{pmatrix} \begin{pmatrix} E_{b1} \\ E_{b2} \end{pmatrix} \tag{1.65}$$

where

$$\varphi_1 = \frac{2\pi n_{eff1}}{\lambda} L_1 \tag{1.66}$$

$$\varphi_2 = \frac{2\pi n_{eff2}}{\lambda} L_2, \tag{1.67}$$

where τ_1 and κ_1 are the transmission and coupling coefficients of the first coupler, respectively; τ_2 and κ_2 are the transmission and coupling coefficients of the first coupler, respectively; φ_1 is the optical length of the first delay line, L_1 is its physical length and n_{eff1} is its effective index of refraction; φ_2 is the optical length of the second delay line, L_2 is its physical length and n_{eff2} is its effective index of refraction; and λ is the wavelength of the input signal in free space. In

the equations above, the output fields are at the left-hand side of the equations, and the input at the right-hand side. The indices 1 and 2 for the fields identify which of the input and output ports they represent.

The overall transfer function is obtained by cascading the matrices, leading to:

$$\begin{pmatrix} E_{o1} \\ E_{o2} \end{pmatrix} = \begin{pmatrix} \tau_1\tau_2 e^{i\cdot\varphi_1} - \kappa_1\kappa_2 e^{i\cdot\varphi_2} & i\cdot(\kappa_1\tau_2 e^{i\cdot\varphi_1} + \tau_1\kappa_2 e^{i\varphi_2}) \\ i\cdot(\kappa_1\tau_2 e^{i\cdot\varphi_1} + \tau_1\kappa_2 e^{i\varphi_2}) & -\kappa_1\kappa_2 e^{i\cdot\varphi_1} + \tau_1\tau_2 e^{i\cdot\varphi_2} \end{pmatrix} \begin{pmatrix} E_{i1} \\ E_{i2} \end{pmatrix} \tag{1.68}$$

For the case where $\tau_1 = \tau_2 = \tau$ and $\kappa_1 = \kappa_2 = \kappa$, we obtain:

$$\begin{pmatrix} E_{o1} \\ E_{o2} \end{pmatrix} = e^{i\left(\frac{\varphi_1+\varphi_2}{2}\right)} \begin{pmatrix} \tau_{eff} & i\cdot\kappa_{eff} \\ i\cdot\kappa_{eff} & \overline{\tau_{eff}} \end{pmatrix} \begin{pmatrix} E_{i1} \\ E_{i2} \end{pmatrix} \tag{1.69}$$

Where

$$\kappa_{eff} = 2\kappa\tau\cos\left(\frac{\Delta\varphi}{2}\right) \quad \text{and} \quad \tau_{eff} = 2\tau^2\cos\left(\frac{\Delta\varphi}{2}\right) - e^{-i\frac{\Delta\varphi}{2}} \tag{1.70}$$

and

$$\Delta\varphi = \varphi_1 - \varphi_2 \tag{1.71}$$

Figure 1.9 shows the transmission τ_{eff} (red) and coupling κ_{eff} (blue) terms of the transfer matrix of an MZI made of 50/50 couplers as the phase difference $\Delta\varphi$ is changed.

1.5.3 MMI

A Multi-Mode Interference (MMI) device is a large optical waveguide supporting many modes, which splits the input of a single input waveguide into many

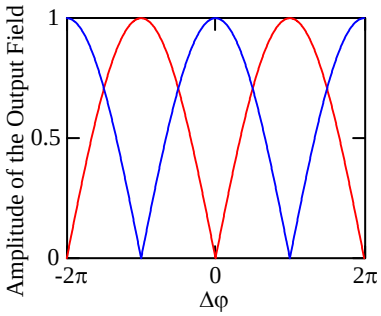

Figure 1.9: Transfer function of a 50/50 MZI. In red we have the transmission τ_{eff} and in blue we have the coupling κ_{eff} coefficients.

output waveguides. The mode at the input excites the other modes of the multi-mode structure. Since each mode propagates with its own propagation constant, an interference pattern arises, having different number of transversal lobes showing up as the modes propagate. This allows to split the input signal in two or more outputs, as depicted in Fig. 1.10. The propagation constant for each mode can be obtained through effective index method, and the coefficients for the amplitude of each mode is obtained by inner product of the modes with the input mode [20, 25]. The best way to obtain the right dimensions and length of the MMI is through plotting the propagation of the excited modes. Some approximations to obtain the proper dimensions of the MMI for a given number of outputs can be used [25, 26].

MMI is used in this work as a mode converter and a filter. It converts the mode of a single-mode waveguide into the symmetric mode of a waveguide composed of two parallel silicon beams surrounded by silicon dioxide, as schematically shown if Fig. 1.10. It works as a filter when we reverse the propagation direction, since a symmetric mode is converted back to the mode of the output waveguide while an anti-symmetric mode is not converted to the mode of the input waveguide, being irradiated away, as shown in Fig. 1.11.

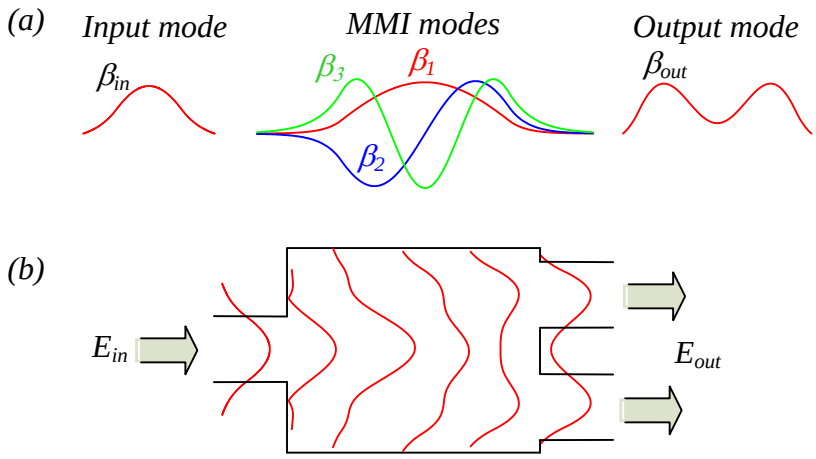

Figure 1.10: (a) Input mode, modes suported by the MMI and output mode with its correspondent propagation constants. (b) Field propagation through an 1×2-MMI.

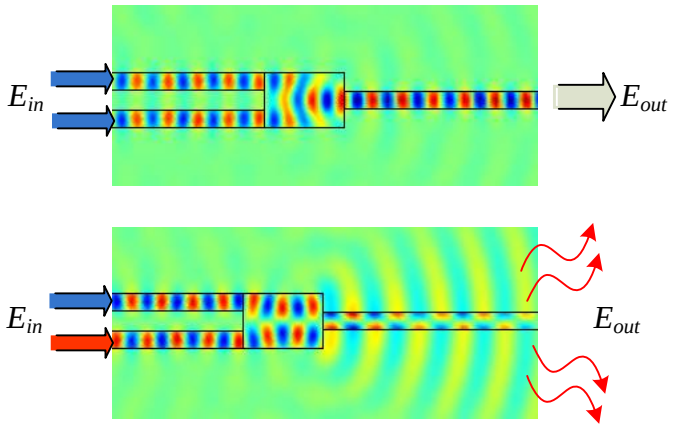

Figure 1.11: On the top we have an FEM simulation of a symmetric mode being converted to the mode of the output waveguide. On the bottom we have an FEM simulation of an anti-symmetric mode being irradiated at the input waveguide.

CHAPTER 2

HITLESS SWITCH

2.1 Introduction

Optical switches are critical elements for on-chip optical networks. They are essential for high performance interconnects in a multi-core microprocessor system [27, 28], where large bandwidth densities, low energy consumption and small footprint components are required [3, 29]. Here we demonstrate hitless operation of a broadband compact electro-optic switch for on-chip optical networks on a silicon platform. A broadband switch is important for two main reasons: low distortion of high bandwidth signals [30], and robustness from on chip temperature changes [31]. Hitless tuning, i.e. switching data at one wavelength without affecting the other wavelengths on the interconnect (see Fig. 2.1), is also an important criterion in on-chip optical networks employing multiple wavelengths [27]. A broadband hitless switch provides the ability to enable and disable a WDM channel drop filter without blocking an adjacent channel in the network.

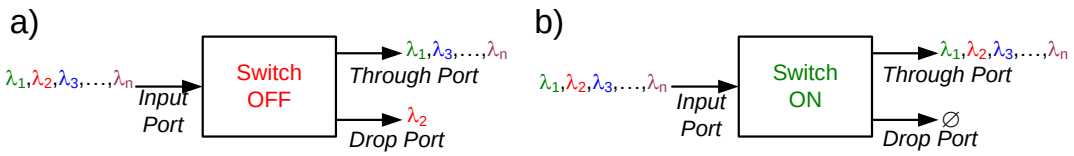

Figure 2.1: Hitless switch scheme. (a) When the switch is OFF, a single wavelength channel in a WDM system is directed to the drop port. (b) When the switch is ON, no channel is dropped.

Previously, thermo-optic [32, 33, 34] and all-optical [35] approaches have

been used to demonstrate broadband hitless switching using coupled resonators, and also proposed to be used in a Mach-Zehnder topology [36, 37]. Electro-optic broadband switching has also been demonstrated, however not in a hitless configuration [12, 38]. Here, we show the synthesis procedure, implementation and analysis of a broadband, hitless, compact electro-optic switch on a silicon photonics platform, using a compact broadband filter integrated with PIN diodes [39].

2.2 Switch Description and Synthesis

The device analyzed and fabricated consists of two coupled optical cavities surrounded by p-doped and n-doped regions. The two cavities create a broadband transmission while the integrated PIN diodes enable free-carrier injection and extraction to change the refractive index of silicon [39]. A schematic of the device with its transfer function for distinct detuning values is shown in Fig. 2.2.

The broadband operation of the device is achieved when a) the cavities share the same resonance wavelength and b) the coupling between each cavity and its adjacent waveguide is much stronger than the coupling between cavities. The hitless operation of the switch is achieved by changing the resonance of the cavity coupled to the drop waveguide while leaving the other unperturbed. When both cavities share the same resonance, light with frequency within the filter bandwidth is directed to the drop port. When the index of the cavity coupled to the drop port (right cavity in Fig. 2.2) is changed, the cavities no longer share the same resonances. This leads to an over-coupled system and the signal is routed to the through port. The fact that the index of the cavity coupled to the

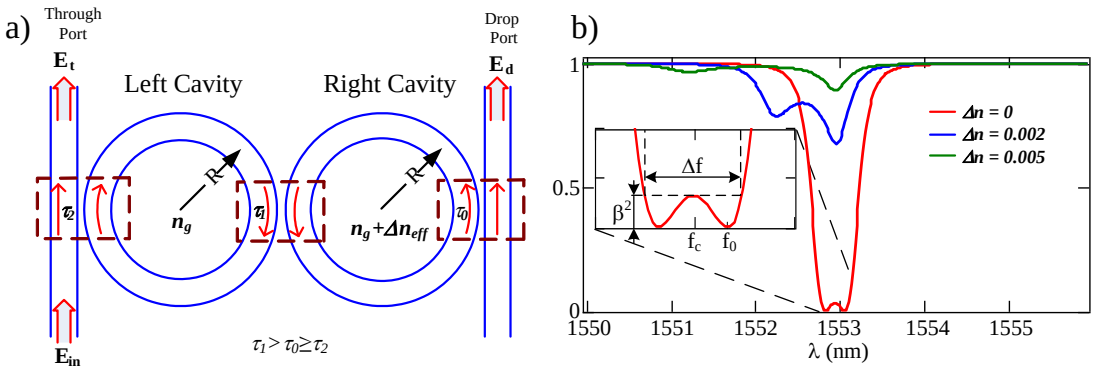

Figure 2.2: (a) Schematic of two coupled ring resonators with (b) its theoretical through port transmission spectrum. Red line shows the original transmission where the two cavities share the same resonance. The blue line shows a transient state and green line the final state of the switch, where detuning was provided by changing the refractive index of the right cavity.

through port (left cavity in Fig. 2.2) is not changed prevents perturbing adjacent channels, which is the goal of a hitless device. In principle, even the residual dispersion caused by the presence of the over-coupled cavity can be reduced by slightly detuning it to the edge of the WDM channel, or to a nearby region between two WDM communication channels.

The detuning mechanism used for changing the refractive index plays an important role for the possible applications of the device. Changing the refractive index by free-carrier plasma dispersion is crucial for systems which require fast switching transitions (a few nanoseconds) of small data packets (sub-microsecond or a few microseconds, depending on the amount of detuning provided, as shown on section 3), once thermo-optical effect caused by the current flowing through the device heats it up and reduces the index change provided by the free-carrier plasma dispersion. Thermo-optical detuning, as has been shown in [32, 33, 34], is suitable for slower switching times, hundreds

of nanoseconds at best [40], with unlimited holding time.

In order to optimize the device performance we calculate the coupling conditions, i.e., the transmission values for each directional coupler present in the device (τ_0, τ_1 and τ_2 in Fig. 2.2(a)) as a function of the desired bandwidth (Δf) given a desired intensity attenuation coefficient β^2, also known as power ripple, shown in the inset of Fig. 2.2(b). General methods for filter synthesis when there is no propagation loss has been extensively studied for CROW systems [41, 42, 43]. Here we provide the steps for a Chebyshev-like transfer function implementation when losses are considered in a two ring device, by forcing the minimum transmission to be zero and the maximum to be β^2 inside the bandwidth of the transmission spectrum of the through port.

The equations for the field at the through and drop ports are:

$$E_t = \frac{\tau_2 - e^{\imath\phi_2} a_2 E_{t1}}{1 - \tau_2 e^{\imath\phi_2} a_2 E_{t1}} \qquad \text{and} \qquad E_d = \frac{\sqrt{e^{\imath\phi_2} a_2} \cdot (-\imath\kappa_2) \cdot E_{d1}}{1 - \tau_2 e^{\imath\phi_2} a_2 \cdot E_{t1}} \tag{2.1}$$

with [44]

$$E_{t1} = \frac{\tau_1 - e^{\imath\phi_1} a_1 \tau_0}{1 - \tau_1 e^{\imath\phi_1} a_1 \tau_0} \qquad \text{and} \qquad E_{d1} = \frac{-\sqrt{e^{\imath\phi_1} a_1} \cdot (-\imath\kappa_1) \cdot (-\imath\kappa_0)}{1 - \tau_1 e^{\imath\phi_1} a_1 \tau_0} \tag{2.2}$$

and with

$$a_i = e^{-\frac{\alpha + \Delta\alpha_i}{2} \cdot 2\pi R} \qquad \text{and} \qquad \phi_i = \frac{2\pi}{\lambda} \cdot \left(n_g + \Delta n_{eff_i}\right) \cdot 2\pi R \tag{2.3}$$

where E_t is the field intensity at through port, E_d is the field intensity at drop port, τ_0, τ_1 and τ_2 are the transmission coefficients of the directional couplers shown in Fig. 2.2(c), κ_0, κ_1 and κ_2 are the coupling coefficients of the directional couplers, R is the radius of the rings, a is intrinsic loss, $\Delta\alpha_i$ is the loss caused by free-carrier absorption, α_i is the roundtrip attenuation coefficient for ring i,

n_g is the group index of the device, Δn_{effi} is the refractive index change caused by free-carrier plasma dispersion for ring i, and λ is the free space wavelength. With no free-carrier injection the values for roundtrip attenuation coefficient are equal $a_1 = a_2 = a$ and phases are also equal $\phi_1 = \phi_2 = \phi$. The equations are shown in a recursive fashion and can be easily extended for higher order filters, although a matrix analysis method can also be used [45]. Analogous to the condition for critical coupling in a single ring [44], critical coupling for two rings requires that the transmission in the input waveguide is equal to the product of attenuation coefficients and transmission coefficient of the output waveguide:

$$\tau_2 = a^2 \tau_0 \tag{2.4}$$

Plugging Eq. 2.4 into the equation for the transmission field E_t and forcing it to have zeros in the numerator we obtain:

$$\tau_1 = \cos\phi_0 \frac{2a \cdot \tau_0}{1 + {\tau_0}^2 a^2} \tag{2.5}$$

where ϕ_0 is the value of the phase ϕ that provides zeros in the through port transmission spectrum. Plugging Eq. 2.4 and Eq. 2.5 in Eq. 2.1 and considering that the minimum attenuation allowed inside the bandwidth (β) happens for $\phi = 0$, the following equation is obtained for τ_0:

$$(a \cdot \tau_0)^4 - 2\frac{1 - \cos\phi_0}{\beta \cdot a}(a \cdot \tau_0)^3 - \frac{(a^2+1)\,(2 \cdot \cos\phi_0 - 1)}{a^2}(a \cdot \tau_0)^2 - 2\frac{(1 - \cos\phi_0)}{\beta \cdot a}(a \cdot \tau_0) + \frac{1}{a^2} = 0 \tag{2.6}$$

which can be solved analytically or numerically. The root we are looking for is the one with real value which provides $\tau_0 < 1$. Finally, the phase of the transmission zero can be related to bandwidth by:

$$\phi_0 = \frac{2\pi}{2\sqrt{2}} \cdot \frac{{\lambda_c}^2}{c_0} \frac{\Delta f}{FSR} \qquad \text{or} \qquad \phi_0 = \frac{2\pi}{2\sqrt{2}} \cdot \frac{\Delta f}{fsr} \tag{2.7}$$

where λ_c is the central wavelength of the switch, Δf is the bandwidth or flat region where the through port transmission is smaller than the ripple (β), c_0 is the light speed at vacuum, FSR is the Free Spectral Range in wavelength domain and fsr is the Free Spectral Range in frequency domain. Therefore, once the values of Δf, β and a are specified, one can determine the transmission for each directional coupler present in the device. It can be demonstrated from the equations above that, for devices with losses, one can have a box-like transfer function only if the value of ϕ_0 is greater than a minimum value ϕ_{min}:

$$\phi_{\min} = \frac{2 \cdot (a^4 + a^2) - \beta \cdot (a^6 + a^4 + a^2 + 1)}{2 \cdot (1 - \beta) \cdot (a^4 + a^2)} \tag{2.8}$$

2.3 Fabrication, experimental description and results

The process flow of the structure ensures that the diodes are electrically isolated for independent tuning of each cavity, an important requirement to achieve hitless operation. We fabricate the device on a silicon-on-insulator (SOI) substrate with a 250 nm device layer on a 3 μm buried oxide layer. Waveguides and cavities are created by patterning and etching 210 nm of the 250 nm top silicon layer, leaving a 40 nm slab throughout the chip. The diodes are made by doping the slab regions around each cavity. We achieve electrical isolation by etching the silicon slab in undoped regions including between the cavities. The hard mask used for patterning the waveguides and cavities protects them in this etching step, while additional patterned HSQ resist is used as a mask for the remaining slab regions. Although only one of the cavities requires dynamic tuning, we create electrical contacts to both cavities in order to fine tune the device spectra if needed. Restricting a slab to the cavity region improves both optical cou-

pling at the tapered chip input and propagation losses through the waveguide. The quasi-TM propagation mode is chosen for this study because it has lower dependence on sidewall roughness as compared to the quasi-TE mode, usually providing a cleaner spectrum. The shape of the device was designed to be equivalent to a racetrack in the region where a strong coupling is required and equivalent to a ring in the coupling region where the coupling is weak, therefore allowing waveguides to be placed further apart and reducing mode conversion losses [46]. For a device with power ripple of 17.5 dB below the transmission, bandwidth of 60 GHz and losses about 10 dB/cm we obtain coupling parameters $\tau_0 = 0.811$, $\tau_1 = 0.970$ and $\tau_2 = 0.800$ which were achieved using spacings of 304 nm, 350 nm and 300 nm, and linear region lengths of 3797 nm, 673 nm and 3797 nm, respectively. The fabrication of the PIN structure is performed by implanting BF^{2+} and As^{-} as acceptor and donor dopants, respectively, with a $10^{19}\,cm^{-3}$ concentration for both [11]. Nickel silicide is formed for contacting the doped regions, and aluminum is used for the contact pads. A Scanning Electron Microscope picture of the cavities with doped Silicon slab surrounding them is shown in Fig. 2.3(a), an Optical Microscope picture of the device before evaporating the Aluminum pads is shown in Fig. 2.3(b). The measured spectrum of the device fabricated is shown in Fig. 2.3(c). Broadband hitless switching behavior is demonstrated by measuring the dynamics of the spectrum as the switch is turned ON and OFF. We monitor the output power at the through and drop ports during both carrier injection and extraction on an oscilloscope with a 30 GHz bandwidth optical sampling module. We scan the input laser from 1547.3 nm to 1554.3 nm with steps of 0.05 nm and observe the spectrum dynamics shown in Fig. 2.4. The switching times of the device, free-carrier concentration and amount of refractive index change are obtained by fitting the measured

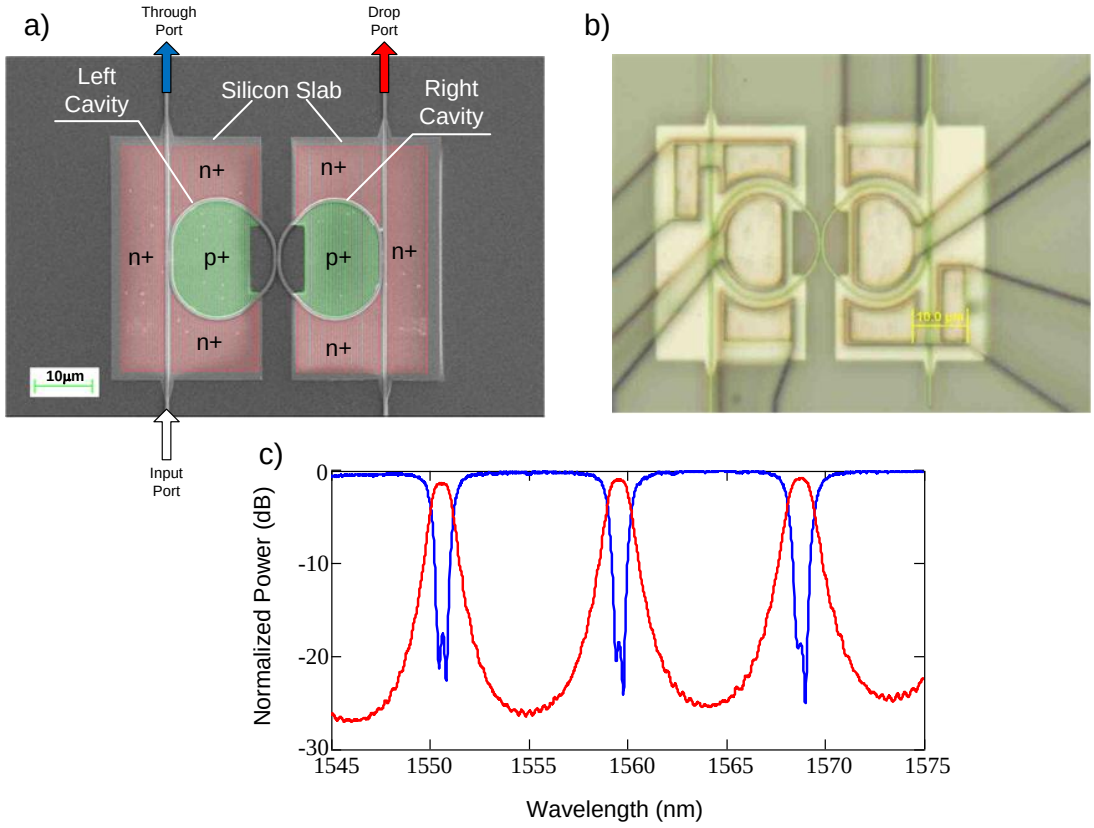

Figure 2.3: (a) SEM picture of the device with the p^+ (green) and n^+ (red) implanted areas highlighted. The Si waveguides have 250 nm $\times$ 450 nm cross-section. The device is clad with 1 µm of silicon dioxide and has a 3 µm silicon dioxide BOX. Each cavity has a total length $2\pi \times 10$ µm with 8 µm bend radius. (b) Optical microscope picture of the device before evaporating aluminum for contact pads. (c) Spectrum of the device fabricated without any carrier injection.

data to the theoretical model. We simulate the device behavior by plugging the refractive index change and losses in the transfer function equations of the device (Eqs. 2.1 to 2.3). In order to obtain the relation between refractive index change and current applied, a DC experiment is performed to separate the blue shift in the resonance, given by free-carrier concentration [47], from the slow red shift provided by thermal effect [48, 49]. The influence of the temperature and

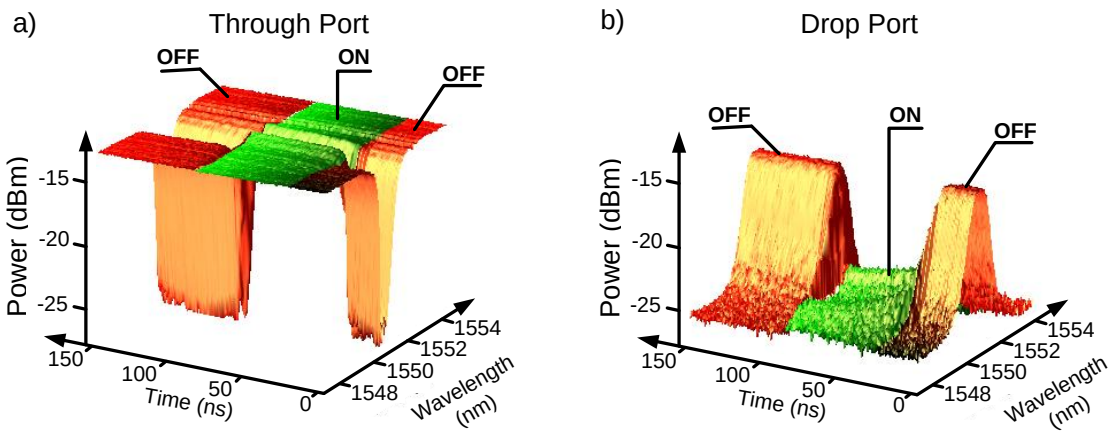

Figure 2.4: (a) Dynamics of the spectrum for the through port. Switch starts in OFF state (red), it is turned ON at 15 ns (green) and is turned OFF again at 110 ns (red). (b) Dynamics of the spectrum for the drop port. Notice that the box-like spectrum disappears in the period where the switch is kept ON.

carrier concentration on the device performance are distinguishable: when a DC bias is applied, the carrier concentration can be approximated as directly proportional to the current while the device temperature can be approximated as proportional to the power dissipated (or the current squared). Mathematically we have:

$$\Delta n_{eff} = -c_1 I + c_2 I^2 \tag{2.9}$$

where Δn_{eff} is the change in effective refractive index, and c_1 and c_2 are proportionality constants. In order to measure the resonance shift carefully, we apply a DC voltage to the cavity coupled to the input waveguide and measure both the maximum resonance shift ($\Delta\lambda_{DCmax}$) and the current that provides this shift (I_{DCmax}). Using the relationship, Eq. 2.9 becomes:

$$\Delta n_{eff} = -\left[\frac{2n_g}{\lambda}\right] \cdot \left[\frac{\Delta\lambda_{DC\,\max}}{I_{\max}}\right] I + \left[\frac{n_g}{\lambda}\right] \cdot \left[\frac{\Delta\lambda_{DC\,\max}}{I^2_{\max}}\right] I^2 \tag{2.10}$$

where n_g is the group index and λ is the original resonance wavelength. Eq. 2.10 provides a direct relation between index change and current flowing through

the device, from which we obtain the free-carrier concentration as a function of the current. This procedure allows us to identify the term with I_2 dependence and suppress it from the model simulated for device operation much faster than the time constants of the thermal effect. We extract the free-carrier concentration inside the device from the free-carrier concentration index change (Δn_{Si}) and free-carrier absorption losses ($\Delta\alpha$) dependence of silicon, given by [8, 50, 47]:

$$\Delta n_{Si} = -8.8 \times 10^{-22} N - 8.5 \times 10^{-18} P^{0.8}, [N] = [P] = cm^{-3} \tag{2.11}$$

$$\Delta\alpha = 8.5 \times 10^{-18} N + 6.0 \times 10^{-18} P, [\Delta\alpha] = cm^{-1} \tag{2.12}$$

where Δn_{Si} is the index change of the silicon waveguide for a given concentration of electrons (N) and holes (P). The index change in the silicon is related to the overall index change, by the confinement factor (Γ) of the field, which in our case is $\Gamma = 0.81$ [51]. Once Δn_{Si} is known and $N = P$ in the steady state, we obtain the free-carrier concentration as a function of the current. The losses added to the right cavity ($\Delta\alpha$) are obtained from the Eq. 2.12, which closes the set of variables used in the modeling. In Figs. 2.5 and 2.6 we show simulated (continuous lines) and measured (dotted lines) spectrum (Fig. 2.5) and time response (Fig. 2.6) for the through (blue) and drop (red) ports. The drop port transmission changes by 9.8 dB when the switch is turned ON with a 1.46 V bias and 4.0 V_{pp} switching signal. The through port transmission has an ON/OFF ratio of 16.6 dB. When the device is ON, the right cavity has a 2.8 nm resonance shift meaning an index change $\Delta n_{eff} = 0.009$ and a free-carrier density around $3.6 \times 10^{18}\, cm^{-3}$. The contact resistance of the device is $R_S = 437\,\Omega$ and the power consumed in ON state, considering a 0.7 V junction potential, is 17.4 mW. The time domain signal for a single wavelength at 1550.8 nm is shown in Fig. 2.6(a). In Fig. 2.6(b) we show the result of switching a 1 Gbps modulated signal with central wavelength 1550.8 nm. Fig. 2.7(a) shows the eye diagram of a 10 Gbps

signal input. Fig. 2.7(b) shows the same signal at the drop port. We notice that the 60 GHz bandwidth accommodates the 10 Gbps signal with low distortion. By fitting the simulated curve to the experimental results when a DC voltage is applied we estimate $\Delta\lambda_{DCmax} = 0.8$ nm with $I_{DCmax} = 2.0$ mA. Plugging these values in Eq. 2.10 and considering that the thermal effect is negligible for the dynamics of the system we obtain, for a e^{-1} amplitude decay, the time constants for the switch as 7 ns for OFF-ON transition and 3 ns for ON-OFF transition.

We demonstrate, as can be seen in 2.7, that at least an 80 ns window can be

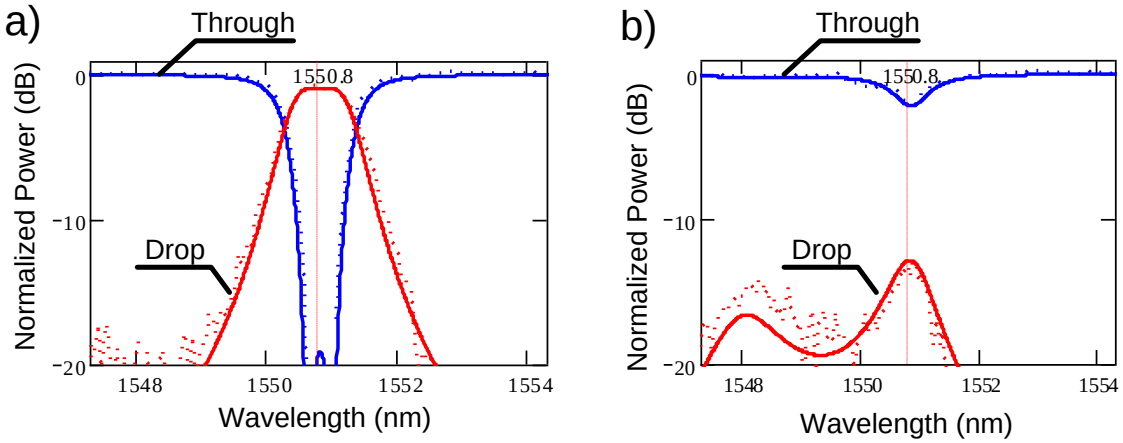

Figure 2.5: (a) Instantaneous spectrum for the switch off at 10 ns. (b) Instantaneous spectrum for the switch on at 107.5 ns. Dotted lines represent experimental data while continuous lines are the calculated values.

sustained with the switch ON with a 7 ns transient time. For a 10 Gbps signal going through the device it represents switching of up to 710 bits. Note that the holding time and current applied (i.e. the extinction ratio) are not independent, being necessary to reduce the current when longer holding times are required. In fact we are able to hold the device for more than 1 µs for extinction ratios 4 dB smaller than the values shown in Fig. 2.5. Longer hold times, essential for on-chip networks, can be achieved using novel electro-optic structures [39], or

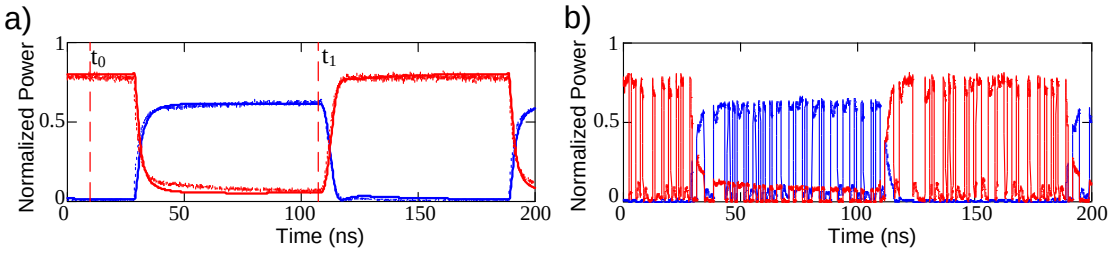

Figure 2.6: (a) Time domain response for a single 1550.8 nm wavelength as input. Experimental result is shown in dotted lines, while result from fitting is shown in continuous line; (b) time domain for a 1 GHz modulated signal as input.

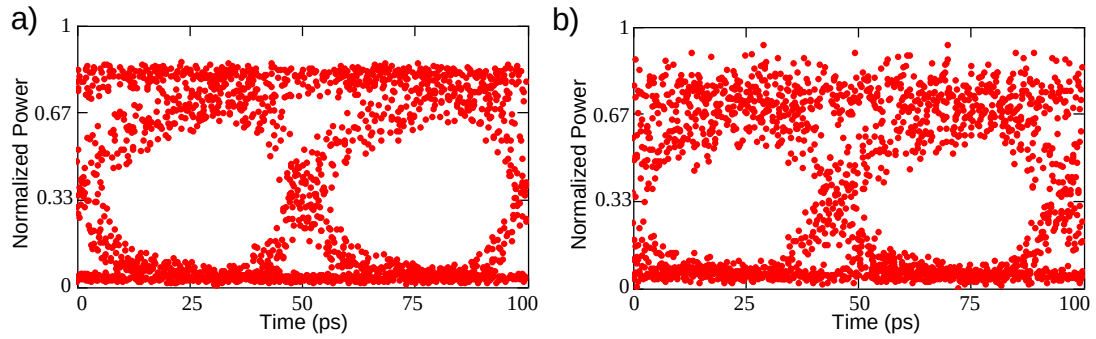

Figure 2.7: Eye diagram of a 10 Gbps signal (a) at input and (b) at drop port.

reducing the surface recombination rates [52].

2.4 Operational Limits

The extinction ratio experienced by each port when the switch goes from OFF state to ON state is limited by the maximum current that the diode can tolerate. Destructive experiments with the fabricated diodes shows that DC currents around 7 mA can damage them, limiting the detuning we can provide for the

switch. For a resonant cavity, the maximum optical detuning needed for maximum extinction ratio is

$$\Delta n_{MAX} = \frac{\lambda}{4\pi R} \tag{2.13}$$

For this amount of refractive index change, the detuned cavity needs to have its resonance shifted by half FSR of the device, which corresponds to 4.5 nm for the switch demonstrated here. To avoid damaging the device, we limit the current to 6.3 mA and obtain at most a 2.8 nm detuning. Even though 2.8 nm detuning is only 62% of the maximum detuning, its effect in the ON/OFF ratio is much stronger: for the drop port, the 9.8 dB ON/OFF ratio obtained experimentally represents 79% of the theoretical value for maximum detuning; for the through port, the 16.6 dB ON/OFF ratio obtained experimentally represents 98% of the theoretical value for the maximum detuning. Both values agree with the theoretical result for a 2.8 nm detuning, which also shows that reasonable ON/OFF ratios can be obtained much before the maximum detuning is achieved.

Noticing that the ON/OFF ratio for the through port easily achieves a value close to its maximum while the drop port ON/OFF ratio increase slowly with the detuning experienced by the switch, a helpful project chart is obtained by verifying the detuning required to achieve equal ON/OFF ratio for both through and drop ports. The values of the ON/OFF ratio when they are equal for both ports are shown as a function of the synthesis parameters in Fig. 2.8(a), and the detuning related to it is presented in Fig. 2.8(b). The detuning is normalized by the maximum detuning presented in Eq. 2.13 and results are plotted for 4 different power ripple specifications, in dB, where $\xi = -20.log(\beta)$. We consider a lossless cavity, with $a = 1$ (0 dB/cm), and a lossy cavity, with $a = 0.9964$ (10 dB/cm for a 5 μm ring radius or 5 dB/cm for a 10 μm ring radius), which is a reasonable value for passive devices we fabricated beforehand for characteri-

zation of the filters. The relation between bandwidth and the synthesis parameter ϕ_0 are explicitly shown for 5 µm and 10 µm ring radius with effective index $n = 1.9$ and group index $n_g = 4.35$, as can be seen in the auxiliary horizontal axes added in red to Fig. 2.8(a). The relation between detuning and carrier density is also explicitly shown in the red auxiliary vertical axes for 5 µm and 10 µm ring radius. For the device fabricated, we verify from Fig. 2.5(a) that its ripple is close to 17.5 dB, with a flat bandwidth about 60 GHz ($\phi_0 = 0.12$). Using these values in Fig. 2.8(b) we verify that the drop port ON/OFF ratio cannot reach the same value as the through port ON/OFF ratio for the device fabricated.

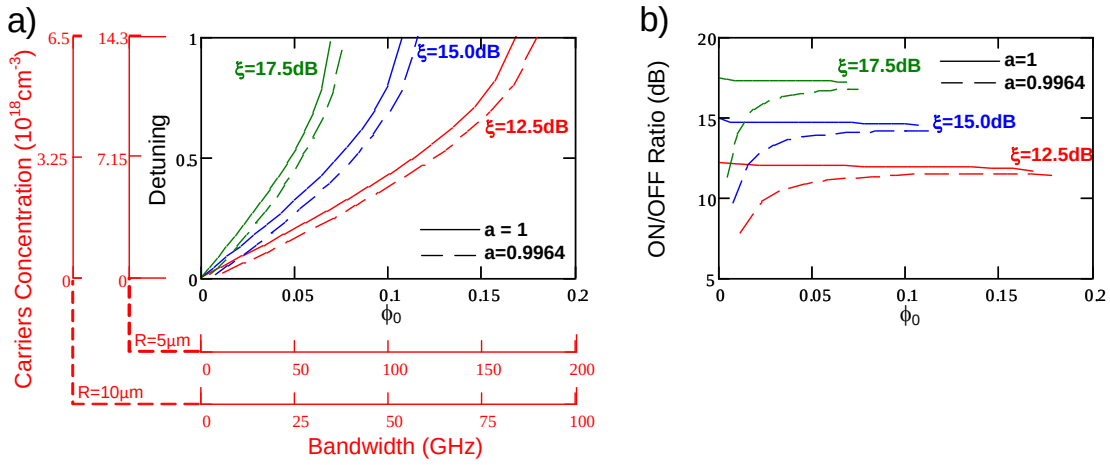

Figure 2.8: (a)Detuning (or Carrier Concentration, in red) required to the same ON/OFF ratio for through and drop ports. It is shown as a function of the normalized transmission zero (Bandwidth) for a few ripple (ξ) and roundtrip loss (a) specifications. (b) Value of the ON/OFF ratio when they are the same for through and drop port.

The intrinsic insertion loss for this switch topology has to be considered for through and drop port in three main points: the central wavelength in the drop port when the switch is OFF, the central wavelength in the through port when the switch is ON and the detuned wavelength in the through port when the

switch is ON. They are pointed out in Fig. 2.9(a) as b), c) and d), and, for the device fabricated, we obtained 0.5 dB, 2.0 dB and 0.4 dB, respectively. In general, each insertion loss can be obtained as a function of the synthesis parameters (bandwidth and ripple), and are depicted in Figs. 2.9(b), (c) and (d) for both a lossless and a lossy case. In Fig. 2.9(b) we verify that the insertion loss of the drop port when the switch is OFF increases considerably for very small bandwidths in a lossy device, once there is a minimum bandwidth that provides the resonance splitting as predicted by Eq. 2.8. Below that bandwidth the field at the drop does not have a box-like shape anymore. In Fig. 2.9(c) we notice that the insertion loss can change from values comparable to those obtained for the drop port in the lossless case to values with a higher loss when propagation losses are added. In Fig. 2.9(d), we show the insertion loss at the detuned resonance with a different vertical scale once its values are much smaller than the other cases. We consider in Fig. 2.9(c) and (d), when the switch is ON, the detuning required to have both through and drop port with the same ON/OFF ratio. Besides the limits shown in Fig. 2.9, the insertion losses when the switch is ON can be reduced by applying a small detuning in the cavity coupled to the input waveguide, so that the overcoupled resonance is shifted to the nearby region where the crosstalk specifications do not allow data to be allocated.

2.5 Conclusion

We show the characteristics of a broadband (60 GHz), spectrally hitless, compact (20 μm × 40 μm), fast (7 ns) electro-optical switch. The device, composed of two coupled resonant cavities, has independently addressable PIN diodes, and the hitless behavior happens when only the cavity connected to the output

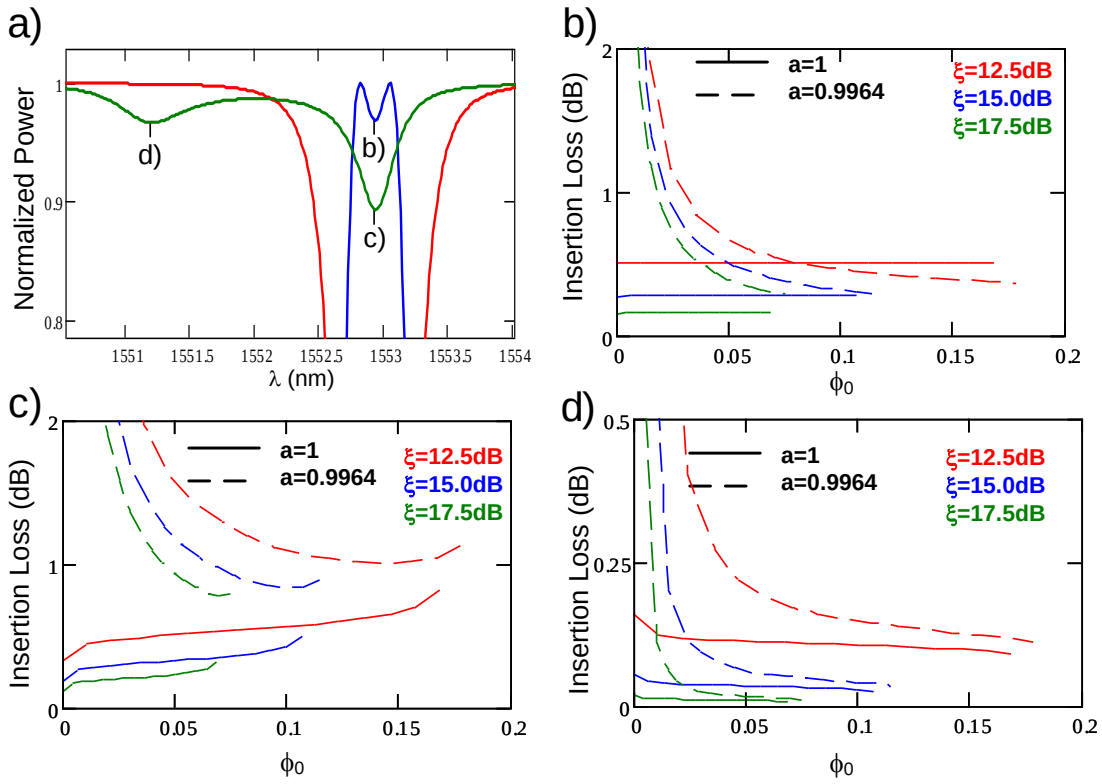

Figure 2.9: Insertion losses of the switch as a function of the normalized bandwidth (ϕ_0) for a few ripple (ξ) and roundtrip loss (a) specifications. (a) Spectrum showing the insertion losses analyzed. (b) Drop port insertion loss when the switch is OFF. (c) Through port insertion loss at the central wavelength when the switch is ON. (d) Through port insertion loss at the detuned wavelength when the switch is ON.

waveguide is detuned by free-carrier injection. Thermal effects in the device limit the hold time to about 80 ns, and the device fabricated shows an ON/OFF extinction ratio of 9.8 dB for the drop port and 16.6 dB for the through port when driven by a 1.46 V bias and 4.0 Vpp switching signal, with total power consumption of 17.4 mW. This demonstrated device is a critical component for on-chip networks.

CHAPTER 3

HIGH FIDELITY TUNING OF SECOND-ORDER MICRORING RESONATOR FILTER OVER LARGE SPECTRAL RANGE

3.1 Introduction

Wavelength Division Multiplexers (WDM) are essential components in high bandwidth telecom and datacom [53]. Their most important feature is the capability to drop a signal from the network based on the carrier wavelength, as well as to add a new signal to the network, as depicted on Fig. 3.1. Current WDM filters only exhibit high performance (i.e., high extinction ratio and low cross talk) for a limited band (typically 1 nm). Although some WDM filters can be tunable, most either rely on bulk components that are not integrable [54, 55] or on movable parts, (such as MEMS-based filters [54]) and are not robust to the environment.

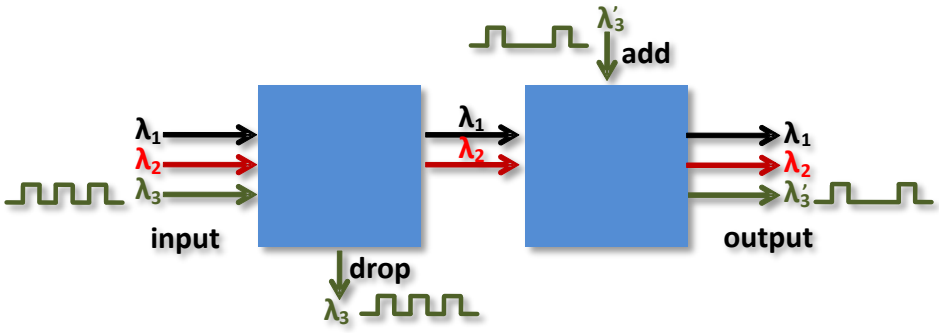

Figure 3.1: Functional schematics of WDM filters. While one of them drops the signal with carrier wavelength at λ_3 from the network, another one adds a different signal at the same wavelength, allowing maximum use of the bandwidth of the network.

The main challenge in tunable WDM filters is maintaining the spectra char-

acteristics (such as bandwidth and extinction ratio) while tuning over large spectral range. This is because high performance WDM filters are typically obtained by using high-order filters such as a series of coupled-resonator optical waveguides (CROW) [19, 32, 45, 55], or in a Fabry-Perot topology [56] which degrade in performance when they are reallocated over a large spectral range. The degradation occurs because tuning the resonators not only modifies their resonance wavelength but can also change the coupling between cavities. We can see the effects of such changes shown in Fig. 3.2. The continuous lines show simulations of the original spectrum of a second-order filter, while the dotted lines show simulations of possible outcomes for the spectrum after thermal tuning the resonance far away, depending on the heat distribution across the filter.

Here we model and demonstrate a thermally tunable WDM filter based on a Si/SiO_2 coupled resonator filter that maintains high performance over at least 15 nm tuning range. We first model the behavior of important characteristics involving the coupling region during thermal tuning. Then, we verify how the coupling changes in two scenarios: first, when the coupling region is at a temperature different of the average temperature of the resonator. Second, when not just the temperature at the coupling region is different from the average, but also is different on each waveguide of the coupling region. Based on the modeling, a set of 6 different configurations of heaters is fabricated to verify the distinct behavior predicted. Finally, we observe a large reallocation without degrading bandwidth or extinction ratio of the filter.

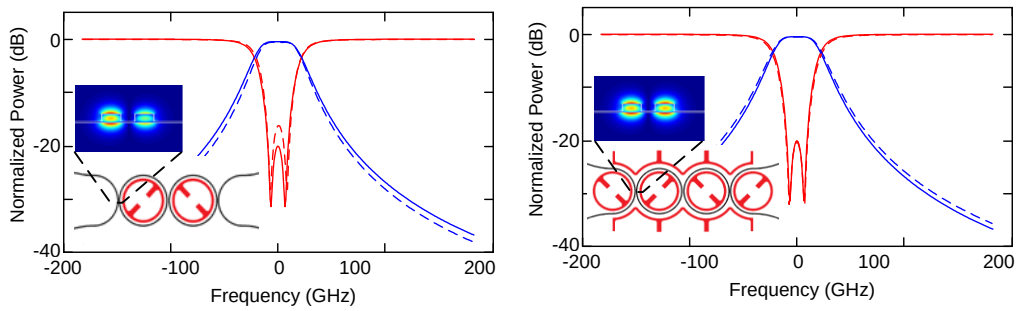

Figure 3.2: Typical transfer function of a WDM filter. Through (red) and drop (blue) ports are shown for the original resonance (continuous lines) and for the resonance placed about 30 nm by thermal tuning. An schematic of the filter, in black, sorrounded by heaters, in red, for the two cases exemplified at left and right. The electrical field distribution, considering the difference in index given by different thermal distribution is also shown in the inset.

3.2 Thermal dependence of the coupling

We model the coupling between two adjacent waveguides taking into account its dependency on three factors [22]: (1) the optical length of the coupling region (z_c); (2) the overlap of the evanescent field of one waveguide with the fundamental mode of the other (K_c); (3) the difference between the propagation constant of the individual waveguides (Δ). All of them depend implicitly on wavelength and temperature, therefore thermally tuning the rings affect all of these factors.

Coupled-Mode Theory, when considering the general case of asymmetric waveguides, provides the value for the coupling κ and transmission τ in a parallel-waveguides configuration according to the expressions [22]:

$$\kappa = -i \cdot e^{i \cdot \Delta \cdot z_c} (K_c/\beta_c) \sin(\beta_c z_c) \tag{3.1}$$

$$\tau = e^{-i \cdot \Delta \cdot z_c} \left[\cos(\beta_c z_c) + i(\Delta/\beta_c) \sin(\beta_c z_c)\right] \tag{3.2}$$

Where $\beta_c = \sqrt{K_c^2 + \Delta^2}$. For the case of geometrically symmetric coupling region, Δ is a function only of the temperature difference of the waveguides, and can be calculated in a first order approximation as

$$\Delta = \Gamma \frac{\pi}{\lambda_0} \frac{dn_{Si}}{dT} (T_{right} - T_{left}) \tag{3.3}$$

where λ_0 is the wavelength of the light, n_{Si} is the effective index of Si, T_{right} is the temperature of the right waveguide in the coupling region, T_{left} is the temperature of the left waveguide in the coupling region, Γ is the confinment factor [22, 51].

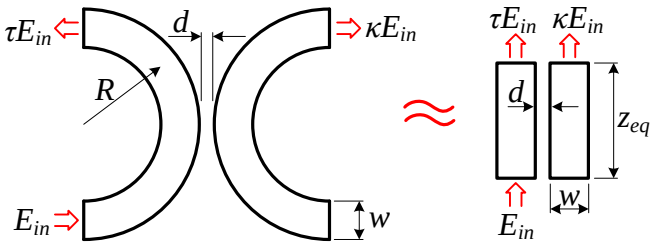

Figure 3.3: Equivalent parallel-waveguide model for the coupling of two curved waveguides.

The equations for a parallel-waveguides directional-coupler can be used for a curved coupler once the equivalent length is obtained, [24] as depicted in Fig. 3.3:

$$z_{eq} = \sqrt{\pi R / \gamma} \tag{3.4}$$

where R is the curvature radius and γ is the decay constant of the evanescent field, given by:

$$\gamma = \frac{2\pi}{\lambda} \sqrt{n_{eff}^2 - n_{SiO_2}^2} \quad , \tag{3.5}$$

where n_{eff} is the effective index of the waveguide and n_{SiO_2} is the refractive index of SiO_2.

A simplified model for calculating the coupling constant K_c is obtained for the 2D model of the 3D structure (as depicted in Fig. 1.2). Given that the field distribution for the fundamental mode of a slab waveguide it given by Eq. 1.16, we can calculate analytically the overlap integral, obtaining:

$$K_c = \frac{\varepsilon_0 \pi c_0}{2\lambda} C^2 \left(\frac{n_{slab}^2 - n_{SiO_2}^2}{n_{slab}^2 \cdot n_{SiO_2}^2} \right)^{\sigma} \frac{e^{-\gamma\left(d+\frac{w}{2}\right)}}{\cos\left(k_x \frac{w}{2}\right)} \times \frac{2k_x \cosh\left(\gamma\frac{w}{2}\right)\sin\left(k_x\frac{w}{2}\right) + \gamma \sinh\left(\gamma\frac{w}{2}\right)\cos\left(k_x\frac{w}{2}\right)}{k_x^2 + \gamma^2} \quad (3.6)$$

Where

$$k_x = \frac{2\pi}{\lambda}\sqrt{n_{slab}^2 - n_{eff}^2} \quad , \quad (3.7)$$

and C is the normalization factor given by Eq. 1.17.

With the equations for Δ (Eq. 3.3), z_{eq} (Eq. 3.4) and K_c (Eq. 3.6) at hand, we can model scenarios which explore different temperature-distribution dependence for the coupling. We have that the refractive indices of Si and SiO_2 depend on wavelength and temperature, where the wavelength dependency can be modeled using Sellmeier equations for Si and SiO_2 [20], using the coefficients present in Table 1.2 and the temperature dependency can be modeled as proportional to the thermo-optical coefficient for each material, being aproximately $1.84 \times 10^{-4} K^{-1}$ for silicon [15, 57], and $1.5 \times 10^{-5} K^{-1}$ for silicon dioxide [58].

3.3 Lumped Model for Temperature Dependence

The temperature distribution across a microring resonator is responsible for setting its resonance wavelength. A given resonance wavelength λ_{res} is obtained for a unique average temperature T_{ring} of a silicon microring resonator.

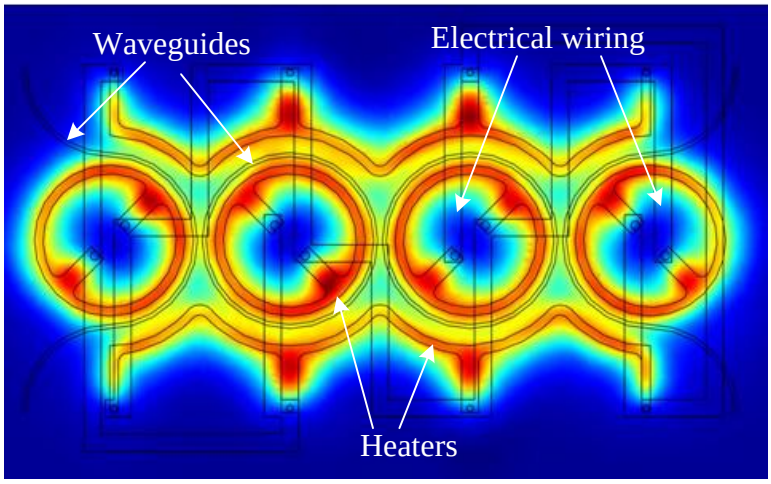

Figure 3.4: Example of full 3D heat distribution simulation. We observe that the vias act quite well as heat sinks, changing the temperature around them. We also notice that the temperature of the microring resonators varies as the geometry of the heaters varies.

We present a simple model to overcome the computationally demanding full 3D simulations for the heat distribution across the device. As heat comes from resistors surrounding the filters, a temperature distribution pattern is observed, as we can see in the FEM simulation shown in Fig. 3.4. The symmetry of the structure allows us to analyze a smaller section, composed of a ring and a coupling waveguide. We therefore separate the temperature of the device in three variables: the average temperature of the ring is lumped the variable T_{right}, the average temperature in coupling waveguide is lumped in the variable T_{left}, and average temperature of the whole ring is lumped in the variable T_{ring}.

Our goal is to engineer the temperature distribution across the device so that we can make the coupling κ_{new} at wavelength λ_{new} to be the same as the original coupling κ_{old} at wavelength λ_{old}, which ultimately makes it possible to have the same transfer function for the filter when tuned at any wavelength. Temperature tuning is a simple process: increasing the temperature of the microring

red-shifts its resonance, which means that the free-space wavelength needs to be increased to keep constant the propagation constant. On the other hand, the evanescent field present in the silicon dioxide is stronger for longer wavelengths, increasing the coupling between the microring and input waveguide. Since the resonance wavelength depends on the average temperature, we notice that the same resonance wavelength can be obtained for a lower coupling-region temperature if the rest of the microring is hotter, bringing up the possibility to tune the coupling by changing the temperature distribution.

Figure 3.5 shows how the coupling κ_{new} changes as the temperature of the coupling region of the microring T_{right} changes around the average temperature of the microring $T_{ring} = 650K$. It is calculated for two scenarios: first, when the temperature of the input waveguide is $T_{left} = T_{right}$; and second, when the input waveguide is kept at room temperature $T_{left} = 300K$. We use equations 3.1 through 3.7 to plot Fig. 3.5. We observe that for the case where both waveguides at the coupling region are kept at the same temperature ($T_{left} = T_{right}$), their temperature need to be closer to the average temperature of the ring $T_{ring} = 650K$ than the case when the waveguides at the coupling region are kept at different temperatures, with the left waveguide kept at room temperature ($T_{left} = 300K$). In both cases the temperatures T_{left} and T_{right} of the coupling region needs to be below the average temperature of the microring T_{ring} in order to achieve $\kappa_{new} = \kappa_{old}$ at the new wavelength. From these two cases, we have a range of possible solutions for T_{right} for the interval $300K < T_{left} < T_{right}$.

We design various heater configurations around the coupled cavities and compare the original spectrum with the shifted spectrum of each one of the configurations. FEM simulations, as shown in Fig. 3.6 and Fig. 3.7, provide two

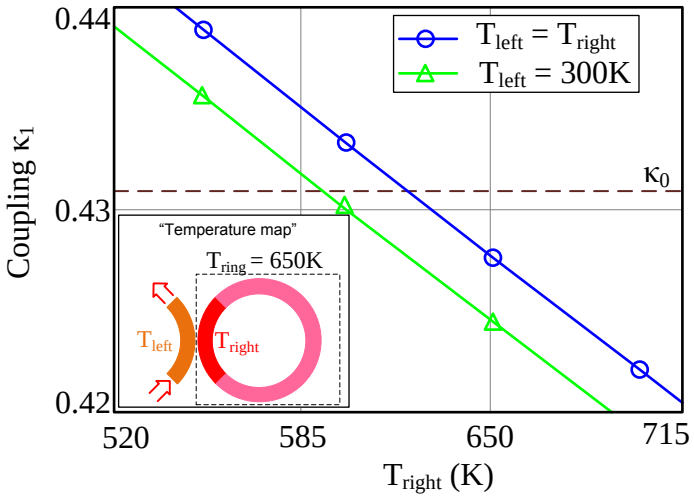

Figure 3.5: Example of coupling dependence on temperature variation of the coupling region. We have three distinct regions: the coupling waveguide (orange), the coupling region of the microring (red) and the delay part of the microring (rose). We change the temperature T_{right} around the temperature T_{ring} and observe the change in coupling for the case when $T_{left} = T_{right}$ (blue) and $T_{left} = 300K$ (green).

important insights for the design. First, we observe that having a thin 40 nm silicon slab connecting the heater to the silicon waveguides increases the efficiency the heat diffusion, as shown in Figs. 3.6 and 3.7. Second, comparing Figs. 3.6 and 3.7 we observe that the presence of the vias change considerably the heat distribution. Therefore, by just changing the placement of the vias in the structure we achieve different temperature distributions.

3.4 Fabrication and results

The device is fabricated on a Silicon-on-Insulator (SOI) wafer, using a CMOS compatible process. Silicon waveguides are etched with a 210 nm by 450 nm

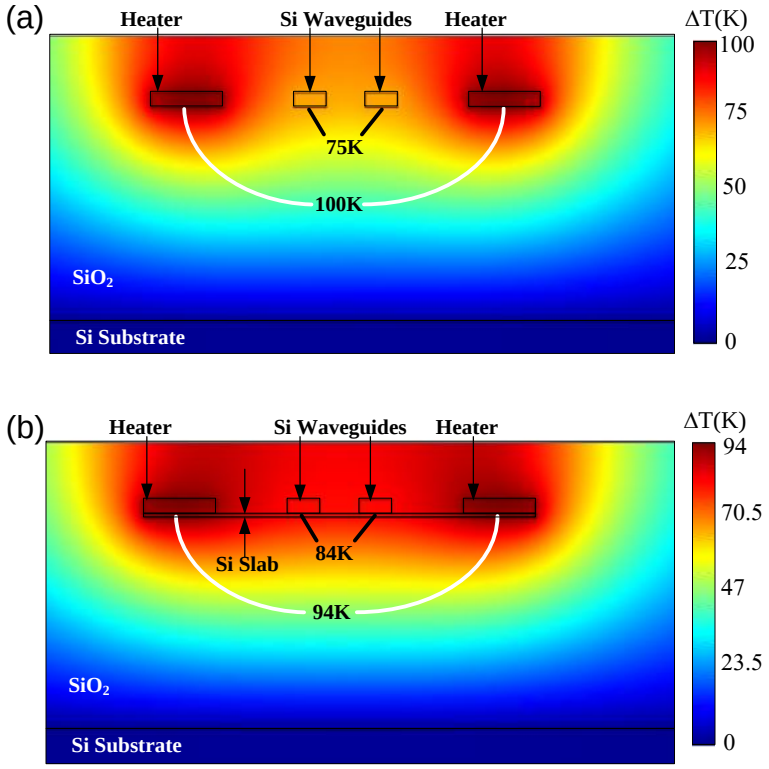

Figure 3.6: (a) Simulation of the heat distribution without slab underneath heaters and waveguide. (b) Simulation of the heat distribution with slab underneath heaters and waveguides. The same amount of energy is provided for the heaters in both simulations.

cross-section. In order to ensure more efficient heat conduction from the heaters to the waveguides, a 40 nm thin silicon slab is left underneath the 10 µm radius microrings. The heaters are made out of electron-beam evaporated nickel-chrome (nichrome) and set 1 µm away from the inner edge of the rings and 2 µm away from the outer edge, to avoid optical losses. Each of the heaters are individually connected to pads so that the heat distribution can be controlled independently. It allows that different regions of the filter can experience different values of temperature and yield distinct transfer functions. An optical microscope picture and a schematic of the fabricated device are shown in Fig. 3.8.

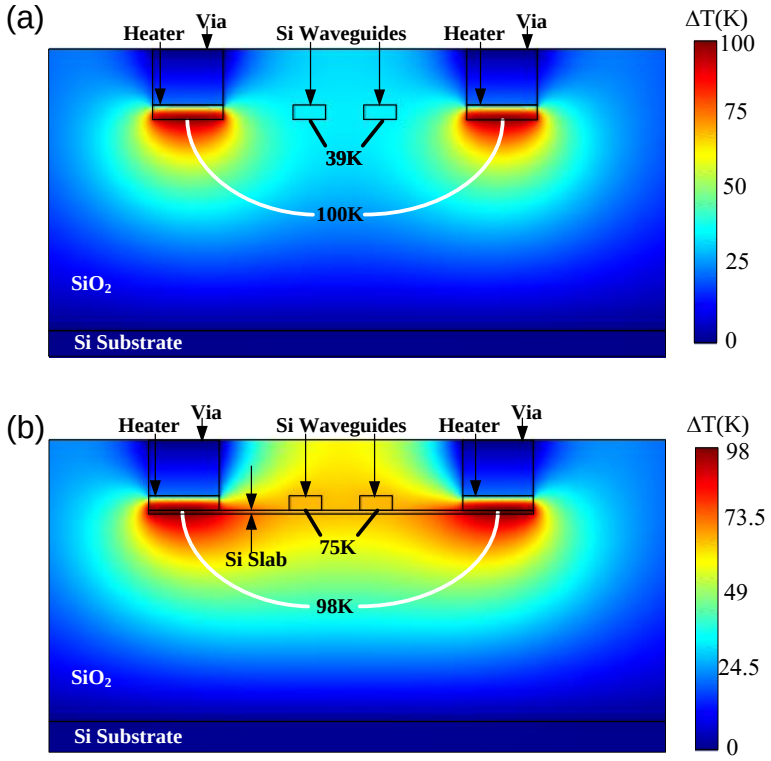

Figure 3.7: (a) Simulation of the heat distribution without slab underneath heaters and waveguide at the vias region. (b) Simulation of the heat distribution with slab underneath heaters and waveguides at the vias region. The same amount of energy is provided for the heaters in both simulations.

Figure 3.9 show the resulting spectrum of the six different configurations tested. The figures show the original spectrum (red) superimposed with the spectrum thermally tuned 15 nm away (blue), and each configuration of heaters is shown in the inset of the transfer functions. The performance of the device is evaluated by the transmission spectra of the through port, since its extinction ratio is more sensitive to thermal changes around the resonance than the drop port. In order to achieve perfectly symmetric transfer function, small fabrication errors are compensated by fine tuning the spectrum by small changes in the voltage applied to the heaters. The best two results can be observed in Fig. 3.9c and Fig. 3.9f. The latter provides a perfect match between the original transfer

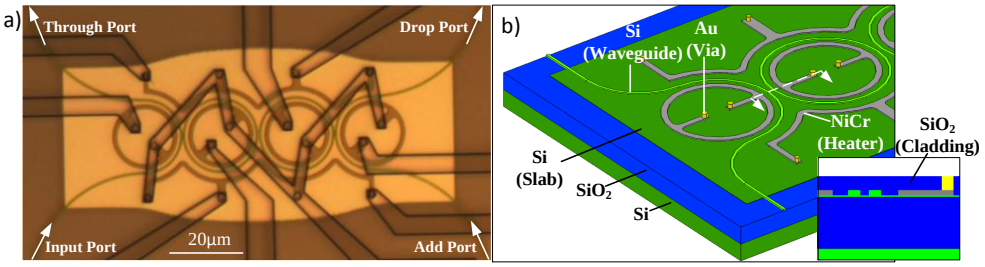

Figure 3.8: (a) Optical microscope picture of the filter before golden vias and pads are deposited on top with heaters rotated by 45°. (b) Schematics of the device with no rotation of the heaters. The inset depicts the cross section with SiO_2 cladding deposited on top.

function and the transfer function of the reallocated resonance. From the heater configuration shown in the insets, we deduce that the temperature distribution in Fig. 3.9c is described by the simplified model we propose as the optimum point of the blue in Fig. 3.5, while the temperature distribution in Fig. 3.9f is described as the optimum point of the green curve in Fig. 3.5. In both cases, the performance of the device remains high with an extinction ratio well over 10 dB and 14 dB respectively, and no noticeable change in the bandwidth (which is not the case, e.g., in Fig. 3.9 b, d and e).

We measure 17 mW/nm and 22 mW/nm power consumption for the configurations at the left and at the right of Fig. 4, respectively. The e^{-1} time-response is 11.1 μs for the falling edge and 8.4 μs for the rising edge. The maximum tunability obtained with the devices we fabricated, where nichrome heaters are placed on top of the 40-nm silicon slab, is 22.5 nm. For comparison, we also fabricated devices without the 40-nm silicon slab, achieving only 19.2 nm for the same power applied, as shown if Fig. 3.10. Therefore, the slab provided a 17% improvement in power efficiency. The power consumption can be made even lower given that it scales with the size of the rings [19].

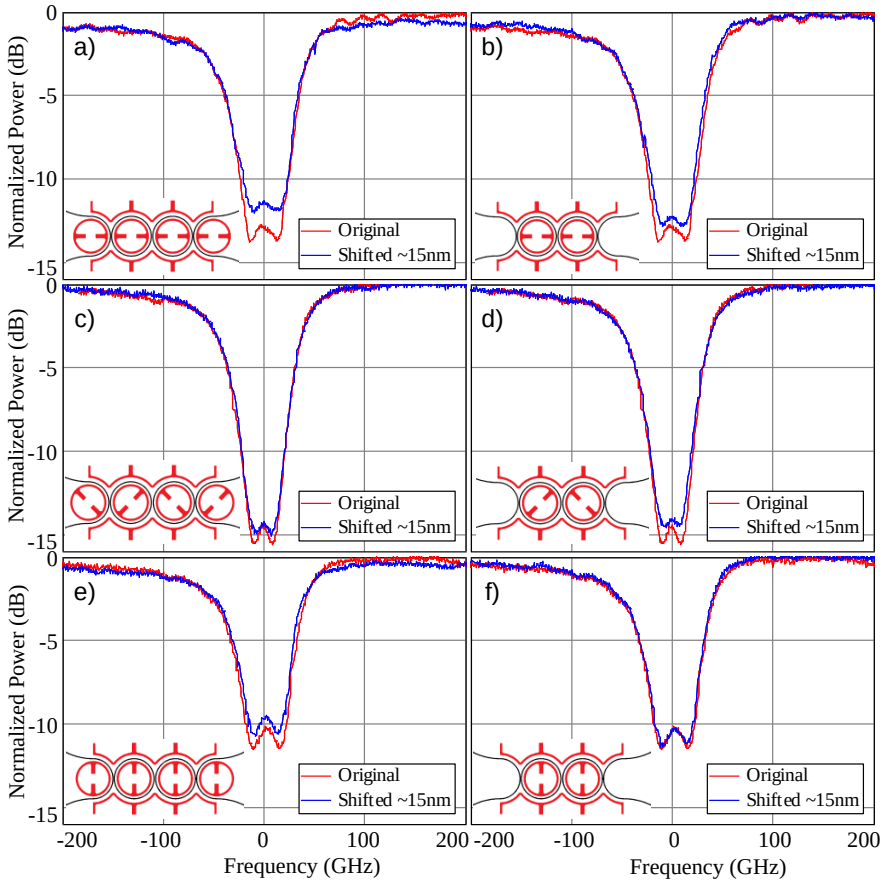

Figure 3.9: Spectrum comparison of devices with different heat distributions.

3.5 Failure test and improvement

We perform experiment to check the failure point of the heaters, to understand better its limits and to move towards larger tunability. We observed degradation of the heaters, both with and without slab underneath, after keeping the resonance shifted around 20 nm for a few seconds. They become open circuit at that point, and Fig. 3.11 shows an optical microscope picture of the failure point without slab (left) and with slab (right). While in the left the heater gets clearly

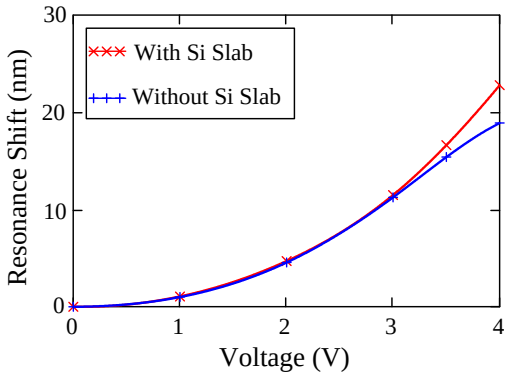

Figure 3.10: Resonance shift as a function of the voltage applied in the heaters. In red we have the shift with a 40-nm silicon slab underneath the device. In blue, we have the shift without a silicon slab.

destroyed as a typical open circuit, on the right we observe a fluid-like pattern, which may be attributed to reaction between Nickel and Silicon, forming some of the lower-temperature nickel silicides [59, 60].

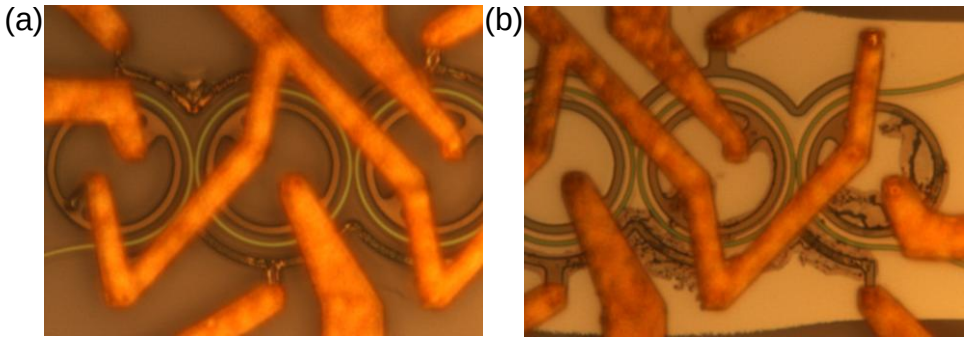

Figure 3.11: Pictures of the device in a destructive experiment. Voltage applied to the heaters is increased till they stop working. (a) Device without slab underneath: just nichrome heaters get destroyed. (b) Device with slab underneath: a melting pattern shows destruction of both nichrome heaters and silicon slab. It is most likely that a nickel-silicide formation started to happen at high temperature.

As an alternative to obtain better heaters, we fabricate silicon doped heaters, which were formed by implanting Ar^- with $1 \times 10^{19} cm^{-3}$ concentration. The

doped silicon heaters are connected to copper pads through TiN diffusion barrier. This set of materials yielded individual heaters able to handle more power then the nichrome heaters, and their performance can be observed in Fig. 3.12. The IV curved measured shows that each of them can handle up to 18 V. However, when all heaters are turned on together, we could only measure the resonance shift up to 11 V, when it becomes unstable and some of the heaters inside the ring stop working. This time, however, there was no visible damage to the heaters, and when we applied a higher voltage with a current limited power supply, the heaters are recovered and the experiment can be performed again, repeating the same behavior as the voltage is increased on all heaters. This behavior follows exactly the same procedure documented for some memristor in the literature [61].

We measure the resonance shift, as shown in Fig. 3.13 and extrapolate the it considering the characteristics shown in Fig. 3.12, which shows that a resonance shift beyond 30 nm can be achieved for the IV characteristics of the heaters.

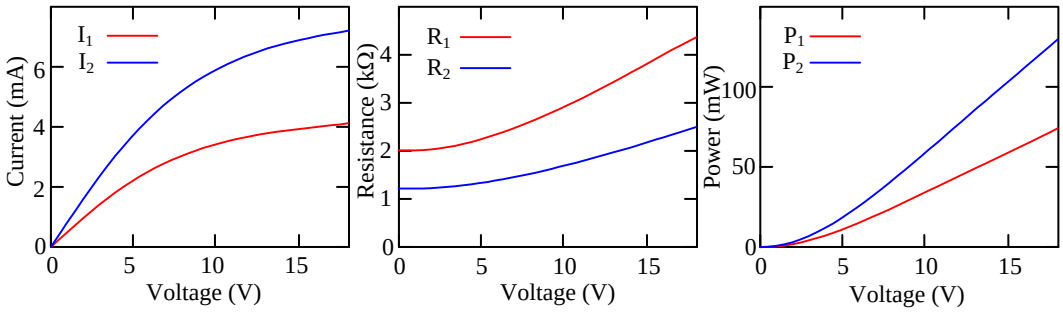

Figure 3.12: Characteristics of higher resistance (red) and lower resistance (blue) set of heaters.

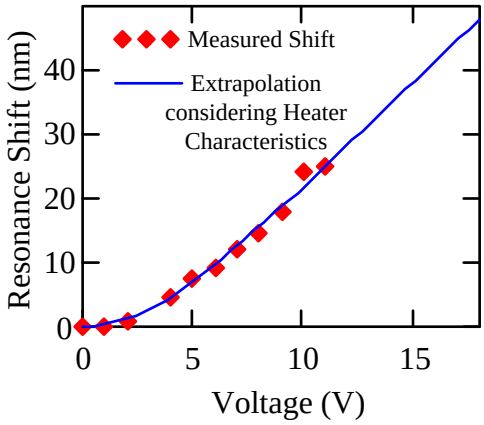

Figure 3.13: In red we have data from measured resonance shift. In blue we display the expected resonance shift considering the IV characteristic measured for the heaters.

3.6 Conclusion

We demonstrate that it is possible to achieve exactly the same transfer function for Si/SiO_2 microring tunable filters reallocated far from its original designed resonance. Such high fidelity behavior is pivotal for integrated reconfigurable WDM networks, and the modeling described here is essential for the case of higher order filters, where changes in the coupling cause strong variation in the transfer function of coupled resonator filters. We observed that doped heaters are very promising to achieve higher tunability, but its performance in our fabrication was hindered by a bistable behavior shown by some ot the resistors. A careful choice of metals and fabrication process is necessary to follow up this work and achieve extremely large and stable tunability range.

CHAPTER 4

CMOS COMPATIBLE RECONFIGURABLE FILTER FOR HIGH BANDWIDTH NON-BLOCKING OPERATION

4.1 Introduction

State-of-the-art multi-core microprocessor systems have already achieved astonishing performances, but the tradeoff between signal attenuation and bandwidth in metallic wires compromises further progress [4, 5, 6]. A compelling alternative to decouple loss and bandwidth relies on Optical Networks-on-Chip (ONoC), which opens new possibilities to network architectures with unprecedented communication bandwidth [62, 63].

Free Spectral Range (FSR) and reconfiguration dynamics of individual filters are two pivotal points which set boundaries to the overall capacity of an ONoC. Both are important for most metrics involving networks efficiency, being crucial factors on the overall aggregate bandwidth and network latency, respectively. The aggregate bandwidth of an ONoC is limited by the sum of the bandwidths of all channels comprising the network, which is ultimately limited by the FSR of individual channels. And a reconfigurable network might suffer unnecessary latency if single channel reallocation requires disabling other channels.

Here, by the proper operation of a Mach-Zehnder interferometer (MZI) enhanced second-order microring-resonator filter, we demonstrate a non-blocking – or hitless [32] – reconfigurable filter with large FSR. The ability to efficiently increase the number of channels in a network has been demonstrated in passive non-reconfigurable structures, in a variety of ways, for example, by using small

microring resonators [64, 65, 66], Vernier filters [67, 68], and by merging MZI's with microring resonators (Fig. 4.1a) [68, 69, 70, 71, 72]. The last approach is chosen for this work because it has the interesting features of doubling the FSR without imparting high radiation losses (intrinsic to tight bends) and without the typical insertion loss for misaligned resonances (intrinsic to Vernier filters).

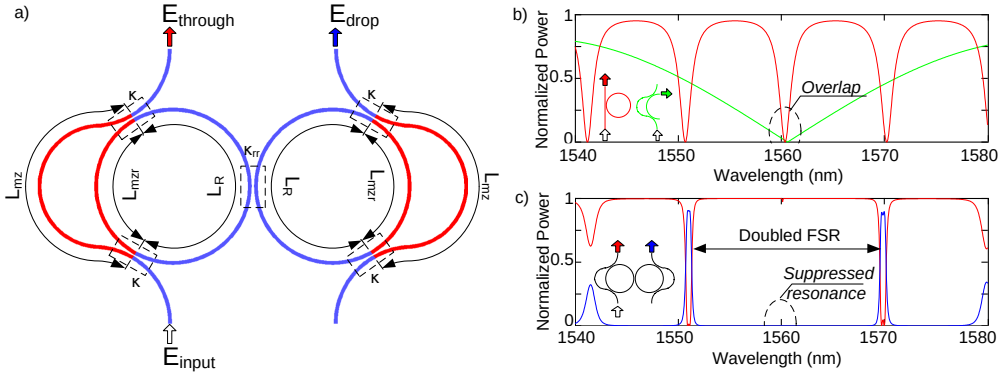

Figure 4.1: (a) Schematics of a second-order filter with MZ arms. (b) Transfer function of a microring resonator (red) and effective coupling κ_{eff} of a MZI (green). (c) Transfer function of through (red) and drop (blue) ports of the filter.

4.2 Description, synthesis and non-blocking operation

The device, shown in Fig. 4.1a, consists of a modified second-order microring-resonator filter, where the coupling between the microring and the waveguide is MZI assisted with a two-point coupling topology instead of the usual single-point coupling (red inset in Fig. 4.1b). The MZI is composed of 2 arms with lengths L_{mz} and L_{mzr}, with equal field coupling κ for both coupling regions, as shown in Fig. 4.1a. The MZI provides a periodic wavelength dependency for the coupling between bus waveguides and resonators, with periodicity set by the arm length difference $\Delta L = L_{mz} - L_{mzr}$. In Fig. 4.1b, the spectral responses

of the ring and of the MZI are shown in red and green, respectively. For a given relation between the values of ΔL and κ one can achieve the removal of a resonance of the microring leading to a doubled FSR filter with a box-like transfer function, as shown in Fig. 4.1c.

In order to determine the required values of ΔL and κ, one needs to ensure that the minimum coupling κ_{eff} of the MZI overlaps with the resonance to be suppressed. The coupling (κ_{eff}) and transmission (τ_{eff}) coefficients of an MZI are extracted from the input to output transfer function

$$\begin{pmatrix} E_{out1} \\ E_{out2} \end{pmatrix} = \exp\left(i\frac{2\pi}{\lambda}n_{eff}(\lambda,T)\frac{L_{mz}+L_{mzr}}{2}\right)\cdot\begin{pmatrix} \tau_{eff} & i\cdot\kappa_{eff} \\ i\cdot\kappa_{eff} & \overline{\tau_{eff}} \end{pmatrix}\begin{pmatrix} E_{in1} \\ E_{in2} \end{pmatrix} \tag{4.1}$$

with

$$\kappa_{eff}(\lambda,T) = 2\kappa t\cos\left(\frac{2\pi}{\lambda}n_{eff}(\lambda,T)\frac{\Delta L}{2}\right) \tag{4.2}$$

$$\tau_{eff}(\lambda,T) = 2\tau^2\cos\left(\frac{2\pi}{\lambda}n_{eff}(\lambda,T)\frac{\Delta L}{2}\right) - \exp\left(-i\frac{2\pi}{\lambda}n_{eff}(\lambda,T)\frac{\Delta L}{2}\right) \tag{4.3}$$

where n_{eff} is the effective refractive index of the waveguides comprising the MZI, which is a function of wavelength λ and temperature T. Therefore, the minimum coupling at the wavelength λ_0 is obtained when $\kappa(\lambda_0) = 0$, which leads to:

$$\Delta L(m_2) = \frac{\lambda_{m_1}}{n_{eff}(\lambda_{m_1})}\cdot\left(m_2-\frac{1}{2}\right)\ , m_2\in\mathbb{N}^* \tag{4.4}$$

where the wavelength λ_{m_1} is obtained from the resonance condition of a microring:

$$2\pi R n_{eff}(\lambda_{m_1}) = m_1\lambda_{m_1}\ , m_1\in\mathbb{N}^* \tag{4.5}$$

Combining Eq. 4.2 and Eq. 4.5, we have the equation for the effective coupling at λ_{m_1-1}:

$$\kappa_{eff}(\lambda_{m_1-1}) = 2\kappa\tau\cos\left[\frac{m_1-1}{2m_1}\left(1+2m_2\right)\pi\right] \tag{4.6}$$

Therefore the coupling κ is given by:

$$\kappa(m_2) = \sqrt{\frac{1}{2} - \frac{1}{2}\sqrt{1 - \kappa_{eff}^2(\lambda_{m_1-1})\left[\sin\left(\frac{1+2m_2}{2m_1}\pi\right)\right]^{-2}}} \tag{4.7}$$

In order to obtain real solutions, minimum and maximum boundaries are set for the possible values of m_2:

$$\frac{m_1}{\pi}\text{asin}\left[\kappa_{eff}(\lambda_{m_1-1})\right] - \frac{1}{2} \leqslant m_2 \leqslant \frac{m_1}{\pi}\left\{\pi - \text{asin}\left[\kappa_{eff}(\lambda_{m_1-1})\right]\right\} - \frac{1}{2} \tag{4.8}$$

The geometry of the device is determined by choosing values for m_1 and m_2 that obey Eq. 4.8, which are then used to calculate ΔL and κ using Eqs. 4.4 and 4.7, while the bandwidth and passband ripple of the box-like filter are determined by the effective coupling $\kappa_{eff}(\lambda_{m_1-1})$ and ring to ring coupling κ_{rr}, which are obtained from filter synthesis methods [13, 42, 43, 73]. For example, Fig. 4.2 shows a few possibilities of transfer functions for different values of m_1 and m_2 and fixed values of $\kappa_{eff}(\lambda_{m_1-1})$ and κ_{rr}. The examples shown in Figs. 4.2a, b, and c are for $m_2 = (m_1 - 1)/2$, $m_2 = (m_1 - 1)/3$, and $m_2 = (m_1 - 1)/5$, which result in $\Delta L = 2\pi R/2$, $\Delta L \approx 2\pi R/3$, and $\Delta L \approx 2\pi R/5$, respectively, all of them with 60 GHz flatband bandwidth and -20 dB passband ripple at resonance. All figures show a doubled FSR around the suppressed resonance at λ_{m_1}, with a box-like resonance at the next resonance at λ_{m_1-1} and distinct behavior for further resonances. In Fig. 4.2a, every other resonance is removed, while in Fig. 4.2b one out of every three resonances is removed, and in Fig. 4.2c one out of every five resonances is removed. We observe that the coupling, shown in green, is more (less) sensitive around the resonance λ_{m_1-1} (λ_{m_1}) for smaller m_2 values, which can be an important criteria when choosing the design parameters for specific applications.

In order to obtain non-blocking operation of the filter, the following se-

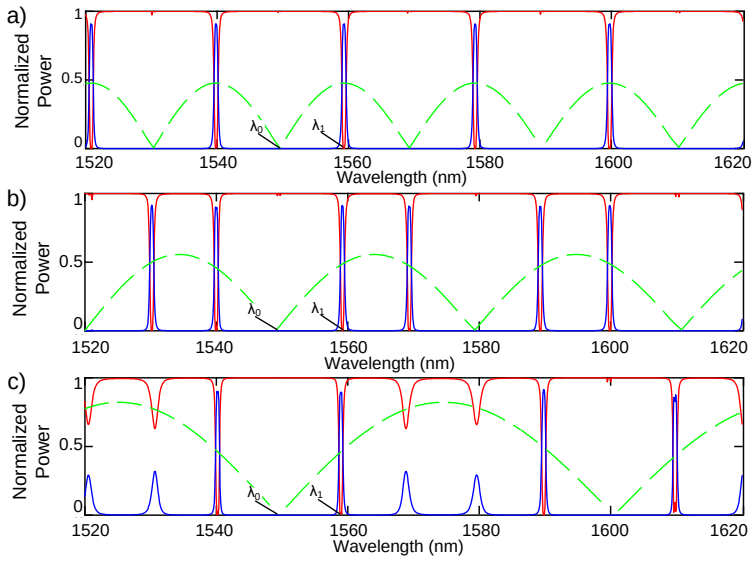

Figure 4.2: Examples of possible transfer function. In red we have the through port, the drop port is in blue, and, in green, we have the wavelength dependency of the effective coupling κ_{eff} for (a) $m_2 = (m_1 - 1)/2$, (b) $m_2 = (m_1 - 1)/3$, and (c) $m_2 = (m_1 - 1)/5$. All simulations considered 10 µm radius silicon microrings, surrounded by SiO_2, with 6 dB/cm propagation losses.

quence of 3 events is implemented: the refractive index of the microring and of the MZI at the right is modified, which changes the box-like filter into an all-pass filter; the refractive index of the entire structure is modified altogether, moving the all-pass filter to a new wavelength; and finally the excess change in the refractive index of the microring and MZI at the right is removed, so that the all-pass filter transitions back to a box-like filter at a new wavelength. We make use of the strong thermo-optical effect present in silicon to change the refractive index and achieve non-blocking tuning [15].

Figure 4.3 shows the transmission response of the structure and its non-blocking nature following the three steps of temperature tuning outlined above. The through port and drop port transmissions (E_t and E_d, respectively) where

plotted using

$$E_t = \frac{\tau_{Left} - a\tau_{Left}\tau_{rr}\overline{\tau_{Right}}\phi_{Right} - a\tau_{rr}\phi_{Left} + a^2\overline{\tau_{Right}}\phi_{Right}\phi_{Left}}{1 - a\left(\phi_{Left}\overline{\tau_{Left}} + \phi_{Right}\overline{\tau_{Right}}\right)\tau_{rr} + a^2\phi_{Left}\overline{\tau_{Left}}\phi_{Right}\overline{\tau_{Right}}}\phi_1 E_i \tag{4.9}$$

$$E_d = \frac{-ia\kappa_{Left}\kappa_{rr}\kappa_{Right}\sqrt{\phi_{Left}\phi_{Right}}}{1 - a\left(\overline{\tau_{Left}}\phi_{Left} + \overline{\tau_{Right}}\phi_{Right}\right)\tau_{rr} + a^2\overline{\tau_{Left}}\phi_{Left}\overline{\tau_{Right}}\phi_{Right}}\sqrt{\phi_1\phi_2}E_i \tag{4.10}$$

where

$$\phi_{Left/Right} = \exp\left[i\frac{2\pi}{\lambda}n_{eff}(T_{Left/Right})\left(2\pi R + \frac{\Delta L}{2}\right)\right] \tag{4.11}$$

$$\phi_{1/2} = \exp\left(i\frac{2\pi}{\lambda}n_{eff}(T_{Left/Right})\frac{L_{mz} + L_{mzr}}{2}\right) \tag{4.12}$$

$$a = \exp\left[-\alpha\left(\pi R + \Delta L\right)\right] \tag{4.13}$$

where $\tau_{Left} = \tau_{eff}(T_{Left})$, $\kappa_{Left} = \kappa_{eff}(T_{Left})$, $\tau_{Right} = \tau_{eff}(T_{Right})$, and $\kappa_{Right} = \kappa_{eff}(T_{Right})$, and α is the propagation loss. T_{Left} is the temperature of the left microring and of the Mach-Zehnder arm connected to it, and T_{Right} is the temperature of the right microring and of the Mach-Zehnder arm connected to it. Figure 4.3(i) shows the transmission when $T_{Left} = T_{Right} = T_0$. Figure 4.3(ii) shows the transfer function when the temperature of right ring and MZI is increased to $T_{Right} = T_1$, obtaining an all-pass filter. Figure 4.3(iii) shows the transfer function when the temperature of the full device is increased by T_F so that $T_{Right} = T_1 + T_F$ and $T_{Left} = T_F$, shifting the all-pass filter to a new location. Finally, Figure 4.3(iv) shows the transfer function when temperature of the right side of the device is reduced to T_F, reallocating the box-like transfer function at a new wavelength. Even though it is clear in Fig. 4.3 that the reconfiguration process does not block other channels, we observe that it imparts about 1 dB insertion loss to the intermediate wavelengths. Optimization of design parameters can be used to reduce even more such reconfiguration insertion loss.

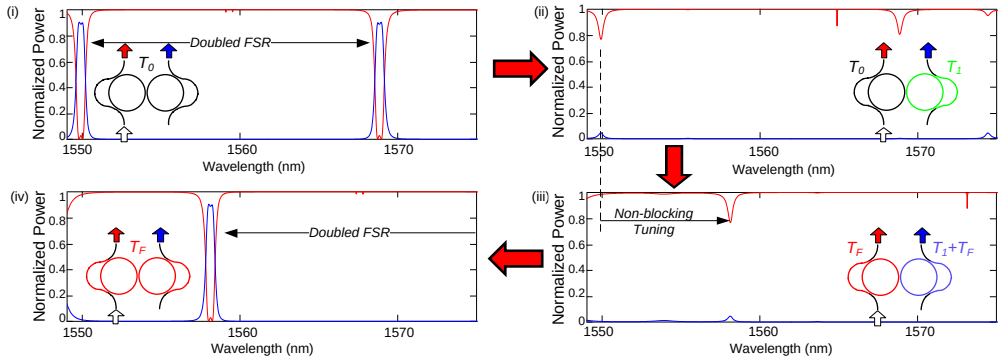

Figure 4.3: Non-blocking tuning. (i) Initial transfer function of the filter, with the whole structure at the same temperature T_0. (ii) All-pass transfer function after the right side of the filter is at temperature T_1. (iii) The all-pass transfer function is shifted completely by increasing the temperature of the whole structure by T_F. (iv) Final transfer fuction, obtained by reducing the temperature of the right side down to T_F.

4.3 Fabrication, Experiment and Results

We fabricated the structure using a CMOS-compatible process. As shown in Fig. 4.4a, doped Si heaters were formed inside the microrings and in the surroundings of the external arms of the MZI's. The cross section of the heaters is 215 nm high by 1000 nm wide, while the cross section of the crystalline silicon waveguides is 215 nm high by 450 nm wide. A thin 35 nm silicon slab is left underneath the structure to enhance the heat transfer from the heaters to the waveguides. The overall structure is fabricated on an SOI wafer with a 3 µm buried oxide and is clad with a 1.2 µm of SiO_2. Vias are etched for electrical contacts, where a thin stack of TiSi and TiN is formed prior to the evaporation of the Cu wirings and pads. The final structure is shown in Fig. 4.4b.

The transfer function of the device fabricated is measured as shown in Fig. 4.5a, where a doubled FSR of 19.2 nm can be observed for the 10 µm ra-

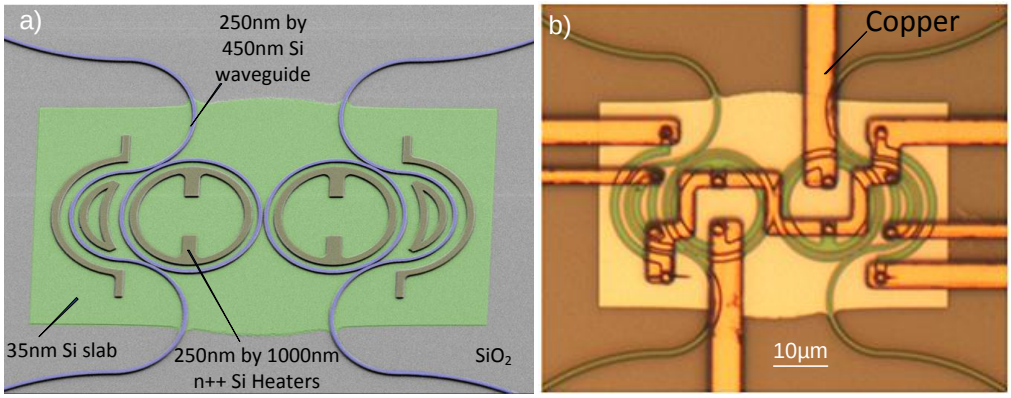

Figure 4.4: (a) False-color Scanning Electron Microscope picture of the device. The waveguides are shown in blue, heaters in brown and a thin silicon slab underneath the structure is shown in green (no metal contacts shown). (b) Optical microscope picture of the final structure, with copper wiring connected through round vias to the heaters.

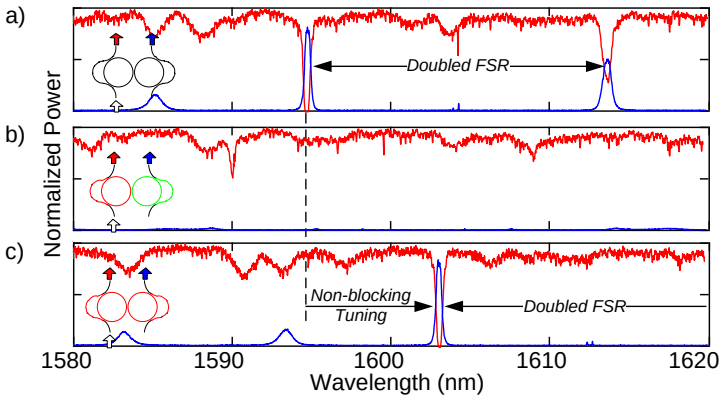

Figure 4.5: (a) Original spectrum of the device, with through (red) and drop (blue) ports presenting the doubled FSR. (b) Spectrum after changing the effective index of the cavity coupled to the drop port. No resonances are observed. (c) New resonance of the filter after non-blocking tuning.

dius microrings, with its main resonance at 1594.6 nm. The residual power dropped at the suppressed resonance (at 1604.2 nm) is about 16 dB below the signal level. In Figs. 4.5b and 4.5c we demonstrate the non-blocking tuning of the fabricated filter. For the first step of the non-blocking tuning, we apply 28 mW to the heater inside the microring connected to the drop port, which changes the box-like transfer function (Fig. 4.5a) to an all pass transfer function (Fig. 4.5b), as expected. In Fig. 4.5c we show the final step of the tuning, where a new central resonance wavelength, at 1603.1 nm, is observed under 115 mW of heat power applied for all heaters. Non-blocking operation is clear from the experimental results, confirming that a doubled FSR filter can be reconfigured from a wavelength to another with negligible insertion loss for intermediate wavelengths.

4.4 Conclusion

We fabricate and characterize a CMOS-compatible, Mach-Zehnder-coupled, second-order-microring-resonator filter with doubled free spectral range and demonstrate non-blocking thermo-optical filter reconfiguration. We demonstrate that non-blocking tuning can be achieved for a doubled FSR filter, which translates to a higher throughput for NoC's. It is important to note that in the current configuration, when the device is reconfigured and the refractive index of part of the structure is modified to achieve the all-pass filter, an overcoupled resonance is obtained, which still has a small power penalty and imparts some loss (< 1 dB) on other channels allocated between the initial and final wavelength. Even though the procedure described does not block the communication of other channels, its power penalty must be considered in the network design,

and may limit the number of channels that can be reconfigured simultaneously.

CHAPTER 5

ELECTRICALLY-DRIVEN OPTICAL-ISOLATOR

5.1 Introduction

Isolators are fundamental for the operation of optical networks on chip (ONoC). They protect lasers from damage caused by reflections in the network, improving their stability both in wavelength and power.

Traditional isolators rely on Faraday rotation induced by magnetic fields [74, 75, 76], and therefore are based on materials that are not CMOS compatible, which prevents their integration in current microelectronic systems. Recently several mechanisms have been suggested to provide nonreciprocity based on non-magnetic methods. Mechanisms making use of nonlinear effects [77] or radiation pressure, in a non-linear mechanical topology [78] have been theoretically shown to have the ability to provide optical isolation when an individual signal comes from only one direction; however they fail to isolate in the important scenario when there are signals propagating forward and backward simultaneously. The use of a complex modulation in a waveguide [79] have been recently suggested as a possibility for inducing one-way modal conversion. However, such static devices are reciprocal as it is constraint by Maxwell's equations [80] and therefore cannot be used to construct any non-reciprocal optical devices, including isolators and circulators.

Here we show for the first time an electro-optical isolator, on silicon, based on indirect interband photonic transition [81] induced by a traveling electrical wave that provides dynamic index modulation in a waveguide. The struc-

ture used here supports two optical modes: a symmetric and anti-symmetric as shown in Fig. 5.1. A traveling wave modulation with frequency and wavenumber matches the difference in frequency and wavenumber between the original mode and a second mode of the waveguide propagating in one direction, as shown in Fig 5.3 (left) and induces mode conversion. When the propagation is in the opposite direction, as shown in Fig. 5.3 (right) the traveling wave's frequency and wavenumber does not correspond to the difference in frequency and wavenumber between the original mode and any other existing mode and therefore no conversion occurs. Figure 5.3 shows the mode amplitudes as the light propagates from one direction to the other obtained using coupled mode equations [81], using the wavenumbers obtained for a 10 GHz index modulation in the structure with dimensions w = 450 nm, h = 215 nm, t = 35 nm and d = 500 nm. One can see that total conversion is expected when light propagates from right to left while minimal conversion (<2% in the example shown) is expected when light propagates from left to right. The different transmission of the symmetrical modes in the forward and backward directions clearly shows the nonreciprocity of the dynamic modulated system.

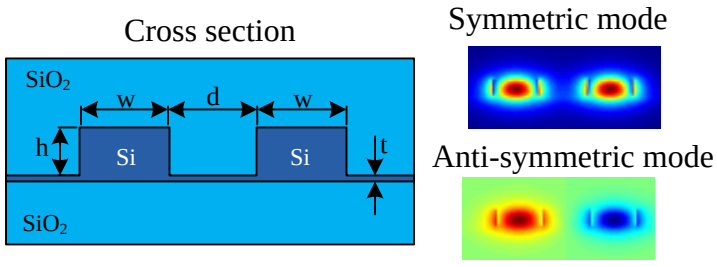

Figure 5.1: Waveguide geometry and materials.

In order to realize the isolation, we add 1x2 MMI's to the edges of the structure. When no mode conversion occurs (Fig. 5.4 top), the MMI at the output

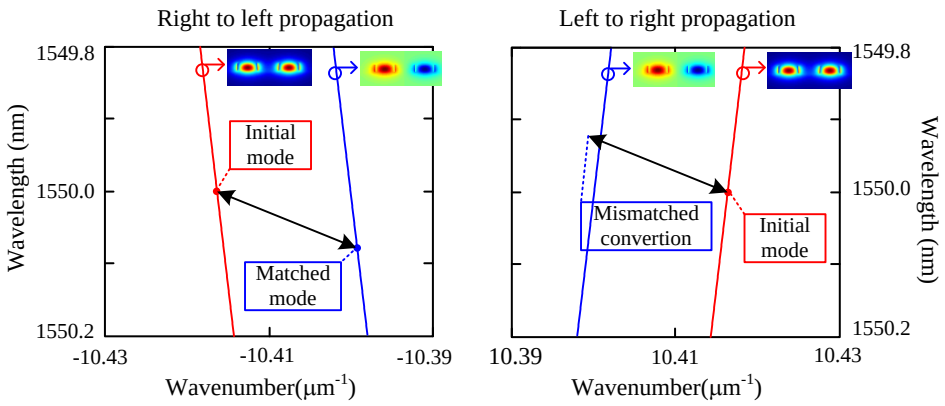

Figure 5.2: Dispersion relation for symmetric (red) and anti-symmetric (blue) modes of coupled waveguides. The black arrow represents the traveling-wave permittivity modulation. In the left, it matches the initial mode to another mode, while in the right it is observed conversion mismatch.

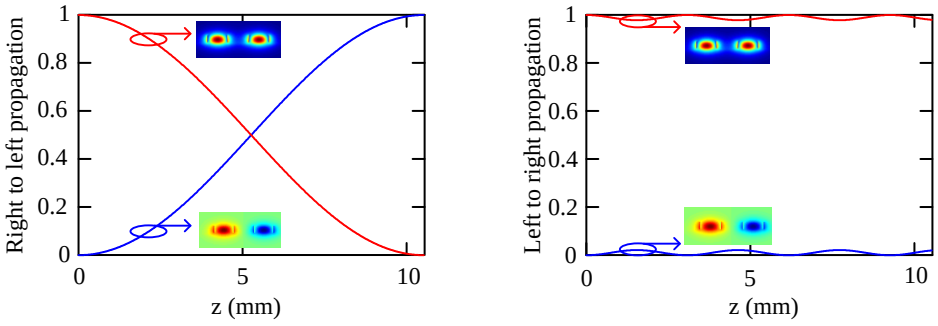

Figure 5.3: Dynamics of the mode conversion. Right to left propagation achieves full conversion from one mode to the other, while left to right propagation does not.

converts the symmetric mode back to the mode of the output waveguide. When conversion does occur, the MMI at the output cannot convert the mode to the mode of the output waveguide, and as a result light is dissipated providing isolation. Fig. 5.5 shows a 2D FEM simulation in time domain of the mode conversion. The input signal was set at 1550 nm, and the permittivity modulation with maximum $\Delta\varepsilon = 0.29122$, at 10 THz with wavenumber $q = 76285.3m^{-1}$.

The total length of the waveguide is 31.5 µm. Note that in order to induce conversion the overlap integral between the modulation spatial distribution and the initial and final modes should be non zero [81] and therefore the modulation cannot be symmetrical across the structure cross-section. In the simulation the modulation is induced only in the the lower half of the waveguide. Simulations with modulation frequency down to 100 GHz were successfully performed, with $q = 25984.8m^{-1}$, $\Delta\varepsilon = 0.0182$ and device length of 0.413 mm, with mode conversion observed in only one direction, which shows the scalability of the principle. The increase of length is required because light travelling needs to experience at least one modulation period to attain efficient mode conversion, which consequently requires considerably more computational power.

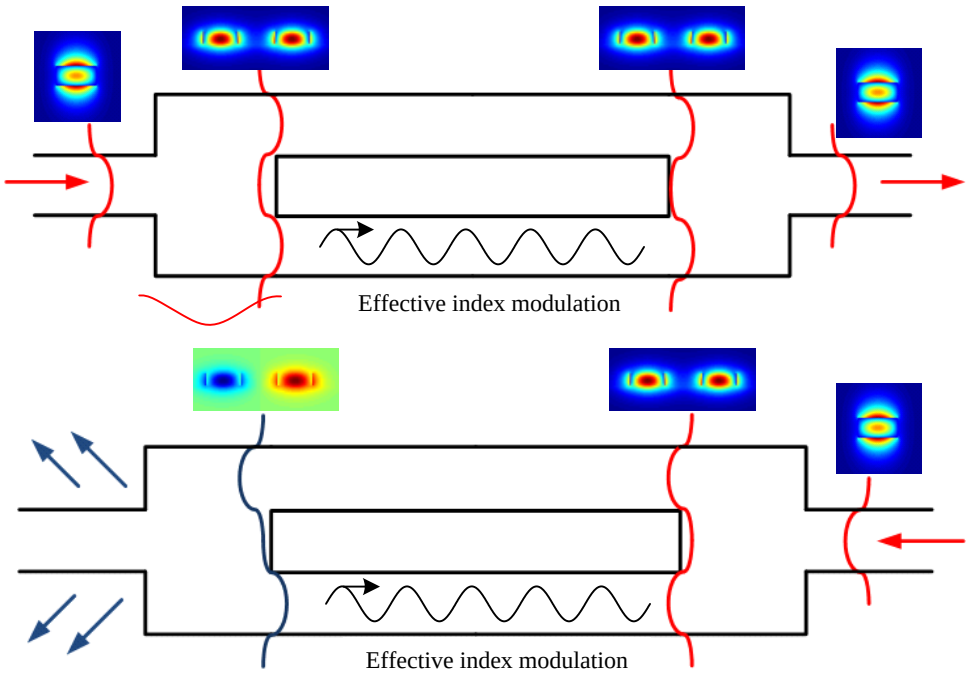

Figure 5.4: Schematic of the isolator. A single mode waveguide feeds a 1x2 MMI, which provides the symmetric mode for the isolator. By modulating the refractive index of one waveguide we obtain a non-zero overlap between the modes and modulation. In one direction the symmetric mode is converted to the anti-symmetric mode, but it is not converted in the other direction.

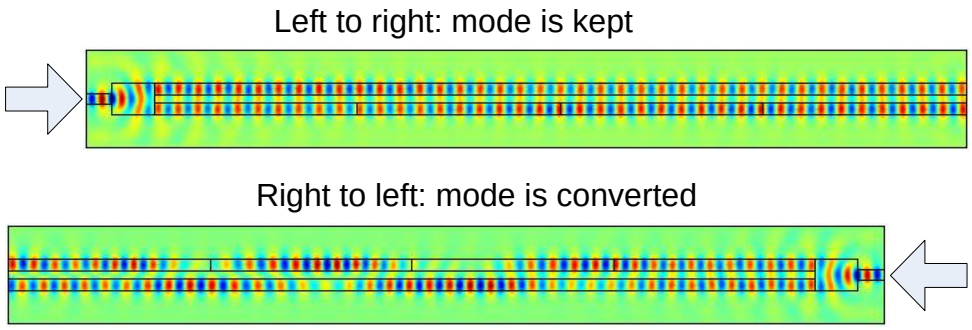

Figure 5.5: FEM time-domain simulation showing the conversion occurring in only one propagation direction.

5.2 Theoretical Background

In order to derive the equations that describe the conversion between modes achieved by a traveling-wave modulation of the permittivity of a waveguide, we start from the wave equation for the electric field where the perturbation is present in the polarization vector [82]:

$$\nabla^2 \vec{E} - \frac{1}{c}\frac{\partial^2 \vec{E}}{\partial t^2} = \frac{4\pi}{c^2}\frac{\partial^2 \vec{P}}{\partial t^2} \tag{5.1}$$

For conversion happening only in the propagation direction, we only need to consider the longitudinal component:

$$\frac{\partial^2 \vec{E}}{\partial z^2} - \frac{1}{c}\frac{\partial^2 \vec{E}}{\partial t^2} = \frac{4\pi}{c^2}\frac{\partial^2 \vec{P}}{\partial t^2} \tag{5.2}$$

Assuming a wave solution with amplitude dependence, we have:

$$\vec{E} = A(z)e^{\imath(\omega t - kz)} \tag{5.3}$$

Putting 5.3 into 5.2 we obtain

$$\frac{d^2 A}{dt} - \frac{k^2}{A} - 2\imath k\frac{dA}{dz} + \frac{\omega^2}{c^2}A = \frac{4\pi}{c^2}\frac{d^2 P}{dt^2} \tag{5.4}$$

Using the Slow Varying Amplitude Approximation, we can neglect the first term of the left side. The second and the forth terms cancel each other. Finally we obtain:

$$\frac{dA}{dz} = \imath \frac{2\pi}{\omega c} \frac{d^2 P}{dt^2} \tag{5.5}$$

Equation 5.5 is the main equation for mode conversion. We need to obtain P as a function of the permittivity modulation so that we can solve Eq. 5.5 and verify the conditions for mode conversion.

Assuming that we have two modes with transversal distribution $U_1(x, y)$ at frequency ω_1 and wavenumber k_1 and $U_2(x, y)$ at frequency ω_2 and wavenumber k_2:

$$\vec{E} = U_1(x, y)A_1(z)e^{\imath(\omega_1 t - k_1 z)} + U_2(x, y)A_2(z)e^{\imath(\omega_2 t - k_2 z)} + c.c. \tag{5.6}$$

The polarization $\vec{P}$ is given by

$$\vec{P} = \varepsilon_0 \chi \vec{E} \tag{5.7}$$

where

$$\chi = \varepsilon_r - 1 \tag{5.8}$$

The nonlinear part is given by

$$\chi^{NL} = \varepsilon_r \tag{5.9}$$

For

$$\varepsilon_r = \varepsilon_{r0} + \delta\varepsilon e^{\imath(\Omega t - qz)} + c.c. \tag{5.10}$$

we obtain, plugging 5.10 and 5.6 into 5.7:

$$\begin{aligned}\vec{P} = U_1(x, y)A_1(z)e^{\imath[(\omega_1+\Omega)t-(k_1+q)z]} + U_1(x, y)A_1(z)e^{\imath[(\omega_1-\Omega)t-(k_1-q)z]} + \\ U_2(x, y)A_2(z)e^{\imath[(\omega_2+\Omega)t-(k_2+q)z]} + U_2(x, y)A_2(z)e^{\imath[(\omega_2-\Omega)t-(k_2-q)z]} + c.c.\end{aligned} \tag{5.11}$$

For electrical field propagation in the reverse direction ($-z$), we replace k_1 and k_2 by $-k_1$ and $-k_2$ and obtain

$$\vec{P} = U_1(x,y)A_1(z)e^{\imath[(\omega_1+\Omega)t-(-k_1+q)z]} + U_1(x,y)A_1(z)e^{\imath[(\omega_1-\Omega)t-(-k_1-q)z]} + U_2(x,y)A_2(z)e^{\imath[(\omega_2+\Omega)t-(-k_2+q)z]} + U_2(x,y)A_2(z)e^{\imath[(\omega_2-\Omega)t-(-k_2-q)z]} + c.c. \quad (5.12)$$

Now we need to plug the equations above in Eq. 5.5, obtain the solution when there is phase matching or not and verify when conversion occurs for each direction of propagation.

The permittivity modulation is given by:

$$\Delta\varepsilon(x,z,t) = \delta\varepsilon(x)\cos(\Omega t - (-q)z) \quad (5.13)$$

A waveguide which only support two modes, we have that the total field is a superposition of the two modes amplitudes A_1 and A_2:

$$\vec{E}(x,z,t) = A_1(z)E_1(x)e^{\imath(\omega_1 t - k_1 z)} + A_2(z)E_2(x)e^{\imath(\omega_2 t - k_2 z)} + cc \quad (5.14)$$

From Eq. 5.5, we obtain the coupled mode equations [82]:

$$\begin{cases} \frac{dA_1(z)}{dz} = iCe^{-\imath\Delta k z}A_2(z) \\ \frac{dA_2(z)}{dz} = iCe^{\imath\Delta k z}A_1(z) \end{cases} \quad (5.15)$$

Where

$$\begin{aligned} \Delta k &= k_2 - k_1 - (-q) \\ C &= \tfrac{\varepsilon_0}{8}\omega \int_{-\infty}^{\infty} \delta(x)E_1(x)E_2(x)dx \end{aligned} \quad (5.16)$$

$\delta(x)$ is the profile of the perturbation. For two modes E_1 and E_2 with even and odd symmetries respectively, $\delta(x)$ cannot be even in order to have $C \neq 0$.

For initial conditions:

$$\begin{cases} A_1(0) = 1 \\ A_2(0) = 0 \end{cases} \quad (5.17)$$

we obtain the solution:

$$\begin{cases} A_1(z) = e^{i\frac{\Delta k}{2}z}\left[i\frac{\Delta k}{2\gamma}\sin(\gamma z) + \cos(\gamma z)\right] \\ A_2(z) = i\frac{C}{\gamma}e^{i\frac{\Delta k}{2}z}\sin(\gamma z) \end{cases} \tag{5.18}$$

With

$$\gamma = \sqrt{\left(\frac{\Delta k}{2}\right)^2 + C^2} \tag{5.19}$$

For perfect phase matching, we have:

$$\begin{cases} \Omega = \omega_2 - \omega_1 \\ -q = k_2 - k_1 \end{cases} \tag{5.20}$$

Therefore $\Delta k = 0$, $\gamma = C$, and:

$$\begin{cases} A_1(z) = \cos(Cz) \\ A_2(z) = i\sin(Cz) \end{cases} \tag{5.21}$$

The coherence length is given by:

$$C \cdot l_c = \frac{\pi}{2} \Rightarrow l_c = \frac{\pi}{2C} \; or \; C = \frac{\pi}{2l_c} \tag{5.22}$$

In the other direction, the phase mismatch is given by $\Delta k = 2(k_2 - k_1)$. In this case, the amplitudes are:

$$\begin{cases} A_1(z) = e^{-i(k_2-k_1)z}\left[\imath\frac{k_2-k_1}{\sqrt{(k_2-k_1)^2+C^2}}\sin\left(\sqrt{(k_2-k_1)^2+C^2}z\right) + \right. \\ \qquad\qquad \left. + \cos\left(\sqrt{(k_2-k_1)^2+C^2}z\right)\right] \\ A_2(z) = \imath\frac{C}{\sqrt{(k_2-k_1)^2+C^2}}e^{i(k_2-k_1)z}\sin\left(\sqrt{(k_2-k_1)^2+C^2}z\right) \end{cases} \tag{5.23}$$

Figure 5.3 shows complete mode conversion when light travels in one direction while small conversion with higher periodicity happens for the signal propagation on the other direction.

5.2.1 Parallel Waveguides

A very large separation between k-vectors happens when a single waveguide guide two modes, as shown in Fig. 5.6, requiring index modulation of the order of terahertz and modulation wavelength on a sub-micrometer length scale. A way to bring this separation to more feasible values is by having two parallel waveguides set aside, as if they were a long directional coupler, as shown in Fig. 5.2. Since the modes result from splitting of their own single modes in a symmetric and anti-symmetric set of supermodes, the separation can be arbitrarily set according to the distance among them. With this configuration in mind we obtain the propagation constants of the guided modes.

As a first approximation, we obtain the slab equivalent for the channel waveguide we are working with, using the Effective Index Method. Then, we obtain the propagation constant for the symmetric and anti-symmetric modes at the frequencies ω_1 and $\omega_2 = \omega_1 + \Delta\omega$, where $\Delta\omega$ is the frequency of the refractive index travelling-wave modulation. Top insets of Fig. 5.7 show a wavelength where conversion happens on the forward direction but not in the backward. Bottom insets of Fig. 5.7 show a wavelength where conversion happens on the backward propagation direction but not in the forward.

5.3 Electrical Design

Electrical modulation limits the possible frequency of the signal on 10's of gigahertz. According to the dispersion relation, the k-vector required for such a frequency points to wavelengths of the order of 100's of micrometers. Unfor-

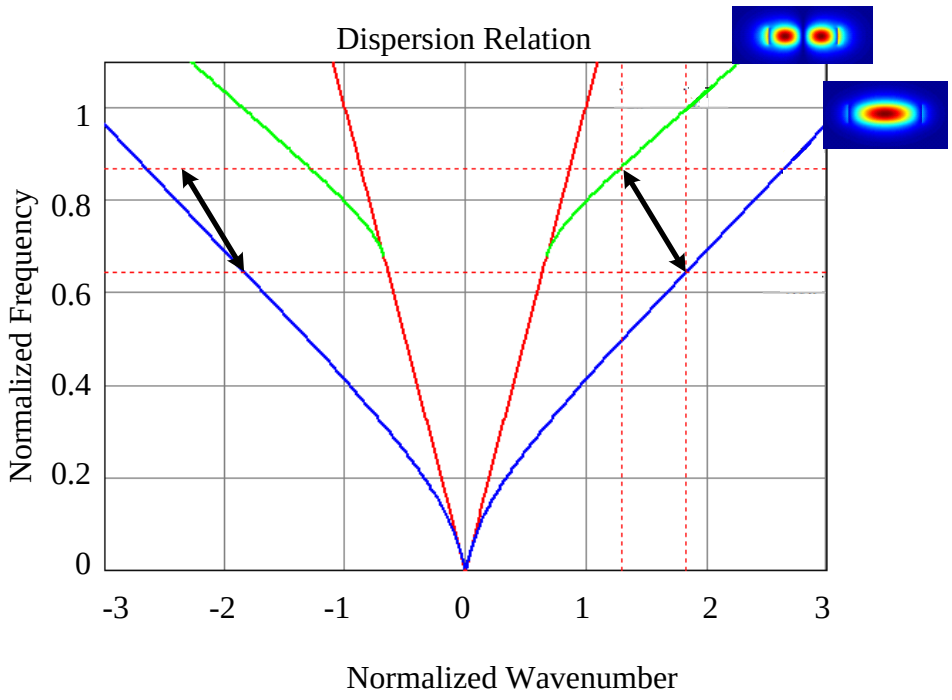

Figure 5.6: Example of single waveguide supporting two modes. Theoretically it is possible to provide the conversion from one mode to the other. Unfortunately, it requires index modulation on the order of terahertz, and modulation wavelength on the order of nanometers, unfeasible with electrical modulation.

tunately, a simple transmission line operating at 10's of gigahertz have wavelength on the order of millimeters, and a different approach is required to attain the necessary modulation wavelength.

The solution to obtain a modulation wavelength on a sub-millimeter fashion relying on millimeter waves is obtained by an artificial transmission line: a set of transmission lines out-of-phase from each other is used as a voltage supply, and they feed alternately sections of a doped waveguide which have pn and np junctions. The voltage changes the length of the depletion region of the junctions, modulating the refractive index and imparting a traveling wave modulation.

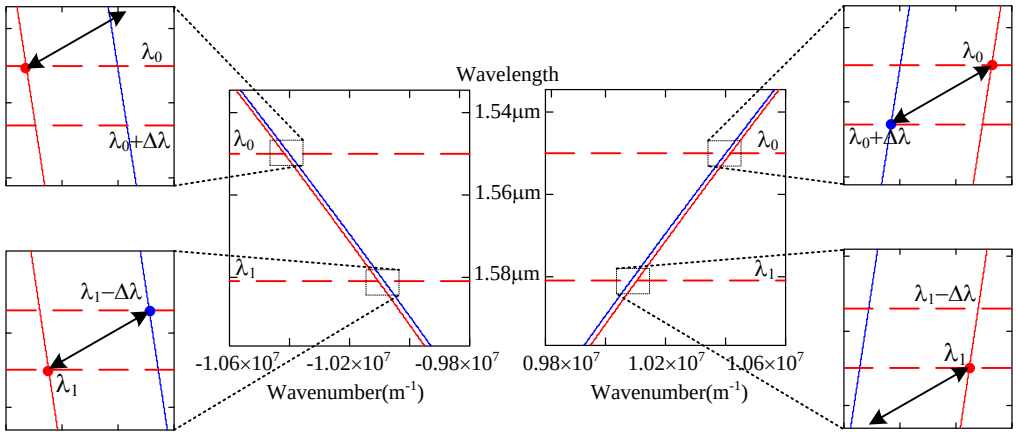

Figure 5.7: Example of dispersion relation of two parallel silicon structures. Conversion can be attained with modulation on the order of tens of gigahertz, and modulation wavelength on the order or hundreds of micrometers.

This arrangement provides a stepwise sinusoidal modulation, with wavelength only depending on the dimensions of the pn and np sections.

In this section we first analyze the effects of the discretization on the amplitude of the harmonic responsible for the mode conversion. Then, for a sinusoid discretized in four parts, we show that a traveling wave component propagating backwards starts to be formed if there is phase error for signals in quadrature. In the sequence, we derive the equations for the refractive index change of a pn junction in reverse bias. Then we analyze the capacitance of pn-np and np-pn junctions, which is the topology we use in the isolator. Next we provide discuss the effects of a periodically loaded transmission line on the attenuation of the electrical signal. We verify that the load impedance needs to be purely real to avoid attenuation, which means that an inductor in parallel to the capacitors is required for good operation of the isolator. Finally we present the parameters chosen for the inductor fabricated and, for the parameters used in the design, we plot the impedance of the overall load (pn-np junctions, inductor and feed-

ing stub) as a function of the frequency.

5.3.1 Effects of Discretization

A discretized modulation pattern certainly generates many harmonics, and the intensity of the fundamental component is therefore reduced. Here we calculate the intensity of each harmonic as a function of the number of discrete steps forming the modulation.

Consider a discretized modulation pattern for the permittivity given by:

$$\Delta\varepsilon\left(t,z\right)=\delta\varepsilon\cos\left[floor\left(\frac{z}{d_{\,\mathrm{mod}}}\right)\varphi_{TL}-\omega t\right] \tag{5.24}$$

where φ_{TL} is the phase of the transmission line feeding a given junction of length d_{mod}. For simplicity, lets normalize it as:

$$g\left(x\right)=\cos\left[floor\left(\frac{x}{L}m\right)\cdot\frac{2\pi}{m}+\varphi_{t}\right] \tag{5.25}$$

Where L is the length of a complete discrete sinusoid, and m is the number of discrete steps the sinusoid is devided. We observe that the phase of each transmission line, φ_{TL} is then a fraction of 2π. We can expand it in a Fourier series:

$$g(x)=\sum_{n=-\infty}^{\infty}G_{n}e^{\imath 2\pi nx/L} \tag{5.26}$$

with

$$G_{n}=\frac{1}{L}\int_{0}^{L}g(x)e^{-\imath 2\pi nx/L}dx \tag{5.27}$$

Solving for the coefficients G_n we obtain

$$G_{n}=\frac{1}{m}\sum_{k=0}^{m-1}\cos\left(2\pi\frac{k}{m}+\phi_{t}\right)e^{-\imath 2\pi nk/m} \tag{5.28}$$

We observe that the terms n and $-n$ can be put together to obtain purely real coefficients. Defining

$$h(x, \phi_t, n) = G_n e^{\imath 2\pi n x/l} + G_{-n} e^{-\imath 2\pi n x/l} \tag{5.29}$$

The final result is

$$h(x, \phi_t, n) = \text{sinc}\left(\frac{\pi n}{m}\right) \left\{ \begin{array}{r} \cos\left(\phi_t - \frac{2\pi n}{L} x\right) \cdot \left| \begin{array}{l} 1 \text{ if } \frac{n+1}{m} \in \mathbb{N} \\ 0 \text{ if } \frac{n+1}{m} \notin \mathbb{N} \end{array} \right. + \\ + \cos\left(\phi_t + \frac{2\pi n}{L} x\right) \cdot \left| \begin{array}{l} 1 \text{ if } \frac{n-1}{m} \in \mathbb{N} \\ 0 \text{ if } \frac{n-1}{m} \notin \mathbb{N} \end{array} \right. \end{array} \right\} \tag{5.30}$$

where the forward and backward propagation components are explicitly obtained. The first harmonic component of the modulation has the amplitude

$$\text{sinc}\left(\frac{\pi}{m}\right) \tag{5.31}$$

We observe is that a 2-step discretization has first harmonic propagating in both directions, which means that it cannot be used for the isolator design. For a 4-step discretization, there is only forward propagation of the first harmonic in which is present 90% of the signal.

5.3.2 Effects of Delay Mismatch

The design we have chosen discretizes the sinusoidal modulation in four parts. This choice is very practical: using pn-np and np-pn junctions, the same transmission line makes the junctions respond 180°out of phase from each other. Therefore, we only need two transmission lines with 90°delay to provide the four-steps discretization. Here we analyze the effects caused by an error $\delta\phi$ for the phase.

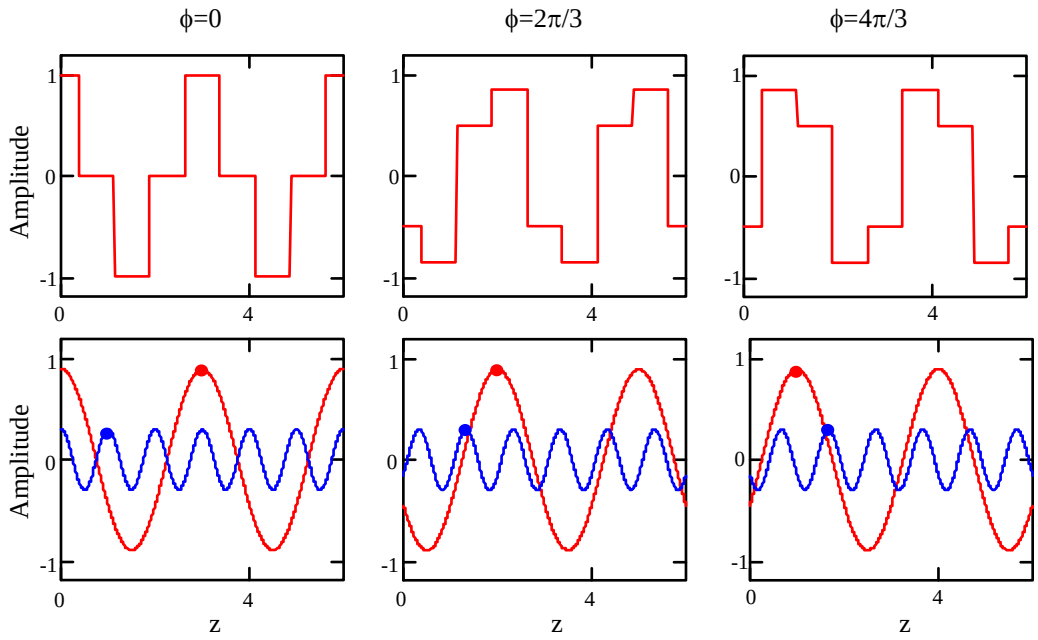

Figure 5.8: Depiction of the discretized traveling wave (blue) used for modulation. Calculation shows that most of the signal (90%) is present on the first harmonic (red), which has the k-vector used for enabling the optical mode conversion. We notice that first harmonic propagates in the backward direction while the third harmonic (blue) propagates in the forward direction.

The discretized signal is given by:

$$g(x) = \begin{cases} \sin(\omega t) & \text{if } 0 \leqslant x < L/4 \\ \cos(\omega t + \delta\phi) & \text{if } L/4 \leqslant x < L/2 \\ -\sin(\omega t) & \text{if } L/2 \leqslant x < 3L/4 \\ -\cos(\omega t + \delta\phi) & \text{if } 3L/4 \leqslant x < L \end{cases} \tag{5.32}$$

where $\delta\phi$ is the phase error for the transmission line in quadrature. After calculating the coefficients of the Fourier series we obtain

$$g(x) = \sum_{m=0}^{\infty} \frac{2}{(2m+1)\pi} \left\{ [\sin(\omega t) + cos(\omega t + \delta\phi)] \sin\left[2\pi(2m+1)\frac{x}{L}\right] \right.$$
$$\left. -(-1)^m [\sin(\omega t) - \cos(\omega t + \delta\phi)] \cos\left[2\pi(2m+1)\frac{x}{L}\right] \right\} \tag{5.33}$$

The only relevant term is the first harmonic ($m = 0$), since the other harmonics do not provide phase matching. Rearranging the terms it is possible to separate it in two parts: a forward propagating and a backward propagating wave. It is given by:

$$g_{1fw}(x,t) = \frac{1}{\pi}\{[1+\cos(\delta\phi)+\sin(\delta\phi)]\cos(\omega t + kx) + [1+cos(\delta\phi)-\sin(\delta\phi)]\sin(\omega t + kx)\} \quad (5.34)$$

$$g_{1bw}(x,t) = -\frac{1}{\pi}\{[1-\cos(\delta\phi)+\sin(\delta\phi)]\cos(\omega t - kx) + [-1+cos(\delta\phi)+\sin(\delta\phi)]\sin(\omega t - kx)\} \quad (5.35)$$

with

$$k = \frac{2\pi}{L} \quad (5.36)$$

Therefore, the amplitude of the forward and backward propagating harmonics are:

$$\frac{\sqrt{[1+\cos(\delta\phi)+\sin(\delta\phi)]^2+[1+\cos(\delta\phi)-\sin(\delta\phi)]^2}}{\pi} = \frac{2}{\pi}\sqrt{1+cos(\delta\phi)} \quad (5.37a)$$

$$\frac{\sqrt{[1-\cos(\delta\phi)+\sin(\delta\phi)]^2+[-1+\cos(\delta\phi)+\sin(\delta\phi)]^2}}{\pi} = \frac{2}{\pi}\sqrt{1-cos(\delta\phi)} \quad (5.37b)$$

We observe that any mismatch $\delta\phi$ decreases the efficiency of conversion from one mode to the other in the isolator and causes an increase in the insertion loss caused by conversion in the direction which no conversion should happen.

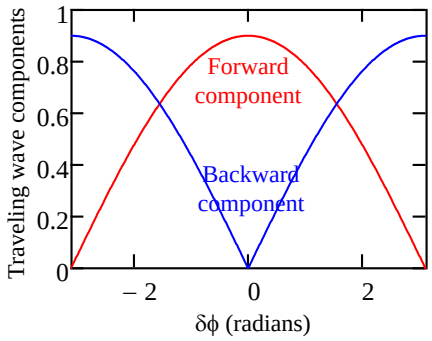

Figure 5.9: Forward (red) and backward (blue) components of the traveling wave generated by 4 discrete steps considering an error $\delta\phi$ for the feeding lines in quadrature ($\pi/2$ and $3\pi/2$ delayed lines).

5.3.3 Depletion Region, Index Change and Figure of Merit

We dope waveguides and modulate the depletion region to change the index of refraction of the waveguides. There are three variables to optimize in the process: the concentration of the dopants (p and n) and the positioning of depletion region formed by them. Besides the modulation achieved by changing the width of the depletion region, the presence of free-carriers also induces loss. In order to optimize the tradeoffs involved, an interesting figure of merit is the ratio between index change and loss. Here we describe the steps to obtain the figure of merit and optimize the design.

First, for a abrupt junction, the length of the depletion region at the p-doped and n-doped regions are, respectively [16]:

$$x_p(V_a) = \sqrt{\frac{2\varepsilon_s}{q}\frac{1}{N_a + N_d}}\sqrt{\frac{N_d}{N_a}}\sqrt{\phi_i - V_a} \tag{5.38a}$$

$$x_n(V_a) = \sqrt{\frac{2\varepsilon_s}{q}\frac{1}{N_a + N_d}}\sqrt{\frac{N_a}{N_d}}\sqrt{\phi_i - V_a} \tag{5.38b}$$

with

$$\phi_i = V_t \ln\left(\frac{N_d N_a}{n_i^2}\right) \tag{5.39}$$

The change in the index of refraction and the added optical losses in a doped silicon waveguide are given by [8]:

$$\Delta n_{Si} = -8.8 \times 10^{-22} N_d - -8.5 \times 10^{-18} N_h^{0.8} \tag{5.40a}$$

$$\Delta\alpha = 6 \times 10^{-18} N_a + 8.8 \times 10^{-18} N_d \tag{5.40b}$$

We are interested in the difference of refraction index and losses between a peak applied voltage and no voltage. We need to consider on our calculation the mode profile as well, which can be obtained as described in Chapter 1. After some algebraic manipulation, we obtain the following expressions for refractive index change and added losses:

$$\begin{aligned}\Delta n = &-8.8 \times 10^{-22} N_d \left[\frac{1}{n_h^{2\sigma}} \frac{C_{even}}{\kappa_{h.even}}\right] \left[\frac{\sin(j_{center} - x_n)}{\cos(\kappa_{h.even} w/2)} - \frac{\sin(\kappa_{h.even} w/2)}{\cos(\kappa_{h.even} w/2)}\right] + \\ &- 8.5 \times 10^{-18} (N_a)^{0.8} \left[\frac{1}{n_h^{2\sigma}} \frac{C_{even}}{\kappa_{h.even}}\right] \left[\frac{\sin[\kappa_{h.even}(j_{center} + x_p)]}{\cos(\kappa_{h.even} w/2)} - \frac{\sin(\kappa_{h.even} j_{center})}{\cos(\kappa_{h.even} w/2)}\right]\end{aligned} \tag{5.41}$$

$$\begin{aligned}\Delta\alpha = &-8.8 \times 10^{-18} N_d \left[\frac{1}{n_h^{2\sigma}} \frac{C_{even}}{\kappa_{h.even}}\right] \left[\frac{\sin(j_{center} - x_n)}{\cos(\kappa_{h.even} w/2)} - \frac{\sin(\kappa_{h.even} w/2)}{\cos(\kappa_{h.even} w/2)}\right] + \\ &- 6.0 \times 10^{-18} N_a \left[\frac{1}{n_h^{2\sigma}} \frac{C_{even}}{\kappa_{h.even}}\right] \left[\frac{\sin[\kappa_{h.even}(j_{center} + x_p)]}{\cos(\kappa_{h.even} w/2)} - \frac{\sin(\kappa_{h.even} j_{center})}{\cos(\kappa_{h.even} w/2)}\right]\end{aligned} \tag{5.42}$$

with

$$C_{even} = \left(\int_{\infty}^{\infty} E_{even} dx\right)^{-1} \tag{5.43}$$

Finally, the figure of merit can be obtained as

$$fom = \frac{10 \log(e) \Delta\alpha + \alpha_0}{\Delta n} \tag{5.44}$$

Where α_0 is the intrinsic loss of the waveguide.

We use the equations above to obtain the dopant concentration and offset which minimizes fom. We obtain, for a silicon waveguide with 250 nm $\times$ 450 nm cross-section, a n-dopant concentration of 1×10^{18} cm^{-3}, a p-dopant concentration of 1×10^{17} cm^{-3}, with the center of the dopants shifted 202 nm – the p-dopant overlaps most of the waveguide. Figure 5.10 shows the change in permittivity for such configuration when a -6 V voltage is applied to the junction.

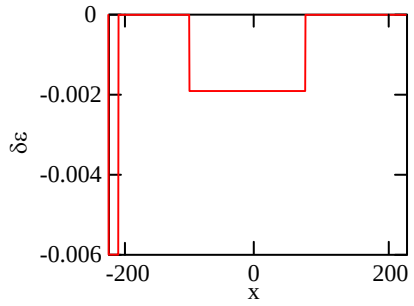

Figure 5.10: Change in permittivity when -6 V is applied to the pn junction.

5.3.4 pn-np/np-pn Capacitance

A pn junction has a voltage dependent capacitance. Considering a linearized model, we have

$$C_{left}(V_1) = C_0 \frac{1}{1 + \frac{\alpha V_1}{d_0}} \tag{5.45a}$$

$$C_{right}(V_2) = C_0 \frac{1}{1 - \frac{\alpha V_2}{d_0}} \tag{5.45b}$$

where C_0 is the capacitance of the diode without voltage applied, and α is the change in the length of the depletion region per Volt applied. For the model shown in Fig. 5.11 we obtain

$$V_1 = \frac{(V_{in} 2\alpha - 2d_0) + \sqrt{(V_{in} 2\alpha - 2d_0)^2 + 8\alpha d_0 V_{in}}}{4\alpha} \tag{5.46}$$

and

$$V_2 = V_{in} - V_1 \tag{5.47}$$

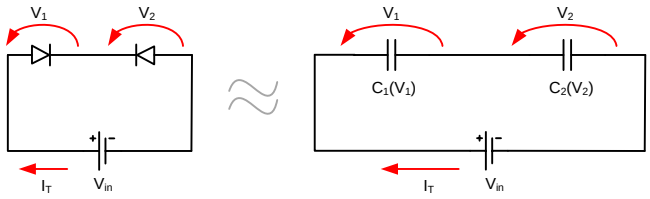

Figure 5.11: Model for a capacitor made of two junctions, in a npn or pnp configuration.

Figure 5.12 shows the change in capacitance as a function of the input voltage V_{in} of a np-pn capacitor.

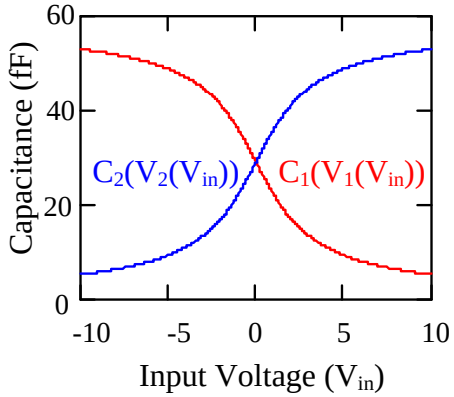

Figure 5.12: Capacitance C_{left} and C_{right} as a function of the input voltage V_{in}.

We calculate C_0 plugging real dimensions of the device in the equation:

$$C_0 = \frac{\varepsilon_0 \varepsilon_r l_{diode} h_{diode}}{d_{depletion}} \tag{5.48}$$

where ε_r is the relative permittivity of Si (11.7), l_{diode} is the length of the diode (112.5 nm), h_{diode} is the height of the diode (250 nm), and $d_{depletion}$ is the length of

the depletion region without voltage applied to the device. It gives $C_0 = 29.1fF$. The parameter α is obtained from simulations using the software Atlas®, from Silvaco®, and we obtain $\alpha = 50nm/V$.

The effective capacitance can be obtained as:

$$C_{eq}(V_{in}) = \frac{C_{left}(V_1(V_{in}))C_{right}(V_{in} - V_1(V_{in}))}{C_{left}(V_1(V_{in})) + C_{right}(V_{in} - V_1(V_{in}))} \tag{5.49}$$

The left side of Fig. 5.13 shows voltage across each of the capacitors in a np-pn device as a function of an AC input signal, and the right side of Fig. 5.13 shows the change in the equivalent capacitance C_{eq} as a function of an AC input signal.

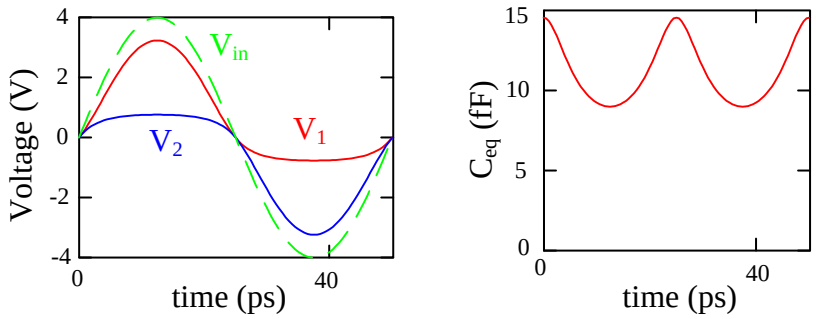

Figure 5.13: In the left we have a 20 GHz signal with peak voltage of 4 V being applied on a np-pn junction (green). The voltage across the np junction is shown in red, and the voltage across the pn junction in shown in blue. In the right we have the change in the equivalent capacitance for when such AC signal is applied.

5.3.5 Periodically Loaded Transmission Line

As a first approximation, a transmission line which is loaded periodically with a reactive impedance can have its reactance lumped in the characteristic impedance of the line

$$Z_0' = \sqrt{\frac{L_0}{C_0 + C_L}} \tag{5.50}$$

where L_0 is the inductance per unit length, C_0 is the capacitance per unit length, and C_L is the load capacitance normalized by the distance between two loads. This model is enough in the case when the load capacitance is small compared to the capacitance of the transmission line. Unfortunately, it is not the case for our design.

In order to properly model the transmission behavior of a periodic transmission line, we recur to ABCD matrix, which makes it easy to compute the impedance and attenuation of a network composed of cascaded elements. The theory regarding ABCD matrix is shown in Appendix A for completeness of the design, providing a compilation of the treatment described in [21].

By applying the ABCD matrix to our design parameter we observe that the periodically loaded transmission line has a cut-off, which attenuates the the propagation the electrical signal and depends on the load impedance. Calculations were performed considering the following parameters: the main transmission line has an of 110 Ω impedance, the capacitance of the pn-np diodes is 14 fF, contact resistance of the diodes, considering the dopants concentration and ohmic contact described in Section 5.5 is 50 Ω, the stub connecting the load to the main transmisison line is 125 µm long with impedance of 60 Ω. We obtained a theoretical attenuation of 20 dB for the case of 32 diodes loading the main transmission line. The equations for the design of the main transmission

line and of the stub are compiled and presented in Appendix B.

The way to reduce the attenuation caused by the load is by reducing the reactive impedance as seen from the transmisison line, which is achieved by adding an inductor in parallel to the capacitive pn-np/np-pn junctions. Theoretically, in resonance the attenuation is completely suppressed, and progressively increases as we operate further from the resonance.

5.3.6 Overall Impedance of the Load

An inductor is required to reduce the strong attenuation caused by the reactive part of the periodic capacitive load. The model used for the the design is shown in Appendix C.

The resonance of the LC tank is obtained by adding the diode capacitance to the inductor's capacitances in Eq. C.16. The overall impedance, considering how the transmission line sees the LC circuit, the resistance of the vias and highly doped silicon, and the piece of transmission line feeding it is given by:

$$Z_{in} = Z_{ltstub}\frac{Z_L + \imath Z_{ltstub}\tan\left(\frac{\omega_0}{c_0}n_{stub}l_{stub}\right)}{Z_{ltstub} + \imath Z_L\tan\left(\frac{\omega_0}{c_0}n_{stub}l_{stub}\right)} \tag{5.51}$$

Where

$$Z_L = \left(\frac{1}{\imath\omega C_d} + R_d\right)||Z_{ind}, \tag{5.52}$$

Z_L is the impedance of the load made of the pn-np (or np-pn) junction and the inductor in parallel, Z_{ltstub} is the impedance of the stub connecting the transmission line to the load, n_{stub} is the effective index of the stub, l_{stub} is length of the stub, R_d is the contact resistance for the connection between the stub and

the highly doped silicon slab, and C_d is the capacitance of the pn-np (or np-pn) junction.

A plot of the LC-circuit impedance (Z_L) and the overall impedance as seen from the transmission line (Z_{in}), with a 125-μm long stub, is shown in Fig. 5.14. The inductor impedance is calculated to be $Z_{ind} = 63 + \imath 278\,\Omega$ at 20 GHz for a 1.84 nH spiral. It was designed to be 1.5-mm long, with a spiral made of of 5.5 turns, with aluminum lines 2-μ wide, with distance between lines of 3-μm and external diameter of 85 μm. Other material parameters are extracted from [83].

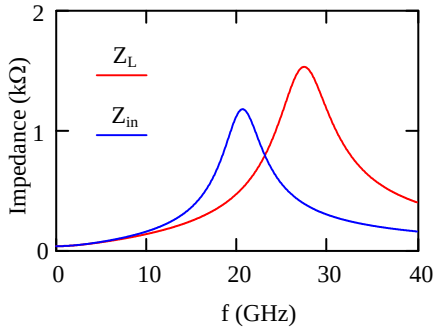

Figure 5.14: Impedance of the LC load (Z_L) and of the LC load as seen from the transmission line when connected by a 125-μm stub (Z_{in} as a function of frequency.

5.4 Design Summary

In this section we briefly summarize the insights brought by the electrical design and present the choices of design parameters used for the device fabricated.

We design the electrical elements embedded in the waveguide to obtain the required traveling wave for the optical mode conversion. In order to realize experimentally the isolator and account for the typical modulation speed that

can be achieved in silicon (typically in the GHz range [9, 39]) the modulation wavelength and the required length of the waveguide for total conversion are therefore scaled up relative to the ones simulated in Fig. 5.2. The traveling wave is designed to operate at a frequency of 10 GHz which correspond to the difference in frequency between the two modes for the waveguide shown in Fig. 5.2. The proper modulation wavelength is achieved experimentally by discretizing the electrical wavelength and using two transmission-lines with a $\pi/2$ phase difference as shown in Figs. 5.15 and 5.16, connected in an alternated way to a series of pn-np and np-pn junctions. When the traveling wave propagates, the depletion region length is changed (inducing an index change) in only one of the parallel diodes (the one experiencing a reverse-bias voltage) fulfilling the required non-zero overlap condition. The electrical structure was designed to induce a periodicity in the index modulation of 450 μm, which means that the modulation wavelength λ_m achieves the design requirements independent of the wavelength of the electrical signal $\lambda_{Electrical}$ (which is around 10 mm for a 10 GHz signal – see e.g. Fig. 5.17 where we show the expected voltage on each modulation section for a 10 GHz travelling wave and a 166 μm diode length). In order to prevent the periodically-loaded transmission lines from having a cut-off below the desired modulation frequency we add spiral inductors in parallel with the pn-np and np-pn junctions to the waveguide (with a total length 1.5 mm corresponding to an inductance L ≈ 1.84 nH). The length of the stub connecting the capacitors and inductors to the transmission line also matter for the cut-frequency, and from design we expect that a 100-μm long stub would push the cut-off about 20 GHz. From calculations, the adequate wavenumber required for conversion leads to 110-μm long diodes, separated by a 2-μm wide region with the opposite dopant to provide electrical insolation. The overall

number of discrete modulation full waves was 22, i.e. 88 modulation sections, or 166 diodes. The optimum distribution for the dopant pattern was calculated to be with n-doped regions of $1 \times 10^{18}\text{cm}^{-3}$ and p-doped regions of $1 \times 10^{17}\text{cm}^{-3}$ concentrations, with the center of the dopant region shifted about 190 nm from the center of the waveguides, so that losses are minimized for the index change required of the device. The dopants distribution across the cross section of the waveguide is shown in the inset of the Fig. 5.16.

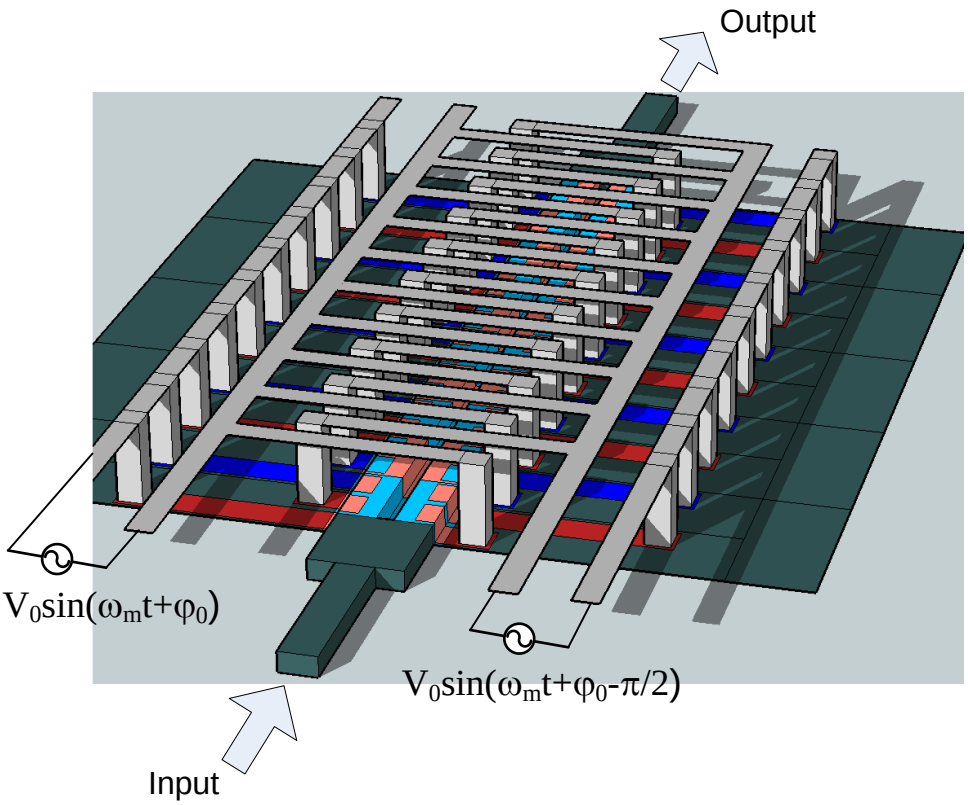

Figure 5.15: Simplified schematics of the device. Undoped silicon is in green, lightly p-doped silicon in light blue, lightly n-doped silicon in rose, heavily p-doped silicon in dark blue, heavily n-doped silicon in red, vias and electrical wiring in gray.

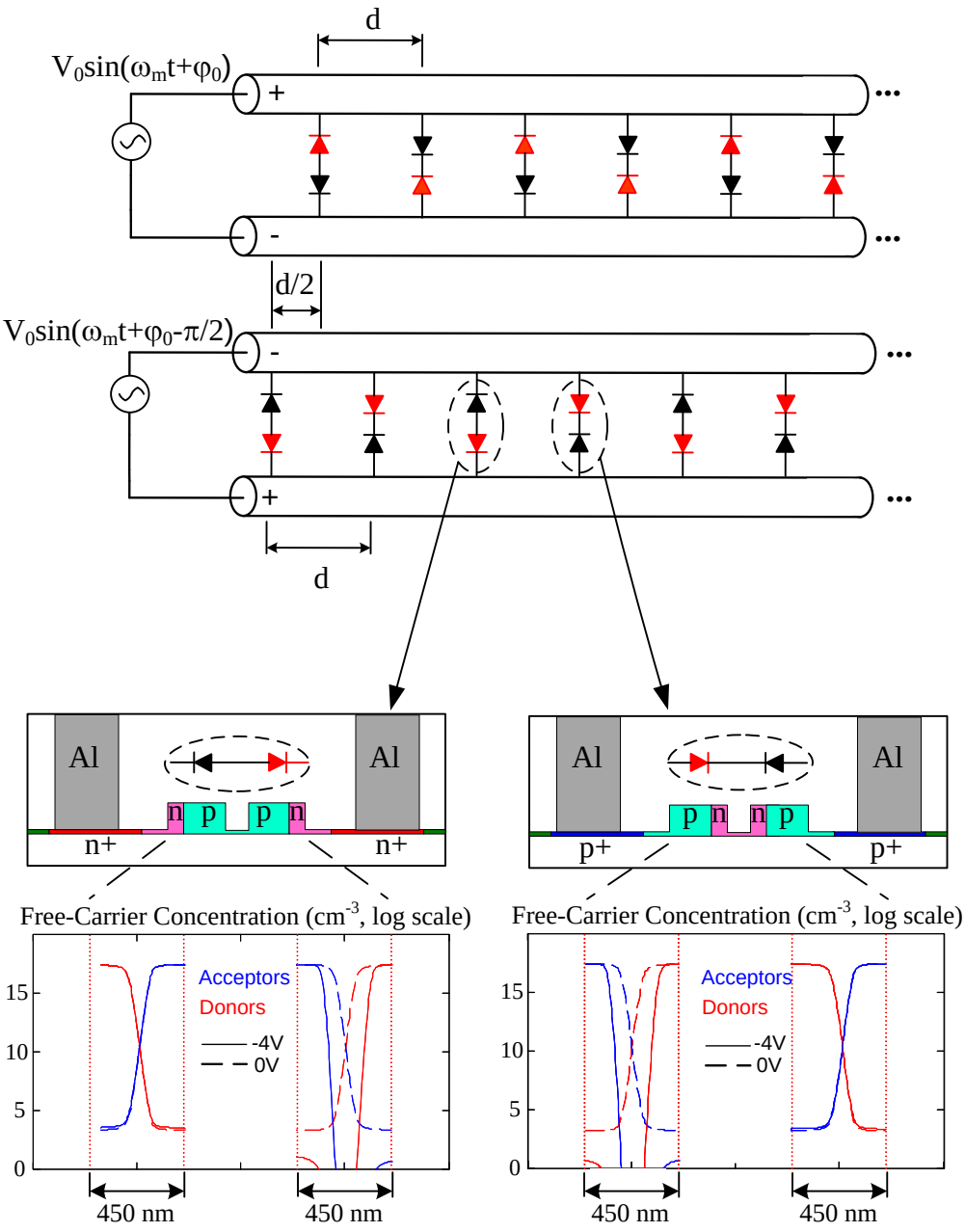

Figure 5.16: Schematics of the two transmission lines feeding pn-np and np-pn junctions. A depiction of the voltage across the transmission lines is shown in dotted blue and red lines, and the reversely-biased diodes are highlighted in red.

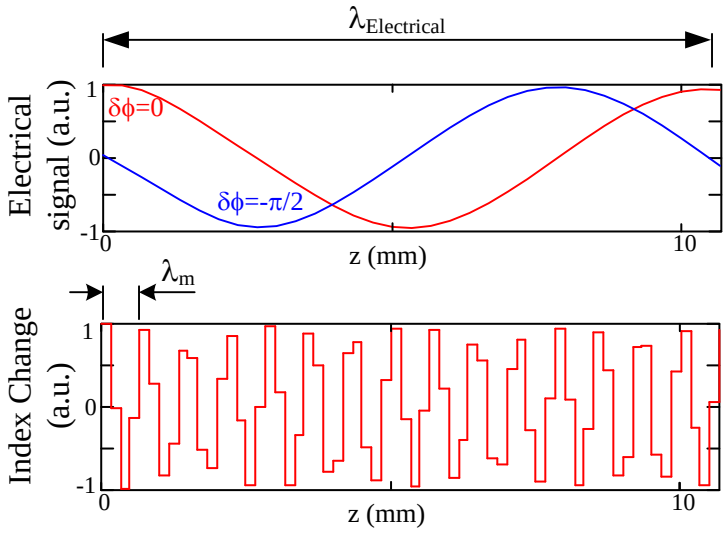

Figure 5.17: Electrical signal across the transmission line and effective index change obtained by the reversely-biased diodes. The diodes are interleaved in such a way that the modulation wavelength λ_m is set independently of the electrical wavelength $\lambda_{Electrical}$.

5.5 Fabrication

We fabricate the device on a SOI platform in a completely CMOS-compatible process. The PMMA photoresist masks for the dopants are written using e-beam lithography, followed by implantation of B^+ with $1 \times 10^{17}cm^{-3}$ concentration and the P^- with $1 \times 10^{18}cm^{-3}$ concentration. Masks for highly doped regions are written as well, followed by implantation of $1 \times 10^{20}cm^{-3}$ of BF_2^+ and Ar^- to form low resistance region for accessing the p and n regions, respectively, for electrical contacts. Next we write a maN-2403 photoresist mask with the waveguide pattern using e-beam lithography, and etched the silicon down 215 nm, leaving a thin 35-nm slab everywhere. The dopants are then activated on anneal furnace and RTA process, followed by cladding the waveguides with a 1-µm thick SiO_2 deposited with PECVD tool. We then write the mask for vias

and inductors, etching through the SiO_2 and sputtering 100 nm of $MoSi_2$ for low contact resistance and 600 nm of AlCuSi. Another cladding layer is deposited, 600-nm thick, and a second set of vias are etched. Finally, we write the mask for lift-off of a 1500 nm deposition of AlCuSi to fill up the vias and form the transmission lines. In Fig. 5.18 we show a general picture of the isolator, where transmission lines and delay lines can be seen. We use a ground-signal-ground transmission line, which is split in two and a $\pi/2$ delay is provided to one of the lines. This approach allows that a single signal generator is used to feed the overall structure.

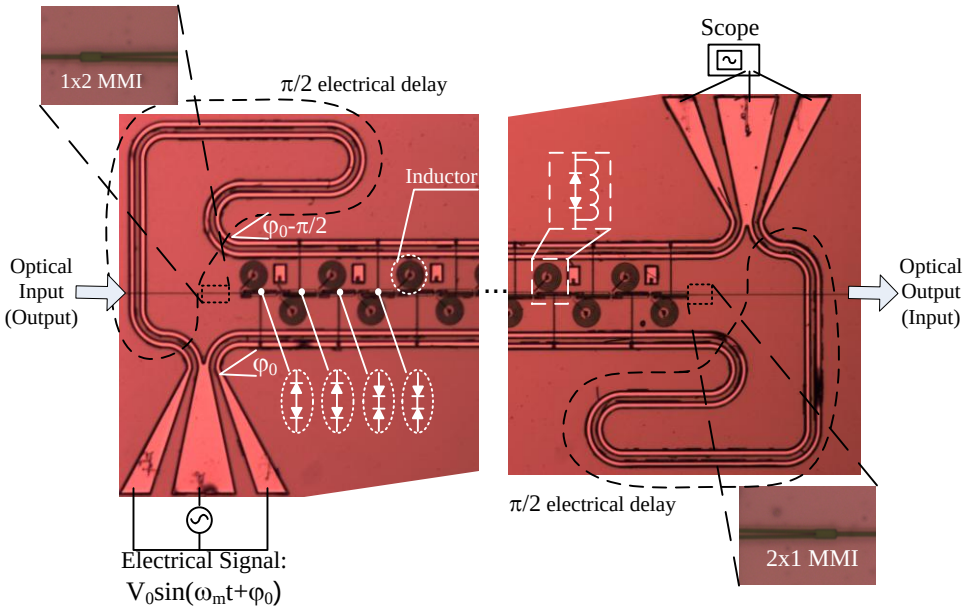

Figure 5.18: Electrically-driven optical-isolator.

In the left side of Fig. 5.19 we show an image of the electrical elements of the isolator (top) and of the optical elements (bottom) of the fabricated device. The insets point out to the inductors we place in parallel to the diodes, and to the vias which contact the pn-np diodes.

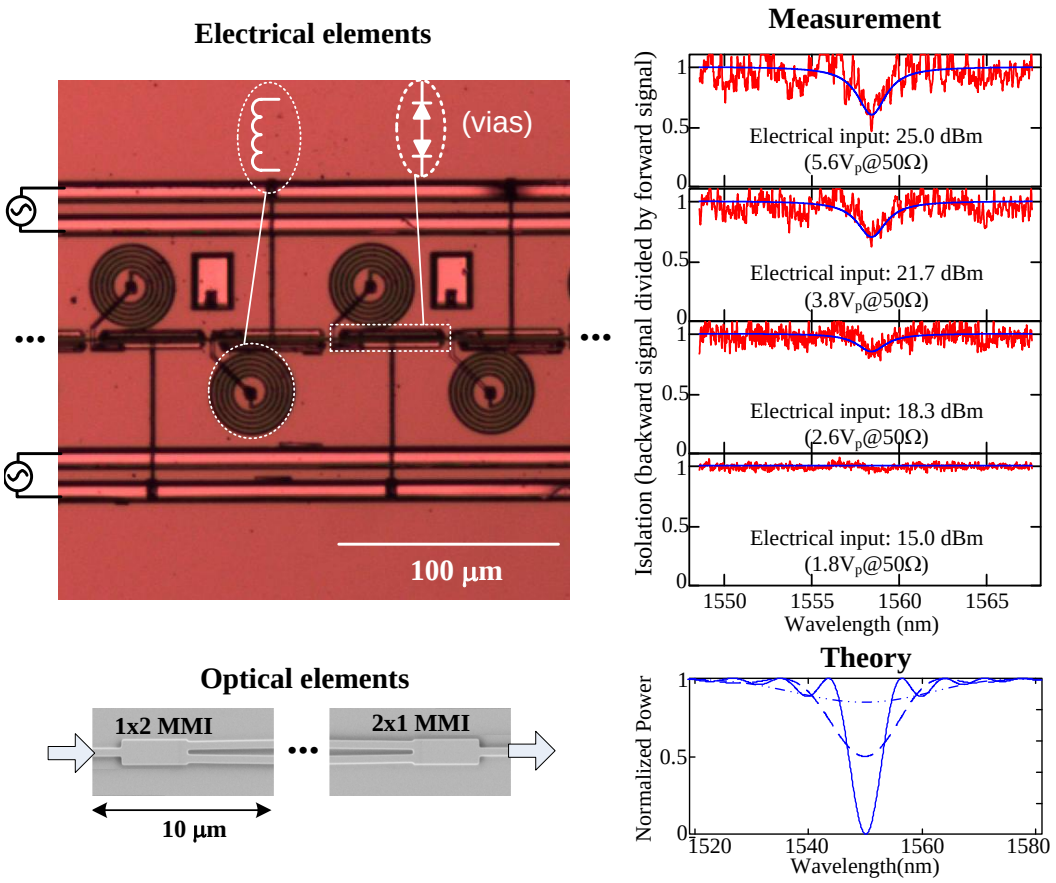

Figure 5.19: In the left we show the electrical elements (top) and optical elements (bottom) of the electrically-driven optical-isolator. In the top right we show isolation as a function of electrical signal input power. We observe up to 3 dB isolation with a electrical input of 25 dBm, and smaller values as the input decreases. The blue line provides a guide to the eye. In the bottom right we have the theoretical bandwidth of conversion, obtained from the dispersion relation of the two modes using Effective Index Method.

5.6 Measurements

We measured up to 3 dB isolation when operating at a wavelength of 1558 nm. This isolation is halfway from the total mode conversion obtained from simulation. This is due limitations with our electrical signal power supply, which can achieve a maximum 25 dBm output power (or 5.6 V_p for 50 Ω impedance). The measurement is performed by applying a CW electrical signal and sweeping the laser wavelength. We measure the transmission spectra for both light going through the device from one direction and from another by swapping the input and output fibers. The right side of Fig. 5.19 shows the ratio between the two measured transmission spectra. The wavelength dependency is due to the dispersion in the waveguide (i.e. a dependence of the wavenumber difference between the modes on wavelength). For comparison we show in the bottom right of Fig. 5.19 the simulated relative transmission using the mode conversion equations and considering the dispersion of the waveguide to determine the bandwidth. Geometry variation of the waveguide caused by the fabrication process reduces the bandwidth of the device fabricated. One can see that the results agree well with the expected performance of the device.

5.7 Conclusion

The isolator shown here is key for future photonic systems on chip. The isolation degree, insertion loss, bandwidth and power efficiency of the device in principle can be increased using appropriate waveguide and electrical elements design and fabrication. The amount of isolation can be increased by having better impedance match and higher input power for the electrical signal. The

dopants in the diodes are expected to induce loss on the order of 16 dB for a 1.0 cm device. This loss is not fundamental and can be decreased by using alternative pn-junction schemes, which also reduce the power consumption and increase the isolation attained [84]. The bandwidth of operation depends on how parallel the dispersion relations for the symmetric and anti-symmetric waveguides, which can be engineered by changing dimensions and geometry of the waveguides. The bandwidth of the device can be increased as well by better etching processes and height characterization of the SOI wafer. From simulation we observe that every nanometer change in the thickness of the silicon slab offsets the matched wavelength about 3 nm, while every nanometer change in the height offsets the center of the bandwidth about 1.6 nm. Simply by mapping and changing the length of the diodes accordingly would provide the required modulation wavenumber and therefore a better isolation. From our measurements, we observed up to 3 nm variation in the slab thickness throughout the fabricated devices.

APPENDIX A

ABCD MATRIX FOR A PERIODICALLY LOADED TRANSMISSION LINE

The ABCD matrix relates output to input of a two-port element as:

$$\begin{pmatrix} V_1 \\ I_1 \end{pmatrix} = \begin{pmatrix} A & B \\ C & D \end{pmatrix} \begin{pmatrix} V_2 \\ -I_2 \end{pmatrix} \tag{A.1}$$

Where V_1 and I_1 are the voltage and current of one of the ports and V_2 and I_2 are the voltage and current of the other port.

For two cascaded elements, as shown in Fig. A.1, we obtain:

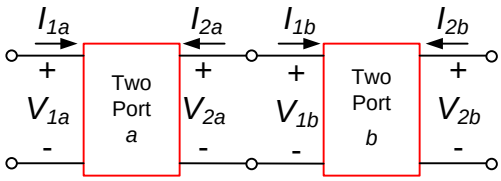

Figure A.1: Two cascaded two port elements.

$$\begin{pmatrix} V_{1a} \\ I_{1a} \end{pmatrix} = \begin{pmatrix} A_a & B_a \\ C_a & D_a \end{pmatrix} \begin{pmatrix} A_b & B_b \\ C_b & D_b \end{pmatrix} \begin{pmatrix} V_{2b} \\ -I_{2b} \end{pmatrix} \tag{A.2}$$

For shunt admittance loading a transmission line in its middle, as shown in Fig. A.2, we have:

$$\begin{pmatrix} A_{tm} & B_{tm} \\ C_{tm} & D_{tm} \end{pmatrix} = \begin{pmatrix} \cosh\left(\frac{\gamma l}{2}\right) & Z_0 \sinh\left(\frac{\gamma l}{2}\right) \\ Y_0 \sinh\left(\frac{\gamma l}{2}\right) & \cosh\left(\frac{\gamma l}{2}\right) \end{pmatrix} \begin{pmatrix} 1 & 0 \\ Y & 1 \end{pmatrix} \begin{pmatrix} \cosh\left(\frac{\gamma l}{2}\right) & Z_0 \sinh\left(\frac{\gamma l}{2}\right) \\ Y_0 \sinh\left(\frac{\gamma l}{2}\right) & \cosh\left(\frac{\gamma l}{2}\right) \end{pmatrix} \tag{A.3}$$

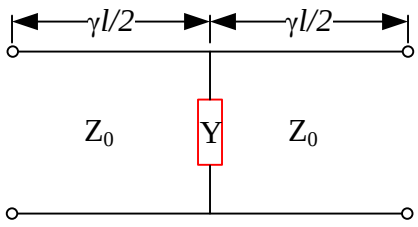

Figure A.2: Shunt admittance loading transmission line.

Where Z_0 is the impedance of the shunt, Y_0 is the admmitance of the shunt, γ is the propagation constant of the main transmission line, and l is the distance between two shunts of the loading the transmission line. In our case, the shunt is formed by the pn-np junctions in parallel with an inductor and the wires connecting it to the main transmission line.

It leads to:

$$A_{tm} = \cosh\left(\gamma_{tl}\frac{l_{tl}}{2}\right) + \frac{Z_{tl}}{2Z_{in}}\sinh\left(\gamma_{tl}\frac{l_{tl}}{2}\right) \tag{A.4}$$

$$B_{tm} = Z_{tl}\left\{\left(\frac{Z_{tl}}{2Z_{in}}\right)\left[-1+\cosh\left(\gamma_{tl}\frac{l_{tl}}{2}\right)\right] + \sinh\left(\gamma_{tl}\frac{l_{tl}}{2}\right)\right\} \tag{A.5}$$

$$C_{tm} = \frac{1}{Z_{tl}}\left\{\left(\frac{Z_{tl}}{2Z_{in}}\right)\left[1+\cosh\left(\gamma_{tl}\frac{l_{tl}}{2}\right)\right] + \sinh\left(\gamma_{tl}\frac{l_{tl}}{2}\right)\right\} \tag{A.6}$$

$$D_{tm} = A_{tm} \tag{A.7}$$

For a network with N symmetric ($A_{tm} = D_{tm}$) elements, reciprocal ($A_{tm}D_{tm} = B_{tm}C_{tm}$), matched at the end, the overall $ABCD$ matrix is formed by the terms [21]:

$$A = \cosh(N\Gamma_{casc}) \tag{A.8}$$

$$B = Z_c\sinh(N\Gamma_{casc}) \tag{A.9}$$

$$C = \frac{1}{Z_c}\sinh(N\Gamma casc) \tag{A.10}$$

$$D = A \tag{A.11}$$

with

$$\Gamma_{casc} = \text{acosh}\left(\frac{A_{tm} + D_{tm}}{2}\right) \tag{A.12}$$

and

$$Z_{ctm} = \sqrt{\frac{B_{tm}}{C_{tm}}}, \tag{A.13}$$

Where and

$$\gamma_{tl} = \frac{\omega_0}{c_0}\sqrt{\varepsilon_{gs}} \tag{A.14}$$

The attenuation constant is obtained from the imaginary part of the propagation parameter Γ_{casc} multiplied by the number of elements N of the network.

APPENDIX B

ELECTRICAL TRANSMISSION LINES

Three distinct transmission lines are used in this work. Proper dimensions need to take into account the trade-off between impedance and losses. Losses decrease when the dimensions of the transmission line increase, while the impedance increases when the dimensions increase. The equations used for the design are obtained from [85, 86]. We use coplanar strips transmission line

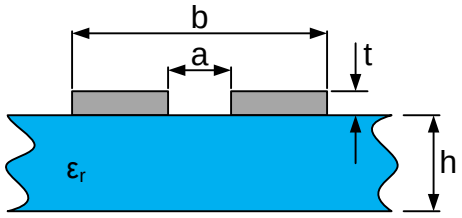

Figure B.1: Coplanar strips.

(Fig. B.1) for feeding the diodes for the electrically-driven optical isolator. The equation for its impedance is given by:

$$Z_0(a,b,h) = \frac{\eta_0}{\sqrt{\varepsilon_{eff}(a,b,h)}} \frac{K(k(a,b))}{K(k'(a,b,h))} \tag{B.1}$$

with

$$\varepsilon_{eff}(a,b,h) = 1 + \frac{\varepsilon_r - 1}{2} \frac{K(k'(a,b,h))}{K(k(a,b))} \frac{K(k_1(a,b,h))}{K(k_1'(a,b,h))} \tag{B.2}$$

and

$$\begin{aligned} k(a,b) &= \frac{a}{b} \\ k'(a,b) &= \sqrt{1-k^2(a,b)} \end{aligned} \tag{B.3}$$

$$\begin{aligned} k_1(a,b,h) &= \frac{sinh(\frac{\pi}{4}\frac{a}{h})}{sinh(\frac{\pi}{4}\frac{b}{h})} \\ k_1'(a,b) &= \sqrt{1-k_1^2(a,b)} \end{aligned} \tag{B.4}$$

and

$$K(k) = \int_0^{\pi/2} \frac{1}{\sqrt{1 - k^2 \sin^2(\theta)}} d\theta \tag{B.5}$$

where a, b and h are the dimensions as shown in Fig. B.1, ε_r is the relative permittivity of the dielectric, and η_0 is the impedance of the free space.

Losses for coplanar strips transmission line (Fig. B.1) are divided in two parts, namely dielectric and conductor losses. For dielectric losses we have (in dB/m):

$$\alpha_d = \frac{20\pi}{ln(10)} \frac{\varepsilon_r}{\sqrt{\varepsilon_{eff}}} \frac{q_0}{\lambda_0} \tan(\delta) \tag{B.6}$$

with

$$q_0 = \frac{\varepsilon - 1}{\varepsilon_r - 1} \tag{B.7}$$

where λ_0 is the free-space wavelength of the electrical signal, and $\tan(\delta)$ is the loss tangent of the dielectric.

For the conductor losses we have(in dB/m):

$$\alpha_c = 17.34 \frac{R_s}{Z_0} \frac{P_p}{\pi a} \frac{a+b}{2a} \frac{\frac{1.25}{\pi} \ln 4\pi \frac{b-a}{2t} + 1 + \frac{2.5t}{\pi(b-a)}}{\left[1 + \frac{b-a}{a} + \frac{1.25t}{\pi a}(1 + \ln 2\pi \frac{b-a}{t})\right]^2} \tag{B.8}$$

with

$$P_p = \begin{cases} \frac{k}{k'^{3/2}(1-k')} \frac{K(k)}{K(k')} & \text{if } 0 < k \leqslant \sqrt{2}/2 \\ \frac{1}{\sqrt{k}(1-k)} & \text{if } \sqrt{2}/2 < k < 1 \end{cases} \tag{B.9}$$

where t is the thickness of the metal, and the Sheet Resistance R_s is given by:

$$R_s = \sqrt{\frac{\omega_0 \mu_0}{2\sigma}} \tag{B.10}$$

where ω_0 is the frequency of the signal (in rad/s), μ_0 is the permissivity of the free space, and σ is the conductivity of the metal. Figure B.2 shows impedance and conductor losses for 1-µm Aluminum transmission lines with silicon as dielectric. From our calculation, dielectric losses are negligible compared to the conductor losses (<10%).

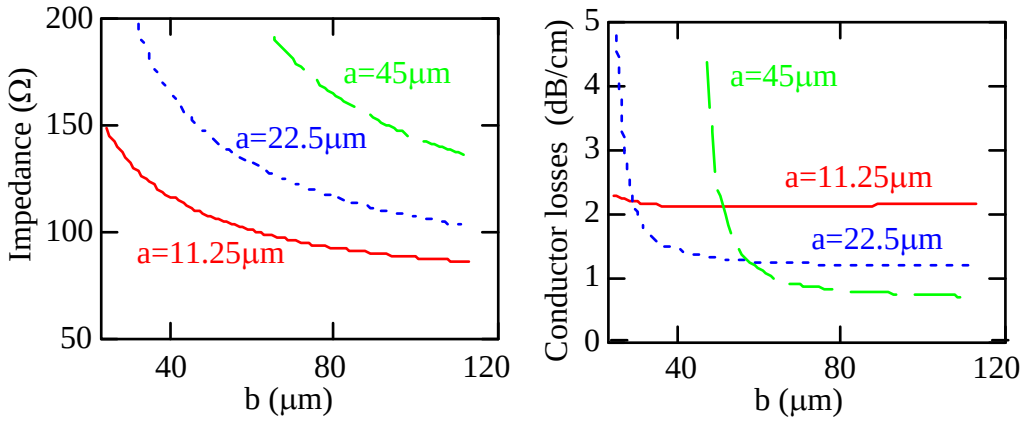

Figure B.2: Impedance (left) and conductor losses (right) for coplanar strip transmission line on a silicon wafer. We use Aluminum 1-μm thick as the metal.

We use three coplanar strips (ground-signal-ground configuration, Fig. B.3) as the input and output for the electical signal of the isolator.

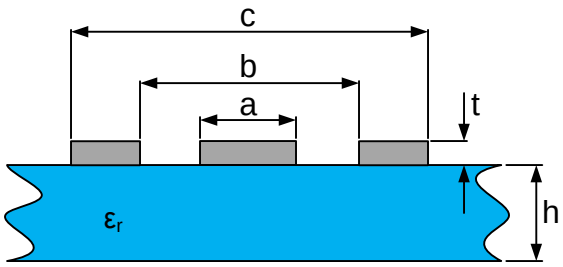

Figure B.3: Three coplanar strips.

Its impedance is given by:

$$Z_{gsg} = \frac{\eta}{4\sqrt{\varepsilon_{gsg}}} \frac{K(k_{gsg})}{K(k'_{gsg})} \tag{B.11}$$

With

$$\varepsilon_{gsg} = 1 + \frac{\varepsilon_r - 1}{2} \frac{K(k'_{gsg1})}{K(k_{gsg1})} \frac{K(k_{gsg})}{K(k'_{gsg})} + \frac{\varepsilon_r - 1}{2} \frac{K(k'_{gsg1})}{K(k_{gsg1})} \left(\frac{K(k_{gsg})}{K(k'_{gsg})} \right)^2 \frac{t}{b-a} + \left(\frac{K(k_{gsg})}{K(k'_{gsg})} \frac{t}{b-a} \right) \quad \text{(B.12)}$$

and

$$k_{gsg} = \frac{c}{b} \sqrt{\frac{b^2 - a^2}{c^2 - a^2}} \quad \text{(B.13a)}$$

$$k'_{gsg} = \sqrt{1 - k_{gsg}^2} \quad \text{(B.13b)}$$

$$k_{gsg1} = \frac{\sinh(\frac{\pi}{4}\frac{b}{h})}{\sinh(\frac{\pi}{4}\frac{b}{h})} \sqrt{\frac{\sinh^2(\frac{\pi}{4}\frac{b}{h}) - \sinh^2(\frac{\pi}{4}\frac{a}{h})}{\sinh^2(\frac{\pi}{4}\frac{c}{h} - \sinh^2(\frac{\pi}{4}\frac{a}{h})}} \quad \text{(B.13c)}$$

$$k'_{gsg1} = \sqrt{1 - k_{gsg1}^2} \quad \text{(B.13d)}$$

Figure B.4 shows impedance for three-coplanar-strips transmission-lines with silicon as dielectric.

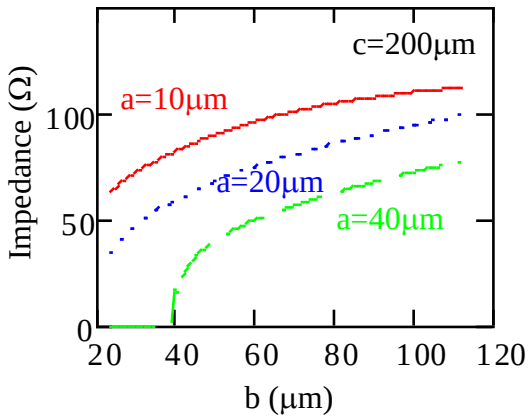

Figure B.4: Impedance of three-coplanar-strip transmission-line on a silicon wafer. We use Aluminum 1-μm thick as the metal.

We use paired strips (Fig. B.5) for connecting the main transmission line to the pn-np and np-np junctions of the isolator.

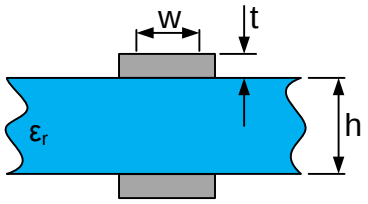

Figure B.5: Paired strips.

Its impedance is given by:

$$Z_{ps} = \frac{\eta_0}{\sqrt{\varepsilon_r}} \begin{cases} \left\{ \frac{w}{h} + \frac{\ln(4)}{\pi} + \frac{\varepsilon_r+1}{2\pi\varepsilon_r} \ln\left[\frac{\pi}{2}\varepsilon\left(\frac{w}{h}+0.94\right)\right] + \frac{\varepsilon_r-1}{2\pi\varepsilon_r^2} \ln\left(\varepsilon_r \frac{\pi^2}{16}\right) \right\}^{-1} & \text{if } 1 \leqslant w/h \\ \frac{1}{\pi}\left\{ \ln\left(\frac{4w}{h}\right) + \frac{1}{8}\left(\frac{w}{h}\right)^2 - \frac{\varepsilon_r-1}{2(\varepsilon+1)}\left[\ln\left(\frac{\pi}{2}\right) + \frac{1}{\varepsilon}\ln\left(\frac{4}{\pi}\right)\right] \right\} & \text{if } w/h < 1 \end{cases} \tag{B.14}$$

Figure B.6 shows impedance for paired-strips transmission-lines with silicon Dioxide as dielectric.

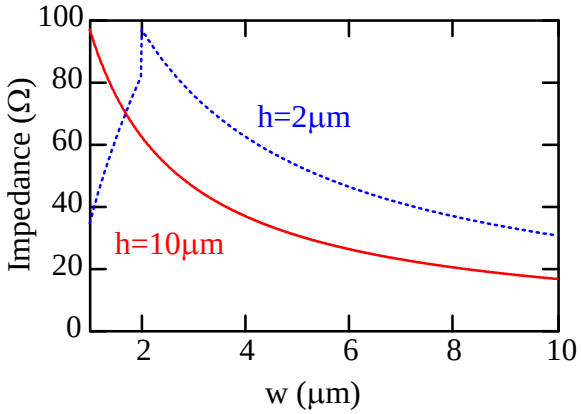

Figure B.6: Impedance of paired-strips transmission-line with silicon Dioxide as dielectric.

APPENDIX C

THIN FILM INDUCTOR

Here we describe the equations for designing a thin-film inductor, modeled as shown in Fig. C.1. A thin-film inductor has the following impedance [83]:

$$Z_{ind} = \left[(\imath\omega L_{spiral} + R_s + R_{eddy})|| \left(\frac{1}{\imath\omega C_p}\right)\right] || \left\{\frac{1}{\imath\omega C_{ox}} + 2\left[R_1|| \left(\frac{1}{\imath\omega C_1}\right)\right]\right\} \tag{C.1}$$

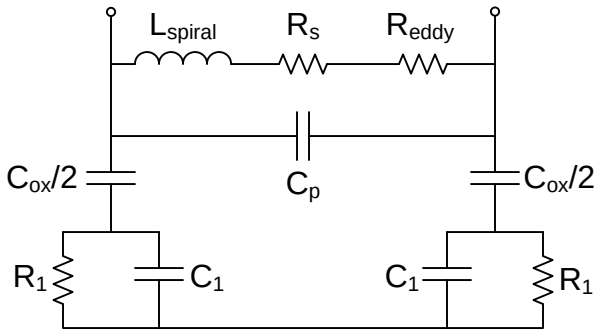

Figure C.1: On-chip spiral-inductor model.

Each term is obtained as follows. The inductance is

$$L_{spiral} = 2\frac{\mu_0 n_{turns}^2 d_{avg} A_{out}}{\pi d_{out}^2}\left[\ln\left(\frac{2.46}{\rho}\right) + 0.2\rho^2\right] \tag{C.2}$$

where

$$\rho = \frac{d_{out} - d_{in}}{d_{out} + d_{in}}, \tag{C.3}$$

$$d_{avg} = \frac{d_{in} + d_{out}}{2}, \tag{C.4}$$

$$A_{out} = \pi\left(\frac{d_{out}}{2}\right)^2 \tag{C.5}$$

where μ_0 is the permeability of free space, n_{turns} is the number of turns of the inductor, d_{in} is the internal radius of the innermost spiral, d_{out} is the external

radius of the outmost spiral. The series resistance is given by

$$R_s = \frac{length}{w\sigma\delta_{skin}(1 - e^{-t/\delta_{skin}})} \tag{C.6}$$

Where

$$\delta_{skin} = \sqrt{\frac{2}{\omega_0\mu_0\sigma}}, \tag{C.7}$$

w is the width of the wire comprising the inductor, σ is the conductivity of the metal, t is the thickness of the metal, and ω_0 is the frequency of operation in rad/s. For a spiral, the length is

$$length = \left(d_{in} + \frac{w}{2}\right) 2\pi n_{turns} + (w + dist)\pi n_{turns}^2 \tag{C.8}$$

The eddy resistance is

$$R_{eddy} = \frac{\sigma_{sub}}{4e^1}(\mu_0 n_{turns} f_0)^2 d_{avg}^3 \rho^{0.7} z_{n.ins}^{-0.55} z_{n.sub}^{0.1} \tag{C.9}$$

Where

$$z_{n.ins} = \frac{t_{ox}}{d_{avg}}, \tag{C.10}$$

$$z_{n.sub} = \frac{1}{d_{avg}}\sqrt{\frac{2}{\omega_0\mu_0\sigma_{sub}}}, \tag{C.11}$$

t_{ox} is the thickness of the oxide, and σ_{sub} is the conductivity of the silicon substrate. The other elements of the model are:

$$C_p = n_{turns} w^2 \varepsilon_0 \frac{\varepsilon_{ox}}{t_{ox}} \tag{C.12}$$

$$C_{ox} = w \cdot length \frac{\varepsilon_0 \varepsilon_{ox}}{t_{ox}} \tag{C.13}$$

$$R_1 = \frac{2}{w \cdot length \cdot G_{sub}} \tag{C.14}$$

$$C_1 = \frac{w \cdot length \cdot C_{sub}}{2} \tag{C.15}$$

Where ε_{ox} is the permittivity of the oxide, G_{sub} is the substrate conductivity, and C_{sub} is the capacitance of the substrate.

The self-resonance of the spiral is:

$$\omega_{res} = \frac{1}{2\pi}\sqrt{L_{spiral}\left[C_p + \left(\frac{C_{ox}}{4}\right) || \left(\frac{C_1}{2}\right)\right]}^{-1/2} \tag{C.16}$$

BIBLIOGRAPHY

[1] G.E. Moore. Cramming more components onto integrated circuits. *Electronics*, 38(8), Apr 1965.

[2] H. Iwai. Cmos technology-year 2010 and beyond. *Solid-State Circuits, IEEE Journal of*, 34(3):357 –366, Mar 1999.

[3] International Technology Roadmap for Semiconductors, 2009.

[4] D. A. B. Miller and H. M. Ozaktas. Limit to the bit-rate capacity of electrical interconnects from the aspect ratio of the system architecture. *Journal of Parallel and Distributed Computing*, 41(1):42–52, Feb 1997.

[5] Nir Magen, Avinoam Kolodny, Uri Weiser, and Nachum Shamir. Interconnect-power dissipation in a microprocessor. In *Proceedings of the 2004 international workshop on System level interconnect prediction*, SLIP '04, pages 7–13, New York, NY, USA, 2004. ACM.

[6] J. C. Palais. *Fiber optic communications*. Prentice Hall, 1988.

[7] M. Lipson. Guiding, modulating, and emitting light on silicon-challenges and opportunities. *Lightwave Technology, Journal of*, 23(12):4222 – 4238, Dec 2005.

[8] R. Soref and B. Bennett. Electrooptical effects in silicon. *IEEE Journal of Quantum Electronics*, 23(1):123–129, Jan 1987.

[9] J. C. Rosenberg, M. J. Green, S. Assefa, T. Barwicz, M. Yang, S. M. Shank, and Y. A. Vlasov. Low-power 30 gbps silicon microring modulator. In *Lasers and Electro-Optics, 2011 and 2011 Conference on Quantum electronics and Laser Science Conference. CLEO/QELS 2011. Conference on*, page PDPB9, May 2011.

[10] Carlos Angulo Barrios, Vilson R. de Almeida, and Michal Lipson. Low-power-consumption short-length and high-modulation-depth silicon electrooptic modulator. *J. Lightwave Technol.*, 21(4):1089, Apr 2003.

[11] Q. Xu and Sameer P. Lipson M. Schmidt, B. Micrometre-scale silicon electro-optic modulator. *Nature*, 435(7040):325–327, May 2005.

[12] M.R. Watts, D.C. Trotter, and R.W. Young. Maximally confined high-speed second-order silicon microdisk switches. In *Optical Fiber Communication Conference*, number c, pages 5–7. Optical Society of America, 2008.

[13] Hugo L. R. Lira, Sasikanth Manipatruni, and Michal Lipson. Broadband hitless silicon electro-optic switch for on-chip optical networks. *Optics Express*, 17(25):22271–22280, Dec 2009.

[14] Joris Van Campenhout, William M. Green, Solomon Assefa, and Yurii A. Vlasov. Ultra-broadband, low-power, 2x2 electro-optic switch using submicron silicon waveguides. In *Optical Fiber Communication Conference*, page OMP2. Optical Society of America, 2010.

[15] G. Cocorullo and I. Rendina. Themooptic modulation at 1.5 um in silicon etalon. *Electronics Letters*, 28(1):83–85, Jan 1992.

[16] S. O. Kasap. *Principles of Electronic Materials and Devices*. McGraw-Hill, 2002.

[17] D. Y. Lin, C. F. Li, Y. S. Huang, Y. C. Jong, Y. F. Chen, L. C. Chen, C. K. Chen, K. H. Chen, and D. M. Bhusari. Temperature dependence of the direct band gap of si-containing carbon nitride crystalline films. *Phys. Rev. B*, 56(11):6498–6501, Sep 1997.

[18] Nicolás Sherwood-Droz, Howard Wang, Long Chen, Benjamin G. Lee, Aleksandr Biberman, Keren Bergman, and Michal Lipson. Optical 4x4 hitless slicon router for optical networks-on-chip (noc). *Opt. Express*, 16(20):15915–15922, Sep 2008.

[19] M. R. Watts, W. A. Zortman, D. C. Trotter, G. N. Nielson, D. L. Luck, and R. W. Young. Adiabatic resonant microrings (arms) with directly integrated thermal microphotonics. In *Lasers and Electro-Optics, 2009 and 2009 Conference on Quantum electronics and Laser Science Conference. CLEO/QELS 2009. Conference on*, pages 1 –2, Jun 2009.

[20] C. R. Pollock. *Fundamentals of optoelectronics*. Richard D. Irwin, Inc., 1995.

[21] Whinnery J. Ramo, S. and T. Van Duzer. *Fields and waves in communication electronics*. John Wiley & Sons, Inc., 1993.

[22] Haruna M. Nishihara, H. and T. Suhara. *Optical integrated circuits*. McGraw-Hill, 1989.

[23] Y. P. Li and C. H. Henry. Silica-based optical integrated circuits. *Optoelectronics, IEE Proceedings* -, 143(5):263 –280, Oct 1996.

[24] Christie K. Madsen and J. H. Zhao. *Optical Filter Design and Analysis: A Signal Processing Approach*. John Wiley & Sons, Inc., New York, NY, USA, 1st edition, 1999.

[25] L. B. Soldano and E. C. M. Pennings. Optical multi-mode interference devices based on self-imaging: principles and applications. *Lightwave Technology, Journal of*, 13(4):615 –627, Apr 1995.

[26] R. Ulrich and G. Ankele. Self-imaging in homogeneous planar optical waveguides. *Applied Physics Letters*, 27(6):337 –339, Sep 1975.

[27] Assaf Shacham, Keren Bergman, and L.P. Carloni. On the design of a photonic network-on-chip. In *Proceedings of the First International Symposium on Networks-on-Chip*, pages 53–64. IEEE Computer Society, 2007.

[28] Ajay Joshi, Christopher Batten, V. Stojanović, and K. Asanović. Building manycore processor-to-DRAM networks using monolithic silicon photonics. In *High Performance Embedded Computing (HPEC) Workshop*, 2008.

[29] Andrew W. Poon, Xianshu Luo, Fang Xu, and Hui Chen. Cascaded Microresonator-Based Matrix Switch for Silicon On-Chip Optical Interconnection. *Proceedings of the IEEE*, 97(7):1216–1238, 2009.

[30] Benjamin G. Lee, Benjamin A. Small, Keren Bergman, Qianfan Xu, and Michal Lipson. Transmission of high-data-rate optical signals through a micrometer-scale silicon ring resonator. *Optics letters*, 31(18):2701–3, Sep 2006.

[31] Francisco J. Mesa-Martinez, Michael Brown, Joseph Nayfach-Battilana, and Jose Renau. Measuring performance, power, and temperature from real processors. *Workshop On Experimental Computer Science*, 2007.

[32] Y. Goebuchi. Fast and stable wavelength-selective switch using double-series coupled dielectric microring resonator. *IEEE Photonics Technology Letters*, 43(8B):5766–540, Feb 2006.

[33] Yuta Goebuchi, Masahiko Hisada, Tomoyuki Kato, and Yasuo Kokubun. Optical cross-connect circuit using hitless wavelength selective switch. *Optics express*, 16(2):535–48, Jan 2008.

[34] M.A. Popović, T. Barwicz, F. Gan, M.S. Dahlem, C.W. Holzwarth, P.T. Rakich, H.I. Smith, E.P. Ippen, and F.X. K\\"artner. Transparent wavelength switching of resonant filters. In *Conference on Lasers and Electro-Optics (CLEO), Baltimore, MD*, 2007.

[35] Yurii Vlasov, William M. J. Green, and Fengnian Xia. High-throughput silicon nanophotonic wavelength-insensitive switch for on-chip optical networks. *Nature Photonics*, 2(4):242–246, Mar 2008.

[36] H.A. Haus, M.A. Popovic, and M.R. Watts. Broadband hitless bypass switch for integrated photonic circuits, May 2006.

[37] S.Y. Cho and Richard Soref. Interferometric microring-resonant 2 x 2 optical switches. *Optics Express*, 16(17):13304–13314, 2008.

[38] C. Li, X. Luo, and A. W. Poon. Dual-microring-resonator electro-optic logic switches on a silicon chip. *Semiconductor Science and Technology*, 23(6):064010, 2008.

[39] Sasikanth Manipatruni, Qianfan Xu, Bradley Schmidt, Jagat Shakya, and Michal Lipson. High Speed Carrier Injection 18 Gb/s Silicon Micro-ring Electro-optic Modulator. *LEOS 2007 - IEEE Lasers and Electro-Optics Society Annual Meeting Conference Proceedings*, pages 537–538, Oct 2007.

[40] M.W. Geis, S.J. Spector, R.C. Williamson, and T.M. Lyszczarz. Submicrosecond Submilliwatt Silicon-on-Insulator Thermooptic Switch. *IEEE Photonics Technology Letters*, 16(11):2514–2516, Nov 2004.

[41] R. Orta, P. Savi, R. Tascone, and D. Trinchero. Synthesis of multiple-ring-resonator filters for optical systems. *Photonics Technology Letters, IEEE*, 7(12):1447–1449, 1995.

[42] B. E. Little, S. T. Chu, H. A. Haus, J. Foresi, and J. Laine. Microring Resonator Channel Dropping Filters. *Lightwave*, 15(6):998–1005, 1997.

[43] Andrea Melloni, Associate Member, and Mario Martinelli. Synthesis of Direct-Coupled-Resonators Bandpass Filters for WDM Systems. *Lightwave*, 20(2):296–303, 2002.

[44] A. Yariv. Universal relations for coupling of optical power between microresonators and dielectric waveguides. *Electronics Letters*, 36(4):321–322, 2000.

[45] Joyce Poon, Jacob Scheuer, Shayan Mookherjea, George Paloczi, Yanyi Huang, and Amnon Yariv. Matrix analysis of microring coupled-resonator optical waveguides. *Optics express*, 12(1):90–103, Jan 2004.

[46] Fengnian Xia, Lidija Sekaric, and Yurii a Vlasov. Mode conversion losses in silicon-on-insulator photonic wire based racetrack resonators. *Optics express*, 14(9):3872–86, May 2006.

[47] C. Manolatou and M. Lipson. All-optical silicon modulators based on carrier injection by two-photon absorption. *Journal of Lightwave Technology*, 24(3):1433–1439, Mar 2006.

[48] Y Varshni. Temperature dependence of the energy gap in semiconductors. *Physica*, 34(1):149–154, 1967.

[49] P. Dumon, G. Priem, L.R. Nunes, W. Bogaerts, D. Van Thourhout, P. Bienstman, T.K. Liang, M. Tsuchiya, P. Jaenen, S. Beckx, and Others. Linear and nonlinear nanophotonic devices based on silicon-on-insulator wire waveguides. *Japanese Journal of Applied Physics*, 45(8B):6589–6602, 2006.

[50] H. C. Huang, S. Yee, and M. Soma. Quantum calculations of the change of refractive index due to free carriers in silicon with nonparabolic band structure. *Journal of Applied Physics*, 67(4):2033, 1990.

[51] Jacob T Robinson, Kyle Preston, Oskar Painter, and Michal Lipson. First-principle derivation of gain in high-index-contrast waveguides. *Optics express*, 16(21):16659–69, Oct 2008.

[52] Joris Van Campenhout, William M. J. Green, Xiaoping Liu, Solomon Assefa, Richard M. Osgood, and Yurii A. Vlasov. Silicon-nitride surface passivation of submicrometer silicon waveguides for low-power optical switches. *Optics letters*, 34(10):1534–6, May 2009.

[53] Jacques Henri Collet, Daniel Litaize, Jan Van Campenhout, Chris Jesshope, Marc Desmulliez, Hugo Thienpont, James Goodman, and Ahmed Louri. Architectural approach to the role of optics in monoprocessor and multiprocessor machines. *Appl. Opt.*, 39(5):671–682, Feb 2000.

[54] Lawrence Domash, Ming Wu, Nikolay Nemchuk, and Eugene Ma. Tunable and switchable multiple-cavity thin film filters. *J. Lightwave Technol.*, 22(1):126, Jan 2004.

[55] Yiying Zuo, Madeleine Mony, Babak Bahamin, Etienne Grondin, Vincent Aimez, and David V. Plant. Bulk electro-optic deflector-based switches. *Appl. Opt.*, 46(16):3323–3331, Jun 2007.

[56] Marcel W. Pruessner, Todd H. Stievater, Mike S. Ferraro, and William S. Rabinovich. Thermo-optic tuning and switching in soi waveguide fabry-perot microcavities. *Opt. Express*, 15(12):7557–7563, Jun 2007.

[57] Bradley J Frey, Douglas B Leviton, and Timothy J Madison. Temperature dependent refractive index of silicon and germanium. *Proceedings of SPIE*, 6273(3):10, 2006.

[58] C. Z. Tan and J. Arndt. Temperature dependence of refractive index of glassy sio2 in the infrared wavelength range. *Journal of Physics and Chemistry of Solids*, 61(8):1315 – 1320, 2000.

[59] L. J. Chen. *Silicide technology for integrated circuits*. The Institution of Electrical Engineers, 2004.

[60] Deal M. D. Plummer, J. D. and P. B. Griffin. *Silicon VLSI technology*. The Institution of Electrical Engineers, 2000.

[61] Y. S. Kim, J.-S. Kim, J. S. Choi, I. R. Hwang, S. H. Hong, S.-O. Kang, and B. H. Park. Resistive switching behaviors of nio films with controlled number of conducting filaments. 98(19):192104, 2011.

[62] Assaf Shacham, Keren Bergman, and Luca P. Carloni. Photonic networks-on-chip for future generations of chip multiprocessors. *IEEE Transactions on Computers*, 57(9):1246–1260, Sep 2008.

[63] Christopher Batten, Ajay Joshi, Jason Orcutt, Anatoly Khilo, Benjamin Moss, Charles Holzwarth, Milos Popovic, Hanqing Li, Henry Smith, Judy Hoyt, Franz Kartner, Rajeev Ram, Vladimir Stojanovic, and Krste Asanovic. Building manycore processor-to-dram networks with monolithic silicon photonics. *High-Performance Interconnects, Symposium on*, 0:21–30, 2008.

[64] Qianfan Xu, David Fattal, and Raymond G. Beausoleil. Silicon microring resonators with 1.5-mu m radius. *Optics Express*, 16(6):4309–4315, Mar 2008.

[65] Shijun Xiao, Maroof H. Khan, Hao Shen, and Minghao Qi. A highly compact third-order silicon microring add-drop filter with a very large free

spectral range, a flat passband and a low delay dispersion. *Optics Express*, 15(22):14765–14771, Oct 2007.

[66] Magdalena S. Nawrocka, Tao Liu, Xuan Wang, and Roberto R. Panepucci. Tunable silicon microring resonator with wide free spectral range. *Applied Physics Letters*, 89(7):071110–071113, Aug 2006.

[67] K. Oda, N. Takato, and H. Toba. A wide-FSR wave-guide double-ring resonator for optical FDM transmission-systems. *Journal of Lightwave Technology*, 9(6):728–736, Jun 1991.

[68] G. Barbarossa and A.M. Matteo. Novel double-ring optical-guided-wave Vernier resonator. *IEE Proceedings-Optoelectronics*, 144(4):203–208, Aug 1997.

[69] M. R. Watts, T. Barwicz, M. Popovic, L. Socci, P. T. Rakich, E. P. Ippen, H. I. Smith, and F. Kaertner. Design, fabrication, and characterization of a free spectral range doubled ring-resonator filter. In *Lasers and Electro-Optics, 2005. (CLEO). Conference on*, volume 1, pages 269 –272, May 2005.

[70] W. M. J. Green, R. K. Lee, G. A. DeRose, A. Scherer, and A. Yariv. Hybrid InGaAsP-InP Mach-Zehnder racetrack resonator for thermooptic switching and coupling control. *Optics Express*, 13(5):1651–1659, Mar 2005.

[71] Linjie Zhou and Andrew W. Poon. Electrically reconfigurable silicon microring resonator-based filter with waveguide-coupled feedback. *Optics Express*, 15(15):9194–9204, Jul 2007.

[72] Long Chen, Nicolas Sherwood-Droz, and Michal Lipson. Compact bandwidth-tunable microring resonators. *Optics Letters*, 32(22):3361–3363, Nov 2007.

[73] R. Orta, P. Savi, R. Tascone, and D. Trinchero. Synthesis of multiple-ring-resonator filters for optical systems. *IEEE Photonics Technology Letters*, 7(12):1447–1449, Dec 1995.

[74] Richard L. Espinola, Tomoyuki Izuhara, Ming-Chun Tsai, Jr. Richard M. Osgood, and Horst Dötsch. Magneto-optical nonreciprocal phase shift in garnet/silicon-on-insulator waveguides. *Opt. Lett.*, 29(9):941–943, May 2004.

[75] T. R. Zaman, X. Guo, and R. J. Ram. Faraday rotation in an inp waveguide. 90(2):023514, 2007.

[76] Ming-Chun Tien, Tetsuya Mizumoto, Paolo Pintus, Herbert Kromer, and John E. Bowers. Silicon ring isolators with bonded nonreciprocal magneto-optic garnets. *Opt. Express*, 19(12):11740–11745, Jun 2011.

[77] Marin Soljačić, Chiyan Luo, J. D. Joannopoulos, and Shanhui Fan. Nonlinear photonic crystal microdevices for optical integration. *Opt. Lett.*, 28(8):637–639, Apr 2003.

[78] Sasikanth Manipatruni, Jacob T. Robinson, and Michal Lipson. Optical nonreciprocity in optomechanical structures. *Phys. Rev. Lett.*, 102(21):213903, May 2009.

[79] Liang Feng, Maurice Ayache, Jingqing Huang, Ye-Long Xu, Ming-Hui Lu, Yan-Feng Chen, Yeshaiahu Fainman, and Axel Scherer. Nonreciprocal light propagation in a silicon photonic circuit. *Science*, 333(6043):729–733, 2011.

[80] H. A. Haus. *Waves and Fields in Optoelectronics*. Prentice-Hall, 1984.

[81] Zongfu Yu and Shanhui Fan. Complete optical isolation created by indirect interband photonic transitions. *Nature Photonics*, 3(2):91–94, Feb 2009.

[82] R. W. Boyd. *Nonlinear Optics*. Academic Press, 2008.

[83] T. H. Lee. *The Design of CMOS Radio-Frequency Integrated Circuits*. Cambridge Univ. Press, 2004.

[84] Anatol Khilo, Cheryl M. Sorace, and Franz X. Kärtner. Broadband linearized silicon modulator. *Opt. Express*, 19(5):4485–4500, Feb 2011.

[85] Farg R. Chadha R. Gupta, K. C. *Computer-aided design of microwave circuits*. Artech House, 1981.

[86] B. C. Wadell. *Transmission line design handbook*. Artech House, 1991.